



UNIVERSITY OF ROME TOR VERGATA

MASTER THESIS IN PHYSICS

---

**Inelastic neutron scattering at eV energies with  
enhanced counting statistics and noise reduction**

---

*Author:*

Pierfrancesco ULPANI

*Supervisors:*

Roberto Senesi  
Carla Andreani  
Giovanni Romanelli

---

Academic year 2016-2017

*'Illud in his quoque te rebus cognoscere avemus,  
corpora cum deorsum rectum per inane feruntur  
ponderibus propriis, incerto tempore ferme  
incertisque locis spatio depellere paulum,  
tantum quod momen mutatum dicere possis.  
Quod nisi declinare solerent, omnia deorsum,  
imbris uti guttae, caderent per inane profundum,  
nec foret offensus natus nec plaga creata  
principiis: ita nihil umquam natura creasset '*

Titus Lucretius Carus, De rerum natura, II, 216-224

University of Rome Tor Vergata

# *Abstract*

Department of Physics

Master

## **Inelastic neutron scattering at eV energies with enhanced counting statistics and noise reduction**

by Pierfrancesco ULPANI

Neutrons are the neutral particle used for the investigation of materials at the atomic scale. The delicate, precise and highly penetrating nature of low energy (meV to eV) neutron beams, make them ideal to study in a non destructive way the structure and dynamics of matter with atomic resolution. In particular, inelastic neutron scattering at eV energies is an experimental technique for the measurement of atomic momentum distributions, and as such is capable of obtaining information on the atomic quantum dynamics in condensed matter. For this reason in recent years significant efforts have been devoted to improve eV neutron spectrometers, both from the design and from the signal detection points of view. This work provides a description of experiments aimed at the detection improvement obtained on the photon sensitive Yttrium-Aluminum-Perovskite (YAP) detectors, installed on the VESUVIO spectrometer at the ISIS spallation neutron source. YAP detectors on VESUVIO are used as time resolved gamma counters to record the radiative emission of resonant neutron absorption of a neutron-gamma converter gold foil. The latter shows an intense resonance at 4.9 eV, and the converter-detector system has the functions of neutron energy analyser and time of flight resolved neutron counting detector. In a measurement on the VESUVIO spectrometer there are two types of photons detected: background photons, coming from the blockhouse and other parts of the spectrometer and signal photons, coming from the resonant gold foil in front of the detector. At present YAP detectors are set to operate with a Low Level Discrimination (LLD) threshold measuring only photons with energy greater than 600 keV. On the other hand, recent studies have shown that the most intense prompt gamma emission from radiative neutron capture at 4.9 eV from gold is concentrated at energies lower than the actual threshold. This motivates the work presented in this thesis, that is to lower and optimise the value of the threshold and provide an experimental assessment of the spectrometer performance following the optimisation showing an improvement on the counting error bars and counting fluctuations in the scattering spectra. The results provide evidence for quantitative improvements on the measurements of atomic momentum distributions, and on the instrument mass-sensitivity, paving the way towards new classes of experiments.

## *Acknowledgements*

Molto spesso mi capita di poter confessare alle persone che questa laurea magistrale è stata sotto molti punti di vista un gioco ma, al contrario, molto raramente sono capitate delle occasioni per poter ringraziare tutti quelli che hanno partecipato al divertimento. Questa sezione quindi ricopre un ruolo molto importante, scritta in italiano per nascondere, almeno per ora, la mia fredda e schizofrenica sensazione legata alla lingua inglese. Dovendo pur cominciare da qualche parte perché non dall'ideatore della tesi Prof. Roberto Senesi che mi ha accolto in modo quasi fraterno all'interno del gruppo e che senz'altro cerca di fare ogni giorno più di quello che un Professore sarebbe tenuto a fare; inoltre ringrazio la Prof.ssa Carla Andreani per avermi coinvolto da subito in tutte le esperienze formative a cui avrei potuto partecipare e Giovanni per la sua spiazzante simpatia ed intelligenza che ha reso ogni analisi dati un gioco da ragazzi. Ovviamente ringrazio anche quella parte del gruppo la quale è riuscita, anche forse per poco, a farmi capire che la scienza non è tutto e che deve essere il tutto a contribuire nelle scelte poiché ogni sfaccettatura, che ci rende quello che siamo, ha il diritto ad un piatto nella bilancia. Forse l'unico grande rammarico della chiusura di questo grande capitolo è il lasciarsi alle spalle un gruppo di amici, e non solo colleghi, che si sono trovati a sgomitare insieme fra una risata ed un'altra nelle situazioni disagiate in quel di Sogene, ringrazio con il cuore in mano ognuno di loro, anche quelli che non ci sono più per scelte diverse o per qualche maledetto e disgraziato motivo; oltre per le mitiche e piacevolissime conversazioni con persone dal cuore nucleare, dall'animo strutturista e testa da teorico, in grado di risolvere qualsiasi problema, vorrei ringraziarli perché grazie a loro ho imparato, paradossalmente in un ambiente fortemente competitivo, che non serve mettere i gomiti sulle spalle di chi ti sta affianco per alzarli e farti notare. Pur essendo convinto che i ringraziamenti siano strettamente connessi al momento in cui ci si trova a scrivere la tesi penso che ci siano, ad ogni modo, delle radici che non si possono non menzionare poiché, nonostante tutto, costituiscono sempre la tua famiglia che rende ogni esperienza un Capitolo e non un semplice paragrafo. In particolare ringrazio mio Padre perché attraverso la sua squisita follia mi ha trasmesso la passione e l'entusiasmo nella conoscenza. Infine ringrazio Francesca che ha vissuto con me passo passo tutte le esperienze degli ultimi anni, dandomi la forza per combattere e il coraggio per andare avanti diventando la più bella scoperta che abbia mai fatto in questi anni da Fisico.

Concludo sperando che anche i non nominati a cui è rivolto il paragrafo trovino fra queste poche righe qualcosa in cui identificarsi riuscendo così a ringraziarli per avermi fatto distogliere lo sguardo da quei rumorosi silenzi che ultimamente offuscavano la mia vista.

*A mia madre,  
augurandole che il mio sguardo possa restituirle la forza,  
il coraggio e la determinazione che un giorno vedevo brillare nel suo*

# Contents

<b>1</b>	<b>Introduction</b>	<b>1</b>
<b>2</b>	<b>Neutron interaction</b>	<b>5</b>
2.1	Basic properties of neutrons . . . . .	5
2.2	Neutron scattering . . . . .	7
2.3	Deep Inelastic Neutron Scattering . . . . .	11
2.4	Other neutron reactions . . . . .	13
<b>3</b>	<b>Sources and instrumentation</b>	<b>17</b>
3.1	Neutron Sources and Facilities . . . . .	17
3.1.1	Reactors . . . . .	18
3.1.2	Proton Accelerator-Based Sources . . . . .	18
3.1.3	Moderation Mechanisms for Spallation Sources . . . . .	20
3.2	Basic principles of the time-of-flight technique . . . . .	21
3.3	ISIS spallation neutron source . . . . .	23
3.3.1	Ion source . . . . .	23
3.3.2	Linac . . . . .	23
3.3.3	Synchrotron . . . . .	23
3.3.4	Target station 1 and muon target . . . . .	24
3.3.5	Target station 2 . . . . .	24
<b>4</b>	<b>The VESUVIO spectrometer</b>	<b>26</b>
4.1	Detectors . . . . .	28
4.1.1	Scintillators . . . . .	28
4.1.2	Inorganic scintillators . . . . .	29
4.1.3	YAP(Ce) . . . . .	31
4.1.4	<sup>6</sup> Li-glass . . . . .	32
4.1.5	Pulse processing . . . . .	33
4.2	Resonance-Filter . . . . .	35
4.3	Resonance-Detector . . . . .	38
<b>5</b>	<b>Measurements and data Analysis</b>	<b>45</b>
5.1	Materials and methods . . . . .	46
5.2	First measurement without CCR . . . . .	49
5.2.1	Time of flight spectra . . . . .	49
5.2.2	y-space spectra . . . . .	51

5.2.3	Signal background ratio . . . . .	53
5.3	Second measurements with CCR . . . . .	55
5.3.1	Time of flight spectra . . . . .	55
5.3.2	y-space spectra . . . . .	58
5.3.3	Signal background ratio . . . . .	59
5.4	Detector dependence . . . . .	59
5.5	Noise reduction . . . . .	62
5.6	Fit of the Compton profile . . . . .	65
<b>6</b>	<b>Conclusions</b>	<b>69</b>
<b>A</b>	<b>Bi-parametric measurements</b>	<b>71</b>
<b>B</b>	<b>Other time of flight spectra</b>	<b>73</b>
<b>C</b>	<b>Script used to fit <math>J(y, \mathbf{q})</math> spectra</b>	<b>81</b>
	<b>Bibliography</b>	<b>84</b>

## Chapter 1

# Introduction

The delicate, precise, and highly penetrating nature of low-energy (meV to eV) neutrons makes them ideal to study in a non destructive manner the structure and dynamics of matter with an atomic scale resolution. In particular, inelastic neutron scattering at eV energies is an experimental technique for the measurement of atomic momentum distributions, and as such is capable to obtain information on the atomic quantum dynamics in condensed matter (ref. [1] and [2]). The atomic momentum distribution is strictly connected, through Fourier transform, with the atomic wave function, in those systems represented by a particle confined in a binding potential <sup>1</sup>

$$n(\mathbf{p}) = |\Psi(\mathbf{p})|^2 \rightarrow |\Psi(\mathbf{r})|^2$$

Experiments allow to directly measure the longitudinal momentum distribution,  $J(y, \mathbf{q})$ , which is simply related to the momentum distribution  $n(\mathbf{p})$  in the Impulse Approximation via:

$$J_{IA}(y, \hat{\mathbf{q}}) = \hbar \int d\mathbf{p} n(\mathbf{p}) \delta(\hbar y - \mathbf{p} \cdot \hat{\mathbf{q}})$$

This quantity has a deep physical meaning, in fact information connected with the local structure of systems under study, as the interatomic potential, can be derived from that using, for example, an inversion of the Schroedinger equation (ref. [4]). A detailed knowledge of the interatomic potential can be of crucial importance for the derivation of the phase diagram of a condensed matter system. This information are extracted by the experimental data trough the study of the lineshape of the spectra acquired. As a consequence there is a great interest in understanding all the possible way to decrease noise and error bars that affect the lineshape.

As an example it can be considered the interatomic potential in systems where hydrogen is present (water, ice...). In fig. 1.1 is shown the most recent theoretical model for the proton  $|\Psi(\mathbf{r})|^2$  and interatomic potential (ref. [5]).

In this figure there is information about the zero-point energy, asymmetry of  $|\Psi(\mathbf{r})|^2$ , and an anharmonicity shape of the potential due to the interaction of hydrogen with the oxygen atom. At

---

<sup>1</sup>In general the Fourier Transform of the momentum distribution is the one body density matrix (ref. [3]). In many experimental cases the non interacting approximation can be used. Examples are systems composed by light atoms bound to heavy atoms.

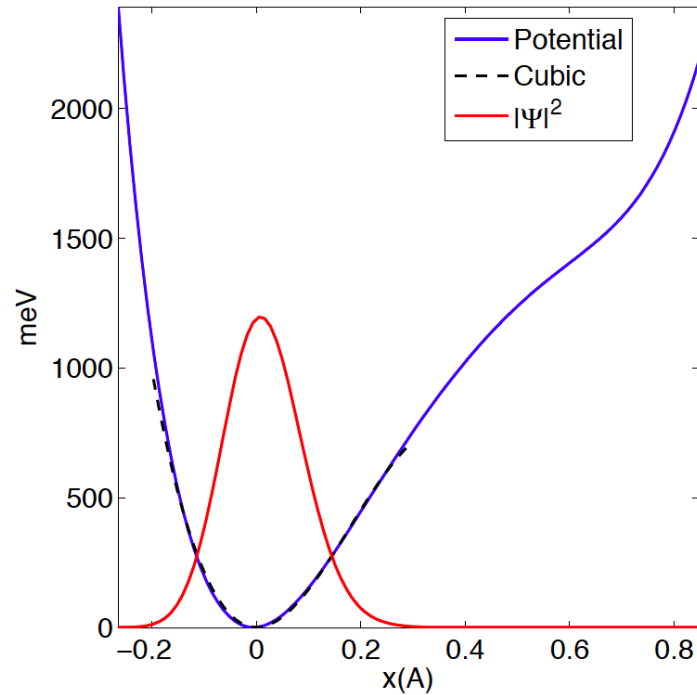


FIGURE 1.1: Theoretical potential energy surface of the proton in ice along the bond direction (blue solid line), cubic fitting potential (black dashed line) and the corresponding ground state wave function  $|\Psi(r)|^2$  (red solid line), ref. [5].

VESUVIO, a spectrometer installed in the ISIS pulsed neutron source, Rutherford Appleton Laboratory (RAL), was performed the best experimental measurement of the  $|\Psi(\mathbf{p})|^2$  represented in red (Fourier transform) in fig. 1.1. The experimental result obtained is shown in fig. 1.2.

The characterization of the microscopic state and comparison with theoretical model goes hand in hand with the quality of the experimental data in terms of statistical errors and noise. In fact the spectrum reported in fig. 1.2 is affected by an uncertainty of 1% at the centre of the overall spectrum and of 15% at 1/15 of the peak height in correspondence of the tails. In order to understand and verify the anisotropy of the theoretical model, the tails, where the uncertainty is greater, are of fundamental importance, in fact from that measurement no asymmetry in the wave function or interatomic potential was experimentally noted because of the error bars.

As another example of the necessity to go beyond the actual experimental limit can be considered the same type of experiment on heavy water where the oxygen momentum distribution can be analysed. This experiment provided the first experimental determination of nuclear quantum effects of oxygen in water analysing the lineshape in the acquired spectra which give a value of the average kinetic energy greater than the classic one predicted by the equipartition theorem. In fig. 1.3 is shown the momentum distribution of oxygen obtained in the experiment. Also in this case is desirable a decreasing effect on the error bars and noise to derive in a more precise way the nuclear quantum effects.

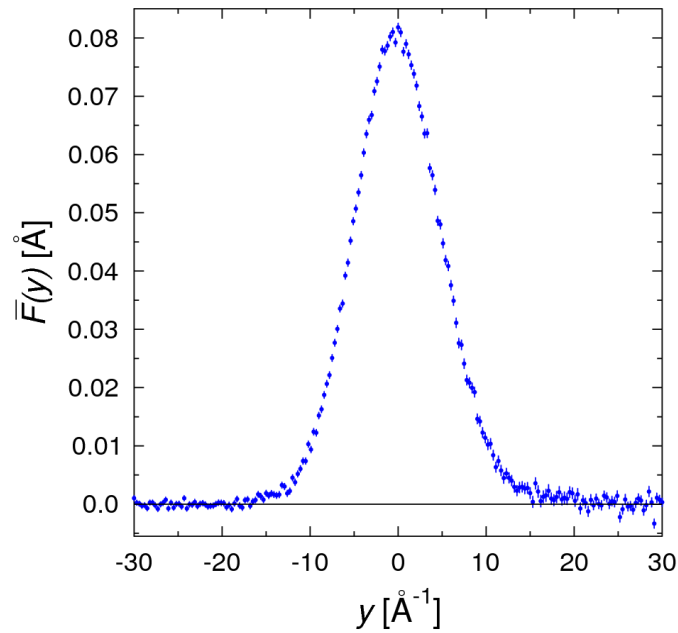


FIGURE 1.2: Experimental result of the Neutron Compton Profile  $F(y, \mathbf{q})$  of bulk ice, strictly connected (ref. [6]) to the atom momentum distribution  $|\Psi(\mathbf{p})|^2$ , ref [7].

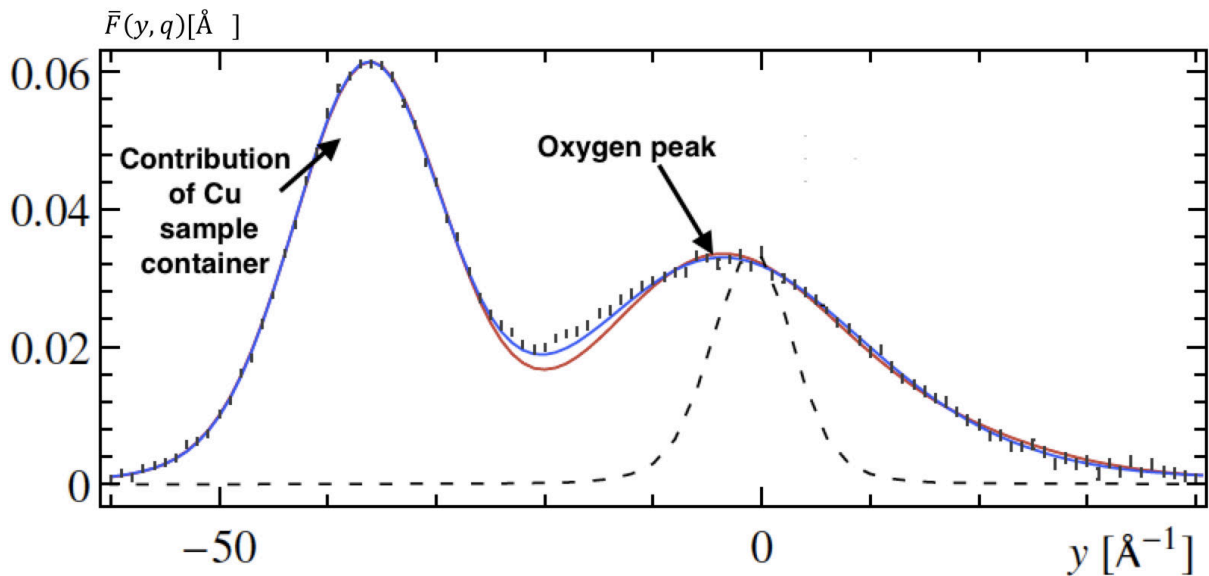


FIGURE 1.3: Experimental data of Neutron Compton Profile for oxygen with best fits (simple Gaussian in red and multivariate averaged Gaussian in blue). The peak around  $y = -40 \text{ \AA}$  comes from the Cu sample container. The black dotted line is the instrumental resolution, ref. [8].

Finally, another important research objective is the quantitative non-destructive hydrogen measurement in bulk samples which is a challenging task. This type of experiment can be performed on VESUVIO because the signal is mass-resolved and neutrons are a non-destructive

bulk probe. In fact the quantity of a certain element (in this case hydrogen) can be measured using the area under the signal peak associated with the element. The best sensibility at present is of the order of  $10\mu\text{mol}/\text{cm}^2$  but there are applications such as H-doped technological materials or complex hydrates where this is not enough as in the luminescence of amorphous porous silicon due to hydrogen (ref. [9]), hydrogen content in fusion materials (ref. [10]) or the study of the structures and operation of the catalyst at the molecular level for catalysis reactions (ref. [11]).

For all these reasons, the principal objective of my thesis is to find experimental methods finalized to improve the quality of the spectra in the atom momentum distribution acquired increasing the counting statistics of signal and reducing the noise.

The demonstration of the improvement was achieved with the results obtained from an experiment performed at the ISIS pulsed neutron source using the VESUVIO spectrometer. In this experiment I was responsible for the changes of the acquisition set-up and data analysis. Results show an improvement on the statistical poissonian error bars and counting fluctuation in the Time Of Flight (TOF) spectra, of a standard 0.25 mm thick polyethylene sample, after the Low Level Discrimination threshold decrease in the forward YAP(Ce) scintillators. The expense is a little increase of the S/B ratio (ref. [12] and [13]) that become, anyway, irrelevant after the background subtraction. It leads to a more precise and sensible measurements of the atom momentum distribution (which is one of the most important information obtained using the VESUVIO spectrometer) paving the way to a new kind of experiments.

In this thesis, I have preliminary introduced in chapter 2 the neutron interaction processes with particular attention to the Deep Inelastic Neutron Scattering which is the process studied in the experiment. Then, I have described in chapter 3 the different types of neutron sources with emphasis to the ISIS spallation neutron source used for our experiment. In chapter 4 there is a description of the VESUVIO spectrometer from any point of view. Then in chapter 5 there is the description of the experiment performed, the data analysis and discussions. Finally, conclusions are drawn in chapter 6 and many appendices are called in the text to facilitate the reading.

## Chapter 2

# Neutron interaction

### 2.1 Basic properties of neutrons

With the advent of nuclear reactors, neutrons have become an important tool for investigating many important features of matter. The basic physical properties of neutrons are:

- mass  $m = 1.67510^{-27} kg$
- Charge  $q = 0$
- spin  $1/2$
- magnetic dipole moment  $\mu_n = -1.913\mu_N$

The energy  $E$  of a neutron with a wave vector  $\mathbf{k}$  is

$$E = \frac{\hbar^2 k^2}{2m} \quad (2.1)$$

In neutron spectroscopy energies are often given in units of  $meV$ ; using  $m = 938MeV$  we have

$$\frac{\hbar^2}{2m} = 2.08meV \text{ \AA}^2$$

From this expression we can see that a neutron with a wave vector  $k \sim \text{\AA}^{-1}$  has an energy  $E \sim meV$ . This energy is typical of the energy carried by lattice vibrations. Using the de Broglie relation

$$\lambda = \frac{h}{mv} \quad (2.2)$$

we can see that neutrons with energy  $E \sim meV$  have a wavelength  $\lambda$  comparable with atomic spacing in condensed matter. As a consequence the diffraction of neutrons from condensed matter can display interference effects.

Slow neutron beams (under 20 MeV) are often described as being cold, thermal, hot or epithermal. There is no standard definition of these terms but one interpretation is shown in table 2.1

In neutron scattering experiments the key variables are the change in the neutron energy and the concomitant change in the wave vector. Calling the initial and final energy and wave vector

	E (meV)
Cold	0.1-10 meV
Thermal	10-100 meV
Hot	100-500 meV
Epithermal	>500 meV

TABLE 2.1: Nomenclature for neutron energies

$E_i, k_i$  and  $E_f, k_f$  we can define the energy transferred as

$$\hbar\omega = E_i - E_f = E = \frac{\hbar^2(k_i^2 - k_f^2)}{2m} \quad (2.3)$$

and the scattering wave vector

$$\mathbf{q} = \mathbf{k}_i - \mathbf{k}_f \quad (2.4)$$

The motion of atoms and their spatial correlations are revealed in a neutron scattering experiment when  $\hbar\omega$  and  $q = |\mathbf{q}|$  match the corresponding energies and wave vectors involved. It is evident from eq. 2.3 that  $\omega$  and  $q$  are related; this relation imposes kinematic constraints on the scattering experiments. For example, in order to gain access to the domain of large  $\omega$  and small  $q$  it is necessary to use incident neutrons with high energy and small scattering angles; not all of  $(q, \omega)$  space is accessible in a neutron scattering experiment and it means that the neutron source and spectrometer configuration limit the range of experiments that can be performed. The penetration depth of neutrons in matter is extremely large, mainly because they don't have charge so there is no Coulomb interaction to overcome. Neutrons are thus scattered by nuclear forces and the scattering process is well suited to the study of bulk properties. The scattering provides information on the physical and chemical properties of the target sample which remain mostly unaffected after the interaction with the experimental probe. In fact, neutron studies are non destructive.

As opposed to X-ray interaction, where the intensity is a monotonic function of  $Z$ , neutron cross section doesn't show any simple dependence upon  $Z$  (atomic number) or  $A$  (mass number) values. This feature of the scattering can be very valuable, enabling studies using isotopes substitutions. An example could be the contrast between hydrogen and deuterium where the scattering from hydrogen exceeds the deuterium one by an order of magnitude.

We can conclude that the most important properties of neutron characterization are:

- sensitivity to different isotopes
- deep penetration into the target
- not-destructive probe
- energy of thermal neutrons are of the same order of many elemental excitations
- de Broglie wavelength of thermal neutrons is of the order of interatomic distances

- magnetic interaction between neutrons and unpaired electrons in magnetic atoms

## 2.2 Neutron scattering

The geometry of a scattering experiment is shown in figure 2.1

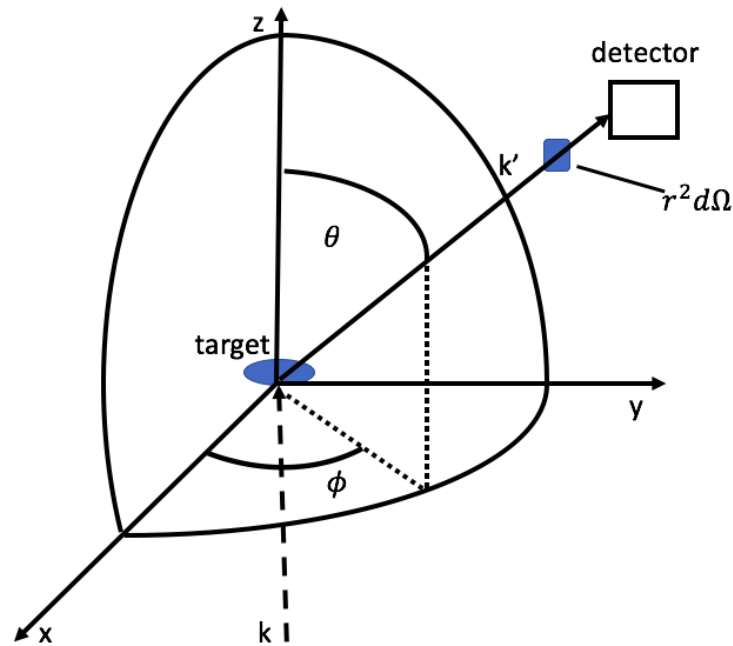


FIGURE 2.1: Scheme of scattering experiment

A neutron in the scattering experiment with wave vector  $\mathbf{k}_i$  is scattered into a state with wave vector  $\mathbf{k}_f$  and  $\mathbf{q}$  is the momentum transferred. If  $|\mathbf{k}_i| \neq |\mathbf{k}_f|$  the scattering process is called inelastic, otherwise is called elastic. In fig. 2.2 is reported a scheme with the different regime, depending on the magnitude of the energy transfers.

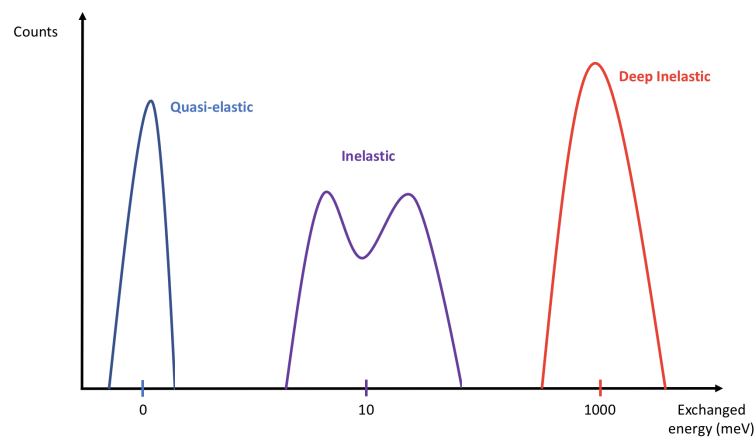


FIGURE 2.2: Different types of neutron scattering

The basic quantity which is measured in these experiments is the double partial differential cross section which gives the fraction of neutrons of incident energy  $E_i$  scattered into an element

of solid angle  $d\Omega$  with an energy between  $E_f$  and  $E_f + dE_f$ . It is denoted by

$$\frac{d^2\sigma}{d\Omega dE_f} \quad (2.5)$$

It has the dimension of area/energy per solid angle. The only satisfactory way to derive an expression for the cross-section is to use the formal scattering theory. We can describe the scattering process for a general neutron scattering with no resonances or absorption and then focus on a specific scattering case, the Deep Inelastic Neutron Scattering (DINS).

In general we can assume that the initial state of neutron  $|k_i\rangle$  is described by a plane wave

$$|k_i\rangle \sim \frac{1}{\sqrt{V}} e^{i\mathbf{k}_i \cdot \mathbf{r}} \quad (2.6)$$

Even the final state can be described by a plane wave under the assumption that we are far away from the sample (scattering point); it is called Born approximation

$$|k_f\rangle \sim \frac{1}{\sqrt{V}} e^{i\mathbf{k}_f \cdot \mathbf{r}'} \quad (2.7)$$

In scattering experiments, detectors measure the number of neutrons scattered per unit time; it depends on the differential cross section. In order to describe the counts of detectors we can write

$$\frac{d^3N}{\hbar d\omega d\Omega dt} = \frac{d^2\sigma}{\hbar d\omega d\Omega} \frac{d^2N}{d\sigma dt} \quad (2.8)$$

Were N is the number of neutrons. The term on the left side of the equation is the number of scattered neutrons in an solid angle  $d\Omega$  around a general direction with an energy exchange in the process  $\hbar\omega = E_i - E_f$  in a  $d\omega$  interval for unit time ( $\hbar\omega$  comes from any combination of suitable  $\mathbf{k}_i$  and  $\mathbf{k}_f$ ). The first term on the right side of the equation is the double differential cross-section to diffuse neutrons in a solid angle  $d\Omega$  with energy exchange  $\hbar\omega$  in  $\hbar d\omega$  interval; the second term is the number of incident neutrons for unit area and time that is equal to  $\frac{N}{V} v_i$  (V= volume and  $v_i = \frac{P_i}{m}$  velocity of incident neutron) obtaining

$$\frac{d^3N}{\hbar d\omega d\Omega dt} = \frac{N P_i}{V m} \frac{d^2\sigma}{\hbar d\omega d\Omega} \quad (2.9)$$

The left side term of the equation represent the number of neutrons that pass from  $|k_i\rangle$  to  $|k_f\rangle$  with  $\hbar\omega$  exchange; dividing this term by N we get the probability of transition from  $i$  to  $f$  state for one particle.

$$W_{fi} = \frac{d^3N}{\hbar d\omega d\Omega dt} \frac{1}{N} \quad (2.10)$$

This probability can be calculated using the Fermi's golden rule (time-dependent perturbation theory). In this case we can describe our system composed by the neutron and scattering centre with the Hamiltonian

$$H = H_0 + V(t) \quad (2.11)$$

Where  $H_0$  is the unperturbed Hamiltonian and  $V(t)$  is the interaction potential probe-target that is turned on when they interact.

$$V(t) = \begin{cases} 0 & t \leq 0 \\ V & t > 0 \end{cases}$$

The interaction takes place when the neutron feels the nuclear field of atoms which constitute the sample. The interaction time is  $10^{-18}s$ , residual strong interaction. With this preliminaries using the Fermi's golden rule

$$W_{fi} = \frac{2\pi}{\hbar} |\langle \psi_f | V | \psi_i \rangle|^2 \delta(\hbar\omega - \hbar\omega_{fi}) \quad (2.12)$$

Where  $|\psi_i\rangle$  and  $|\psi_f\rangle$  are the asymptotic state of the total system (sample-probe) that can be decoupled in the product of the sample and probe state

$$|\psi_i\rangle = |i, k_i\rangle = |i\rangle |k_i\rangle$$

$$|\psi_f\rangle = |f, k_f\rangle = |f\rangle |k_f\rangle$$

In order to obtain an expression for  $W_{fi}$ , Fermi noticed that the neutron scattering was not dependent on the scattering angle and strictly localized. Fermi introduced a pseudopotential of the form

$$V = \sum_{l=1}^N v(\mathbf{r} - \mathbf{r}_l) = \frac{2\pi\hbar^2}{m} b \sum_{l=1}^N \delta(\mathbf{r} - \mathbf{r}_l) \quad (2.13)$$

Where  $b$  is the scattering length (the dimension of the nucleus seen by neutron),  $m$  is the neutron mass and the delta function express the localization of the target. Using eq. 2.9 and eq. 2.10 we get

$$W_{fi} \frac{mV}{P_i} = \frac{d^2\sigma}{\hbar d\omega d\Omega} \quad (2.14)$$

In this expression we can substitute  $W_{fi}$  in eq. 2.12 with the Fermi's pseudopotential and asymptotic states obtaining

$$\begin{aligned} W_{fi} &= \frac{2\pi}{\hbar} |\langle f, k_f | V | i, k_i \rangle|^2 \delta(\hbar\omega - \hbar\omega_{fi}) = \\ &= \frac{2\pi}{\hbar} \left| \frac{2\pi\hbar^2}{m} \frac{b}{V} \langle f | \sum_{l=1}^N \int d\mathbf{r} \delta(\mathbf{r} - \mathbf{r}_l) e^{i\mathbf{k}_i \cdot \mathbf{r}} e^{-i\mathbf{k}_f \cdot \mathbf{r}} | i \rangle \right|^2 \delta(\hbar\omega - \hbar\omega_{fi}) = \\ &= \frac{2\pi}{\hbar} |\langle f | \sum_{l=1}^N e^{i\mathbf{q} \cdot \mathbf{r}_l} | i \rangle|^2 \delta(\hbar\omega - \hbar\omega_{fi}) \end{aligned} \quad (2.15)$$

To get the complete expression, for each  $k_i$ , we have to consider all the possible final states of neutron and sample after the scattering and all the possible initial states of the sample. First we can consider the density of states of neutrons after the scattering process

$$dn = \frac{V}{(2\pi\hbar)^3} \hbar^3 d^3k_f = \frac{V}{(2\pi\hbar)^3} k_f^2 dk_f d\Omega \quad (2.16)$$

Because of the relation

$$\hbar d\omega_f = \frac{\hbar^2 K_f}{m} dk_f$$

we get

$$dn = \frac{V}{(2\pi)^3} \frac{m}{\hbar} d\omega_f d\Omega \rightarrow \frac{d^2 n}{\hbar d\omega_f d\Omega} = \frac{V}{(2\pi)^3} \frac{k_f}{\hbar^2} m \quad (2.17)$$

Multiplying eq. 2.15 with 2.17, summing on the final states of sample and averaging on the initial state of sample and using eq. 2.14 we obtain an expression for the double differential cross section called master equation for neutron scattering

$$\frac{d^2 \sigma}{\hbar d\omega d\Omega} = \frac{k_f}{k_i} b^2 \sum_i \hat{P}_i \sum_f |\langle f | \rho_q | i \rangle|^2 \delta(\hbar\omega - \hbar\omega_{fi}) \quad (2.18)$$

Where  $\rho_q = \sum_{l=1}^N e^{i\mathbf{q}\cdot\mathbf{r}_l}$  is the density operator  $\hat{P}_i$  is the probability of the sample to be in a initial state  $i$ . Now we can use the integral expression for the delta function

$$\delta(\omega) = \frac{1}{2\pi} \int_{-\infty}^{\infty} dt e^{i\omega t}$$

obtaining

$$\frac{d^2 \sigma}{\hbar d\omega d\Omega} = \frac{k_f}{k_i} \frac{b^2}{2\pi} \sum_i \hat{P}_i \sum_f \int_{-\infty}^{\infty} dt e^{i\omega t} e^{-i(\omega_i - \omega_f)t} |\langle f | \rho_q | i \rangle|^2 \quad (2.19)$$

For the energy conservation

$$E_0 + \hbar\omega_i = E_1 + \hbar\omega_f \rightarrow \hbar(\omega_i - \omega_f) = E_1 - E_0$$

with

$$H_{target} |i\rangle = E_0 |i\rangle$$

$$H_{target} |f\rangle = E_1 |f\rangle$$

using it we can rewrite

$$e^{\frac{i}{\hbar}(E_0 - E_1)t} |\langle f | \rho_q | i \rangle|^2 = \langle i | \rho_{-q} | f \rangle \langle f | e^{\frac{i}{\hbar} H_{target} t} \rho_q e^{-\frac{i}{\hbar} H_{target} t} | i \rangle = \langle i | \rho_{-q}(0) | f \rangle \langle f | \rho_q(t) | i \rangle \quad (2.20)$$

Where we have used the Heisenberg representation for the density operator in the last step. In this way the 2.19 become

$$\frac{d^2 \sigma}{\hbar d\omega d\Omega} = \frac{k_f}{k_i} \frac{b^2}{2\pi} \int_{-\infty}^{\infty} dt \sum_i \hat{P}_i \langle i | \rho_{-q}(0) \rho_q(t) | i \rangle e^{i\omega t} \quad (2.21)$$

This expression can be written introducing the dynamical structure factor  $S(\mathbf{q}, \omega)$

$$\frac{d^2 \sigma}{\hbar d\omega d\Omega} = \frac{k_f}{k_i} b^2 N S(\mathbf{q}, \omega) \quad (2.22)$$

Here after we will treat with the dynamical structure factor keeping in mind the relation with the cross section. Up to now we have considered  $b$ , the scattering length, as constant in the sample but it is not the most general case. Taking into account that the scattering length is different for different scattering centre (different element, spin, different isotopes) we obtain for  $S(\mathbf{q}, \omega)$

$$S(\mathbf{q}, \omega) = \langle b^2 \rangle S_S(\mathbf{q}, \omega) + \langle b \rangle^2 S_D(\mathbf{q}, \omega) \quad (2.23)$$

Where the first term gives the contribution due to the self-correlation of the atom at the time 0 and  $t$  and the second term gives the contribution of the correlation between one atom at time 0 with another atom at time  $t$ . Rewriting eq. 2.23 introducing  $S_{S+D}$  we get

$$S(\mathbf{q}, \omega) = \langle b \rangle^2 S(\mathbf{q}, \omega)_{S+D} + [\langle b^2 \rangle - \langle b \rangle^2] S(\mathbf{q}, \omega)_S \quad (2.24)$$

$S(\mathbf{q}, \omega)_{S+D}$  is the coherent term from self and distinct correlation and  $S(\mathbf{q}, \omega)_S$  is the incoherent term only from self correlation.

We can see from eq. 2.24 that in general for a certain  $\mathbf{q}$  one has a coherent and incoherent scattering which are profoundly different. In the coherent scattering there is an interference between the waves scattered. In the incoherent scattering there is no interference at all. Physically we can think of the coherent and incoherent scattering as follows: because the scattering length varies from one isotope to another, the neutron is not affected by a uniform scattering potential but the scattering varies from one point to the next. It is only the average scattering potential that can give interference effect; this average scattering potential is proportional to  $\langle b \rangle$  and hence the coherent scattering cross-section is proportional to  $\langle b \rangle^2$ . The deviations from the average potential are randomly distributed and therefore cannot give interference effects; they therefore give incoherent scattering proportional to the mean square deviation (deviation from the average  $\langle b \rangle$ , i.e. to  $\langle (b - \langle b \rangle)^2 \rangle = \langle b^2 \rangle - \langle b \rangle^2$ ).

### 2.3 Deep Inelastic Neutron Scattering

We can consider now a particular case of the neutron scattering, the Deep Inelastic Neutron Scattering (DINS). It is similar to the Compton effect but using neutrons. In fact in the Compton effect a photon with high energy impinges on a bound electron; the energy of the photon is so high that after the scattering the electron has a free recoil. This event is sensitive to the momentum of the electron before the scattering. We can imagine to do the same thing using neutrons instead of photons and nuclei instead of electrons. The recoil energy is

$$\hbar\omega_r = \frac{\hbar^2 q^2}{2M} \quad (2.25)$$

Where  $M$  is mass of the struck atom. It is obvious that for small masses (hydrogen for example) the recoil energy is very high.

We can now specialize eq. 2.22 for DINS case. In fact when the energy of the incident neutron is higher than any characteristic energy of excitations in the sample, we can apply the Impulse

Approximation (IA). This implies the neglect of any force in the atom after the interaction, and its position vector can be approximated by

$$\mathbf{r}(t) \sim \mathbf{r}(0) + \frac{t}{M} \mathbf{P} \quad (2.26)$$

with  $M$  mass of the struck atom. This approximation is motivated by the fact that energetic neutrons spend a poor time in the sample so the most important effect are at small time. In this case we are studying the vibration of atoms at the bottom of the interatomic potential, with a very small characteristic length ( $< \text{\AA}$ ). In this way we get a particular expression for the dynamical structure factor considering only one atomic mass ( $M$ )

$$S(\mathbf{q}, \omega)_{IA} = \frac{1}{4\pi\hbar} \int_{-\infty}^{\infty} d\mathbf{p} n(\mathbf{p}) \delta(\omega - \frac{\hbar q^2}{2M} - \frac{\hbar}{M} \mathbf{q} \cdot \mathbf{p}) \quad (2.27)$$

where  $n(\mathbf{p})$  is the momentum distribution function of atoms in the sample. In fact the most important application is the measurement of the probability distribution of the atomic momentum.

A particular and explicative example is the a non interacting Bose-Einstein<sup>1</sup> condensate where the momentum distribution of the particles is a delta function for zero temperature see ref. [14]. In this case we have a delta function also for  $S(q, \omega)$  in correspondence of the recoil energy  $\hbar\omega_r$ .

In the other cases the momentum distribution is weighting  $S(\mathbf{q}, \omega)$  obtaining a peak centred at the recoil energy but broadened by the momentum distribution (see DINS peak in fig. 2.2) which is one of the most straightforward observable in DINS experiments. A consequence is that our measurement should be precise not only to individuate the centroid of the peak but also its line shape.

The information obtained has a very important physical meaning because it can be studied the interatomic potential and the average kinetic energy which is

$$\langle E_k \rangle = \frac{3}{2M} \int p^2 n(\mathbf{p}) d\mathbf{p}$$

In other words DINS experiments can be seen as a moving billiard game (see fig. 2.3). In fact we can image that the white ball is the neutron and the moving coloured balls are the atoms: studying the scattering between the white ball and the moving coloured balls we can have information of the momentum distribution of the coloured balls before the scattering; in the same way studying the scattering between neutron and atoms we can go back to the momentum distribution of atoms.

---

<sup>1</sup>The interaction between the particle of the system, the temperature and the zero point energy broaden the momentum distribution because to find the probability that a particle is characterized by a momentum between  $\mathbf{p}$  and  $\mathbf{p}+d\mathbf{p}$  we should integrate the probability density  $n(\mathbf{p})$  in that range.

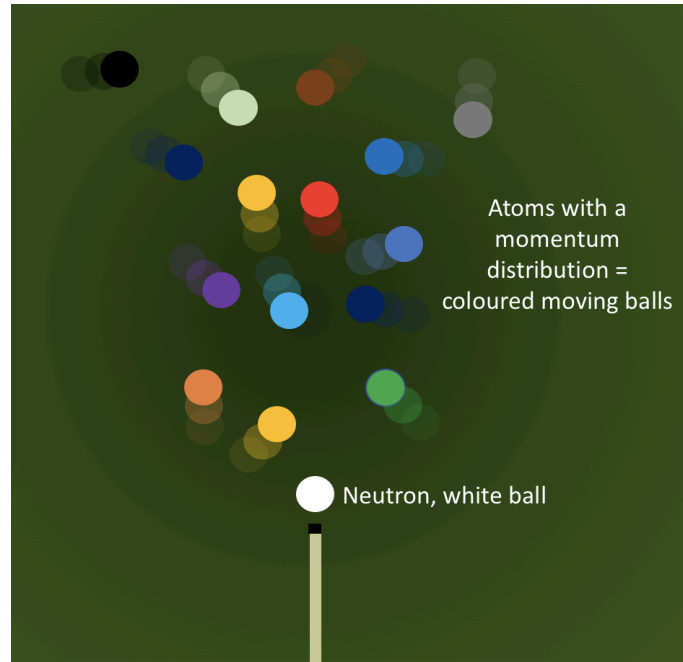


FIGURE 2.3: DINS as a billiards game

In the IA, the scattering variables,  $\mathbf{q}$  and  $E$  are coupled by introducing the *West* variable, which is a measure of the atomic momentum component along the direction of  $\mathbf{q}$

$$y = \frac{1}{\hbar} \mathbf{p} \cdot \hat{\mathbf{q}} \quad (2.28)$$

The new variable  $y$  is the momentum  $\mathbf{p}$  of the nucleus in the initial state projected onto the scattering vector  $\mathbf{q}$  and  $\hat{\mathbf{q}}$  is a unit vector in the direction of the momentum transfer. Therefore, the dynamic structure factor can be rewritten in terms of the new variable via

$$S_{IA}(\mathbf{q}, \omega) = \frac{M}{\hbar q} J_{IA}(y, \hat{\mathbf{q}}) \quad (2.29)$$

The function  $J_{IA}(y, \hat{\mathbf{q}})$  is called the *Neutron Compton Profile* (NCP)

$$J_{IA}(y, \hat{\mathbf{q}}) = \hbar \int d\mathbf{p} n(\mathbf{p}) \delta(\hbar y - \mathbf{p} \cdot \hat{\mathbf{q}}) \quad (2.30)$$

It gives the probability that an atom has a momentum of magnitude between  $\hbar y$  and  $\hbar(y + dy)$ . The NCP is very useful because it connects momentum and energy exchanged in the process; in this way we have obtained a quantity independent on the magnitude of  $\mathbf{q}$  which gives information on the atom momentum distribution centred in  $y = 0$  for any  $\mathbf{q}$  exchanged; it is important because we will be able to sum spectra were different  $\mathbf{q}$  value are involved.

## 2.4 Other neutron reactions

Up to now we have studied only one type of reaction between neutrons and condensed matter. There are other physical phenomena other than the scattering which will be important to

explain experimental techniques in the next chapters. In fact the n-interactions of the neutron with condensed matter can be classified as scattering or absorption reactions. Related to the scattering we can have Elastic or Inelastic scattering. In scattering processes change in energy and direction of the incident neutron can occur, but the nucleus is left with the same number of protons and neutrons. On the contrary, for the absorption we have a nuclear reaction which leads to the disappearance of free neutrons and a wide range of radiations emitted or fission can be induced. The different types of interactions are summarized in fig. 2.4.

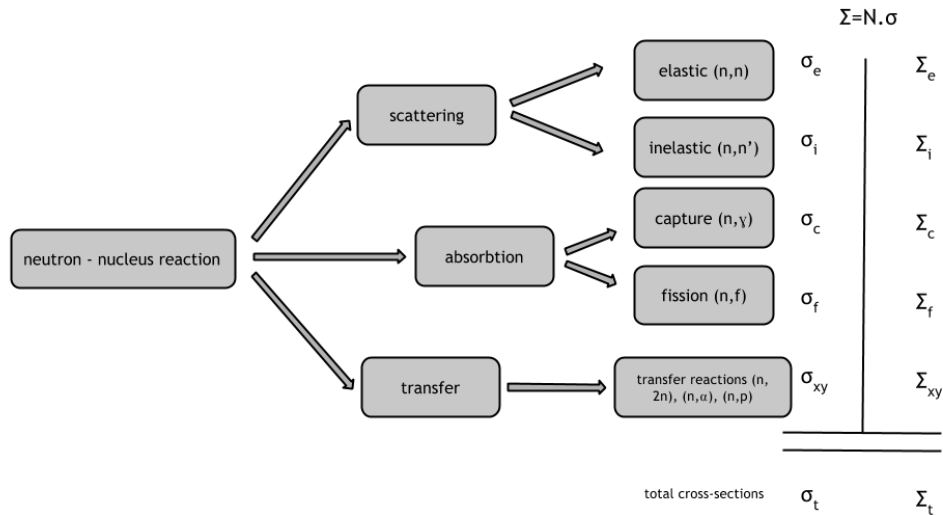
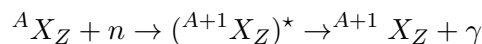


FIGURE 2.4: Types of interaction between neutron and nucleus

In particular we are interested in the radiative neutron capture  $(n, \gamma)$ . The absorption of the neutron by a nucleus which ends with an emission of gamma rays within a very short time ( $\sim 10^{-14} s$ ) is called *radiative capture*. The capture reaction can be modelled as the formation and decay of a compound nucleus following the reaction



There are three different regions in the radiative capture reaction that we can see in fig.2.5. For low energy neutrons, before the first capture resonance,  $\sigma_\gamma$  is approximately  $1/v$  where  $v$  is the velocity of the neutron. After this region we can find isolated resonances and the radiative cross section assume the shape of the typical Breit-Wigner resonance. This region of isolated resonances begins in the keV region in medium weighted nuclei, in the MeV region in light nuclei and in the eV region for very heavy non-magnetic nuclei. Finally at higher energies ( $\sim MeV$ ) the resonances start to overlap and it becomes impossible to distinguish them, in addition to that, other reactions begin to intervene in competition with the radiative capture for their share of the compound nucleus cross section. The result of this behaviour is a decrease of  $\sigma_\gamma$  to very low values at high energies. After the emission of prompt  $\gamma$  rays the  $(A+1)$  isotope is, in most of cases,  $\beta$  unstable; it means an emission of  $e^-$  or  $e^+$  with a consequent  $\gamma$  emission if the new element is in excited configuration (see fig. 2.6 and 2.7). This delayed emission is completely random in time for the stochastic nature of the process.

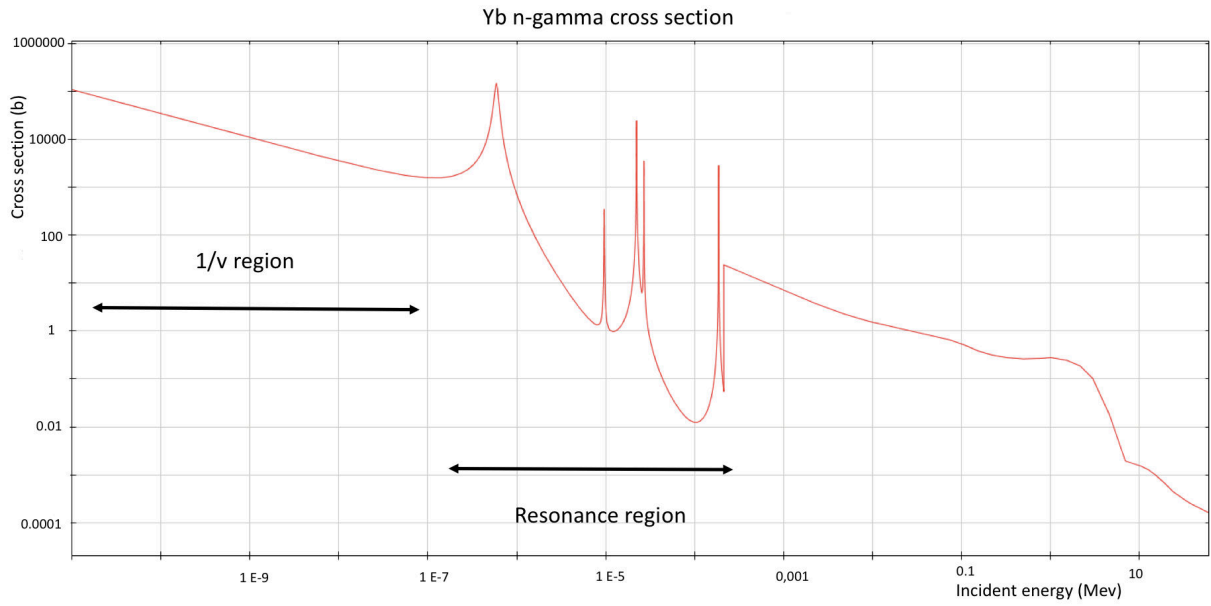


FIGURE 2.5: Radiative capture cross section of Yb as a function of neutron incident energy, ref.[15].

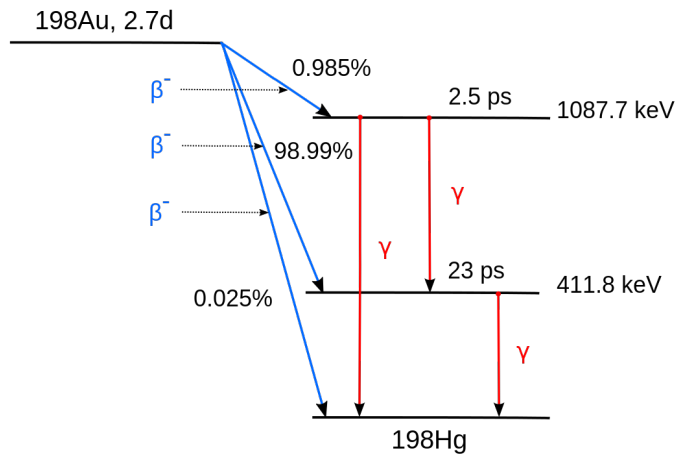


FIGURE 2.6: Decay scheme of  $^{198}\text{Au}$  after the radiative capture of  $^{197}\text{Au}$

For our purposes will be used, as we will see, the radiative neutron capture of a gold ( $^{197}\text{Au}$ ) foil which has a large resonance at  $4.9 \pm 0.15\text{eV}$ .

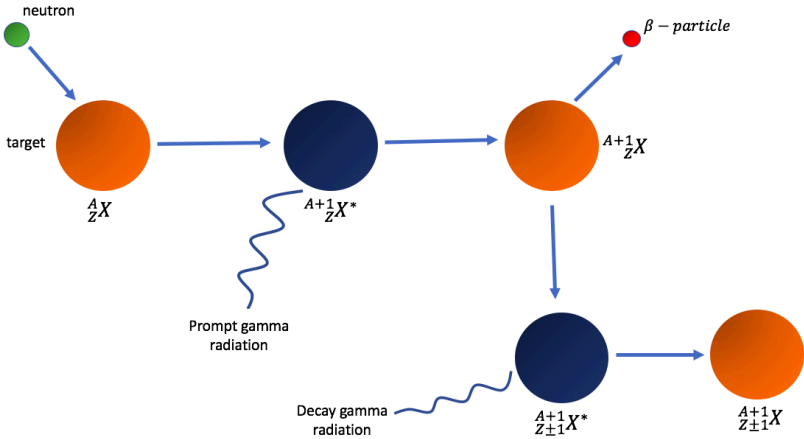


FIGURE 2.7: Scheme of the radiative neutron capture

## Chapter 3

# Sources and instrumentation

### 3.1 Neutron Sources and Facilities

One might think it is not necessary to have any detailed knowledge of the neutron source in order to use the techniques of neutron scattering or imaging. To an extent this is true. However, the distribution of neutrons from the source in terms of energy and time, and the distribution of "background" (fast neutrons, delayed neutrons, gammas, ...), has a direct bearing on the design of neutron scattering and imaging instruments and their performance, on how measured "raw" data must be corrected to make them scientifically meaningful, and on the types of measurements that can be undertaken. Even if the average user does not design the instrument, the user needs to choose the source/instrument to be used for a particular experiment or measurement, so some knowledge of the different types of sources is advisable. There are two kinds of neutron sources for neutron scattering :

- reactor sources
- large accelerator-based neutron sources

Nuclear reactors use the fission process to produce neutrons. Most of the current reactor sources for scattering applications were built in the 1960s and 1970s and were primarily designed for materials testing for the nuclear industry, providing medium flux. The best reactor source, optimized for neutron scattering applications, is still the High-Flux Reactor (HFR) at the Institut Laue-Langevin (ILL), built in 1972 in Grenoble, France. Neutrons can also be produced by the spallation process, in which high-energy protons strike a solid target. The development of proton accelerator technology, driven by other applications such as particle physics, helped to increase the potential power and hence the neutron flux of spallation sources. The pulsed nature of most accelerator-based neutron sources can offer a significant advantage in experiments using the time of flight (TOF) method, in which the speed of the neutron is measured by timing its flight from the source to the detector. One of the most important pulsed proton driven neutron sources is the ISIS facility, near Oxford, UK. Both fission and spallation produce neutrons in the megaelectron volt energy range. However, neutron scattering and most neutron imaging applications require neutrons at electron volt or lower energies. Moderators are used to slow the neutrons to these energies. Reactor technology is highly developed and has not changed significantly for many years. The technologies for accelerator-driven sources offer many more parameters that can be varied to optimize the source for different purposes.

### 3.1.1 Reactors

At research nuclear reactors, neutrons are produced by the well-known fission process shown in fig. 3.1



with  $\sim 200\text{MeV}$  energy release and  $\sim 2\text{MeV}$  kinetic energy for each neutron.  $X$  and  $Y$  are fission fragments or atoms of smaller atomic weight. Power reactors are optimized for heat extraction and efficient use of fuel, so they have quite a different design from research reactors that are optimized for high (external) thermal neutron flux. In a typical research reactor design, one of the neutrons produced per fission is needed to sustain the chain reaction,  $\sim 0.5$  is lost, and one is available for external use. Anyway, the future development of high-flux neutron sources will be based on accelerators.

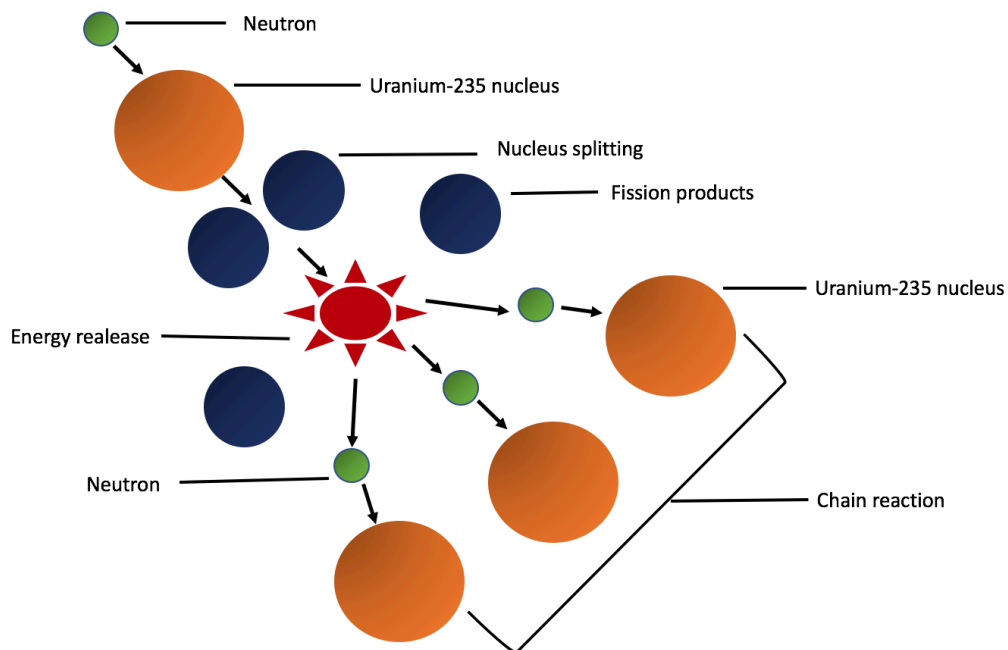


FIGURE 3.1: Scheme of neutron production at reactors

### 3.1.2 Proton Accelerator-Based Sources

High-energy protons can create large numbers of *spalled* neutrons from bombardment of heavy nuclei. For example, a 1 GeV proton is capable of producing approximately 25 neutrons from a lead target, with heat deposition in the target of about half of the proton beam power, meaning one order of magnitude less heat must be dissipated than in a fission reaction producing the same time-averaged neutron flux. Spallation reactions occur for proton energies above 100 MeV. High-energy neutrons, pions, and spalled nuclei cause inter-nuclear cascades followed by low-energy neutron evaporation from the excited nuclei, as illustrated in fig. 3.2

The energy of a small fraction of the neutrons produced in spallation processes can be as high as the incident proton energy (these neutrons require very thick shielding), but the spectrum

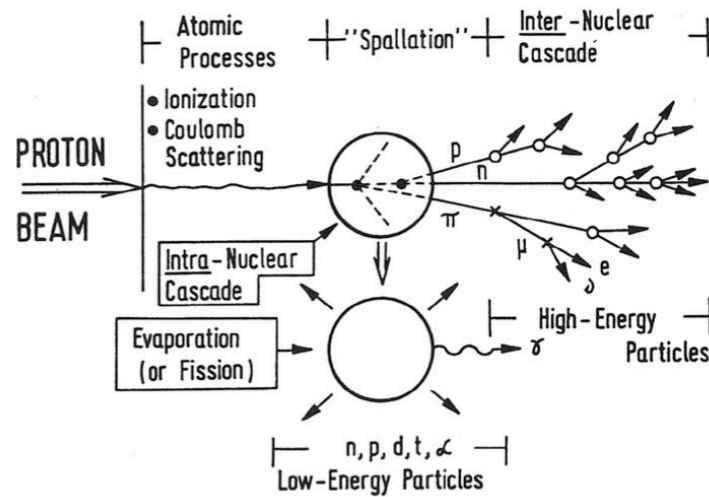


FIGURE 3.2: Scheme of neutron production using spallation process, ref.[16].

reaches a maximum of around 2 MeV for the evaporating neutrons, as shown in fig 3.3. For efficient neutron production, as many protons as possible should undergo high-energy collisions with nuclei rather than gradually losing energy through other processes.

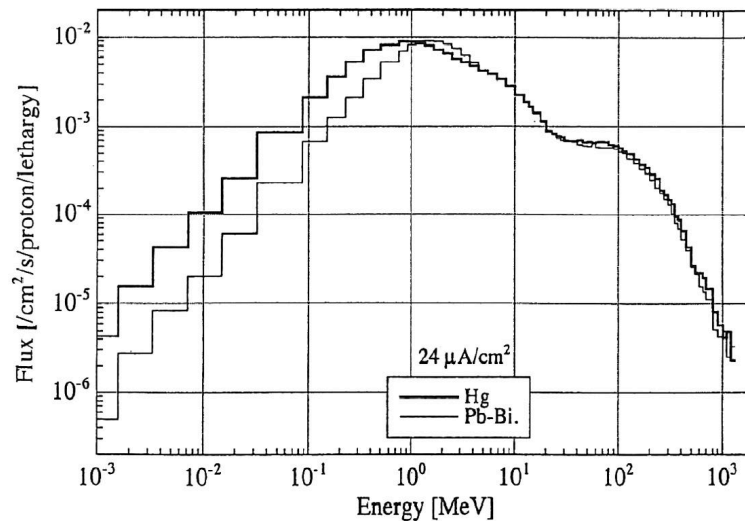


FIGURE 3.3: Neutron energy spectrum in a spallation neutron source, ref. [16].

In the early days of design work on spallation sources, proton energies were less than 1 GeV because of the lack of experimental experience at higher energies. However, more sophisticated codes and experiments in the 1990s demonstrated that the neutron production rate is almost proportional to the accelerator power even at 12 GeV.

For a short-pulse neutron source, the repetition rate of the proton acceleration is an important parameter to be considered. When a long neutron flight path is used for improved TOF resolution, a slow repetition rate is important to minimize frame overlap (where the fast neutrons from one pulse overlap with the slow neutrons from the previous pulse). However, if the same

time-averaged power is maintained, a lower repetition rate requires more power per pulse, creating a more difficult engineering problem for the accelerator and target. Most accelerator-based neutron sources are pulsed, and heat is produced in the target only during the pulses. This allows the heat to dissipate slowly in the period between pulses, so the instantaneous power and neutron flux can be very high. However, thermal shock in the target remains a problem to be overcome at the highest levels of proton power. Building spallation neutron sources instead of reactors is therefore becoming a worldwide trend.

### 3.1.3 Moderation Mechanisms for Spallation Sources

In designing spallation sources, as much consideration should be paid to the moderators as to the accelerator performance. The design of moderators is strongly dependent on the kinds of instruments, resolution, and intensity that are required. Among the most important parameters to be optimized for moderators are

- temperature
- neutronic structure
- materials

Neutrons in moderators reach thermal equilibrium after multiple scattering events and have, in the case of sufficiently thick moderators, a Maxwellian distribution in energy around the temperature of the moderator. On the other hand, for pulsed sources, the time that neutrons spend in the moderator broadens the pulse. Short-pulse spallation sources need to have a sharp pulse structure of thermalized neutrons, so the moderator dimensions need to be small and are optimized at around  $10 \times 10 \times 10 \text{ cm}^3$ . The under-moderated neutrons result in a rich epithermal flux, proportional to  $1/E$  where  $E$  is the energy of the neutrons, in the higher energy slowing down region above the Maxwellian distribution fig. 3.4.

Low-temperature moderators can extend the slowing-down region to shift the Maxwell distribution to lower energy, although flux is sacrificed in the thermal energy region. The pulse width is a key parameter for short-pulse spallation sources and it directly influence the neutron beam instrument performance. For example pulse widths can be reduced by surrounding the moderator with an absorbing material (decoupler) such as cadmium on all sides except the side from which the neutron beam emerges. This prevents the neutrons slowed down in the reflector from entering the moderator and emerging as part of the neutron beam. Since those neutrons would typically emerge into the beam later than would the neutrons slowed down in the moderator, such decoupling prevents the extra broadening of the neutron pulse that would result from such neutrons.

The pulsed nature of the source allows for using the time of flight (henceforth called TOF) technique for the kinematic reconstruction of the scattering process (i.e. to define energy and wave vector transfer). In the following section a brief description of the TOF technique is presented.

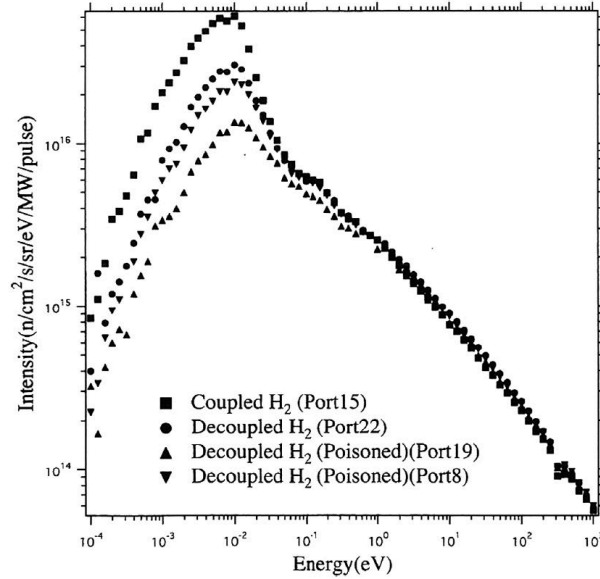


FIGURE 3.4: The neutron energy distribution (flux). The flux consists of a Maxwell distribution at low energies and a  $1/E$  region at higher energies, ref. [16]

## 3.2 Basic principles of the time-of-flight technique

The total neutron TOF  $t$  is the time that a neutron takes to travel from the moderator to the detector. It can be written as:

$$t = t_0 + \frac{L_0}{v_0} + \frac{L_1}{v_1} \quad (3.2)$$

where  $t_0$  is a fixed electronic time delay,  $L_0$  and  $L_1$  are the incident and scattering flight paths of the instrument, while  $v_0$  and  $v_1$  are associated to the initial and final neutron energy, respectively. Figure 3.5 represents a schematic drawing of an instrument, where the geometrical parameters are clearly indicated. TOF technique requires the knowledge of  $L_0$ ,  $L_1$ , the scattering angle  $\theta$  and of the initial or the final neutron energy ( $E_0$  or  $E_1$ ) to reconstruct the kinematic of the scattering process.

By knowing the initial (final) energy, the total neutron TOF allows for the measurement of the final (initial) one, while the detector angular position ( $\theta$ ) allows for the determination of the wave vector transfer,  $\mathbf{q}$ . The TOF acquisition chain can briefly be described as follows: before the proton bunch impinges on the heavy metal spallation target, a proton beam monitor, placed close to the target, triggers the opening of a time gate ( $t = t_{start}$ ) of fixed duration  $\delta t = 20ms$ . During  $\delta t$  the acquisition electronics of an instrument is enabled to process the electric signals provided by neutron detection system (neutron counters). Each signal is stored in a time channel of a Time to Digital Converter (TDC), its value being the time difference between the initial time of the gate  $t_{start}$  (approximately corresponding to the instant the neutron leaves the moderator) and the detection instant ( $t_{stop}$ ). A fixed time delay  $t_0$  (see eq. 3.2) of about  $5\mu s$  is electronically provided, allowing for the recovery of the detectors of all instruments from the saturation induced by the " $\gamma$  flash", produced in the spallation process.

A typical DINS TOF spectrum is showed in fig. 3.6 where we can see the counts as a function of

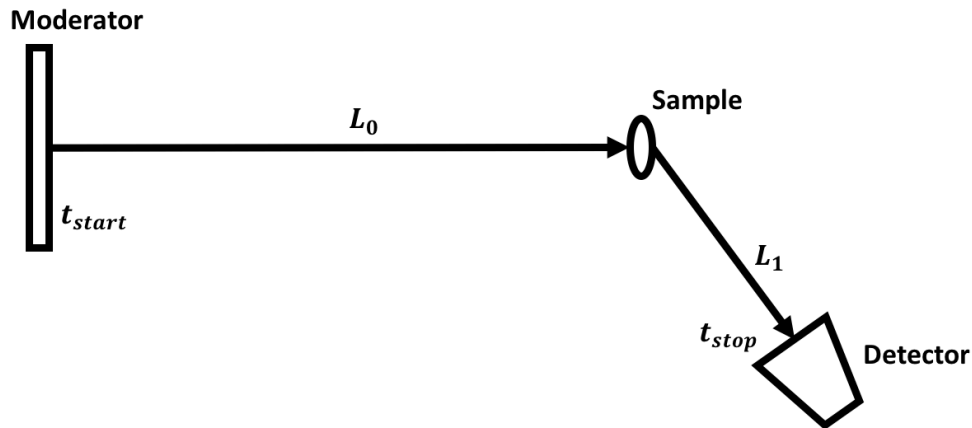


FIGURE 3.5: Scheme of a TOF spectrometer:  $L_0$  is the primary flight path (moderator-sample distance),  $L_1$  is the secondary flight path (sample-detector distance). The  $t_{start}$  and  $t_{stop}$  are provided by the proton beam monitor and the detector, respectively.

the time of flight, in the specific case there are two recoil peaks (polyethylene sample) associated with hydrogen (low TOF) and carbon (high TOF); the hydrogen peak is at lower TOF because hydrogen is lighter than carbon and it is more intense because the cross section of carbon is smaller than the hydrogen one.

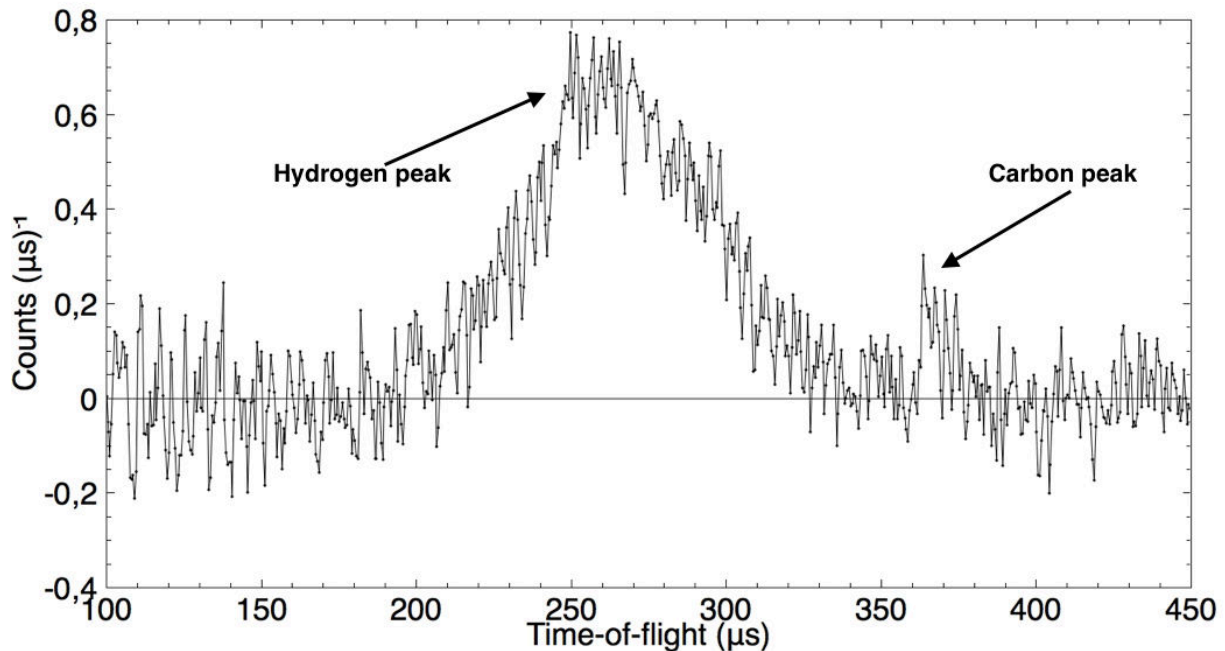


FIGURE 3.6: Example of TOF spectra in a DINS experiment for a polyethylene sample.

This work is focused on an experiment performed at the ISIS facility near Oxford and in the next section I will describe in a more precise way this pulsed neutron source.

### 3.3 ISIS spallation neutron source

The ISIS pulsed neutron source at the Rutherford Appleton Laboratory in Oxfordshire produces beams of neutrons and muons that allow scientists to study materials at the atomic level using a suite of instruments, often described as "super-microscopes". It supports a national and international community of more than 2000 scientists who use neutrons and muons for research in physics, chemistry, materials science, geology, engineering and biology. It is the most productive research centre of its type in the world.

ISIS is made up of many components. The heart of ISIS is an 800 MeV proton accelerator which produces proton bunches every 20 ms.

#### 3.3.1 Ion source

At the very start of the accelerator there is an ion source which produces  $H^-$  ions (negative hydrogen ions - a proton and two electrons) using an electric discharge. The ion source is fed with hydrogen gas together with hot caesium vapour. A discharge plasma is formed, and positively charged ions from the plasma are attracted towards the cathode surfaces. The deposition of caesium reduces the work function of the cathode, making it a more efficient donor of electrons to the positively charged hydrogen ions, thus enhancing  $H^-$  ion production. The  $H^-$  ions are extracted from the ion source in 200  $\mu s$  long pulses to form a beam which is then passed through a magnet to remove any electrons. The  $H^-$  ions acquire an energy of 35 keV across a DC acceleration gap, are focused and monitored in the Low Energy Beam Transport and then passed into the Radio Frequency Quadrupole (RFQ) accelerator where they are accelerated and separated into bunches, it operates at 665 keV, 202.5 MHz.

#### 3.3.2 Linac

Ion bunches are then further accelerated using a linear accelerator with four 10 metre long accelerating tanks in which high intensity radio-frequency (RF) fields accelerate the beam to 70 MeV. The bunches of ions keep in step with the alternating RF electric field, crossing the gaps between the drift tubes when the field is in the correct direction for acceleration, but being shielded inside the drift tubes when the field is in the wrong direction. The linac provides 200  $\mu s$  long, 22 mA  $H^-$  pulses which are transported to the synchrotron. Final acceleration of the beam occurs in the synchrotron. At the end of the linear accelerator, the ions are travelling at 37% of the speed of light.

#### 3.3.3 Synchrotron

Acceleration of the ions continues in the synchrotron, a 163 m circumference ring of powerful magnets that bend and focus the beam into a circle. Ten dipole bending magnets are used to keep the beam travelling around, while quadrupole magnets keep the beam tightly focused. On entry the  $H^-$  beam is stripped of its electrons by a 0.3  $\mu m$  thick aluminium oxide stripping foil. The resulting protons are accumulated in the synchrotron over approximately 130 revolutions. The advantage of this charge exchange injection scheme is that a larger number of protons

( $2.810^{13}$ ) can be accumulated in the synchrotron. Once injection is complete the RF system traps the beam into two bunches and accelerates them to 800 MeV after 10000 orbits of the synchrotron before being kicked into the extracted proton beam line (EPB), delivering  $4 \mu C$  of protons in two 100 ns long pulses to the neutron and muon targets. The entire acceleration process is repeated 50 times per second, so a average current of  $200 \mu A$  is delivered to the targets. In particular there are two target stations: in *target station 1* the current is  $170 \mu A$  and in *target station 2* the remaining  $30 \mu A$ . The ISIS target stations uses the high energy protons produced by the ISIS accelerator to generate neutrons by the spallation process where neutrons are expelled from the nuclei of the target atoms.

### 3.3.4 Target station 1 and muon target

In target station 1 there are 18 beam channels, 9 on each side of the target, which feed the neutron scattering instruments each optimised to explore different properties of materials such as atomic dynamics and arrangements. Neutrons are produced when the 160 kW proton beam from the accelerator hits a metal target. The target is made from a series of thick tungsten plates (clad with tantalum to prevent corrosion). Water cooling channels remove around 90 kW of heat generated in the target. Four moderators are used to slow down fast neutrons escaping from the target to the lower speeds required for neutron scattering experiments. Two use water at room temperature, one uses liquid methane at 100 K and the fourth consists of liquid hydrogen at 20 K. The different temperatures result in different energy neutron beams. The moderators are surrounded by a water-cooled beryllium reflector which scatters neutrons back into the moderators and doubles the useful flux of neutrons. A remote handling cell is used to replace a target or moderator and to perform any required maintenance. In operation, all components become highly radioactive, and the purpose-built cell is integrated into the target station. The cell has a pair of manipulators on each side, and operations are viewed through large shielding windows and video cameras.

Muons are produced in the ISIS target station 1 by colliding the proton beam with a 10 mm thick carbon target 20 m upstream of the neutron target. Collisions produce pions which decay with a mean lifetime of 26 ns into muons. The muon beam is fully polarised, and this polarisation is maintained as the beam is transported to the muon spectrometers. The muon target uses 2-3% of the proton beam.

$$\pi^+ \rightarrow \mu^+ + \nu_\mu$$

$$\pi^- \rightarrow \mu^- + \bar{\nu}_\mu$$

### 3.3.5 Target station 2

The ISIS Second Target Station is a low-power neutron source optimised to maximise the production of long wavelength neutrons. It is required to produce neutrons of two pulse shape varieties. The first, a wide pulse shape with full width at half-maximum height (FWHM) no

bigger than  $300 \mu\text{s}$  and a modest tail, is generated by a coupled moderator; whilst the second is a simple pulse shape de-coupled moderator, with little or no tail, and a width comparable to those of the existing ISIS methane and hydrogen moderators ( $30 - 50 \mu\text{s}$ ).

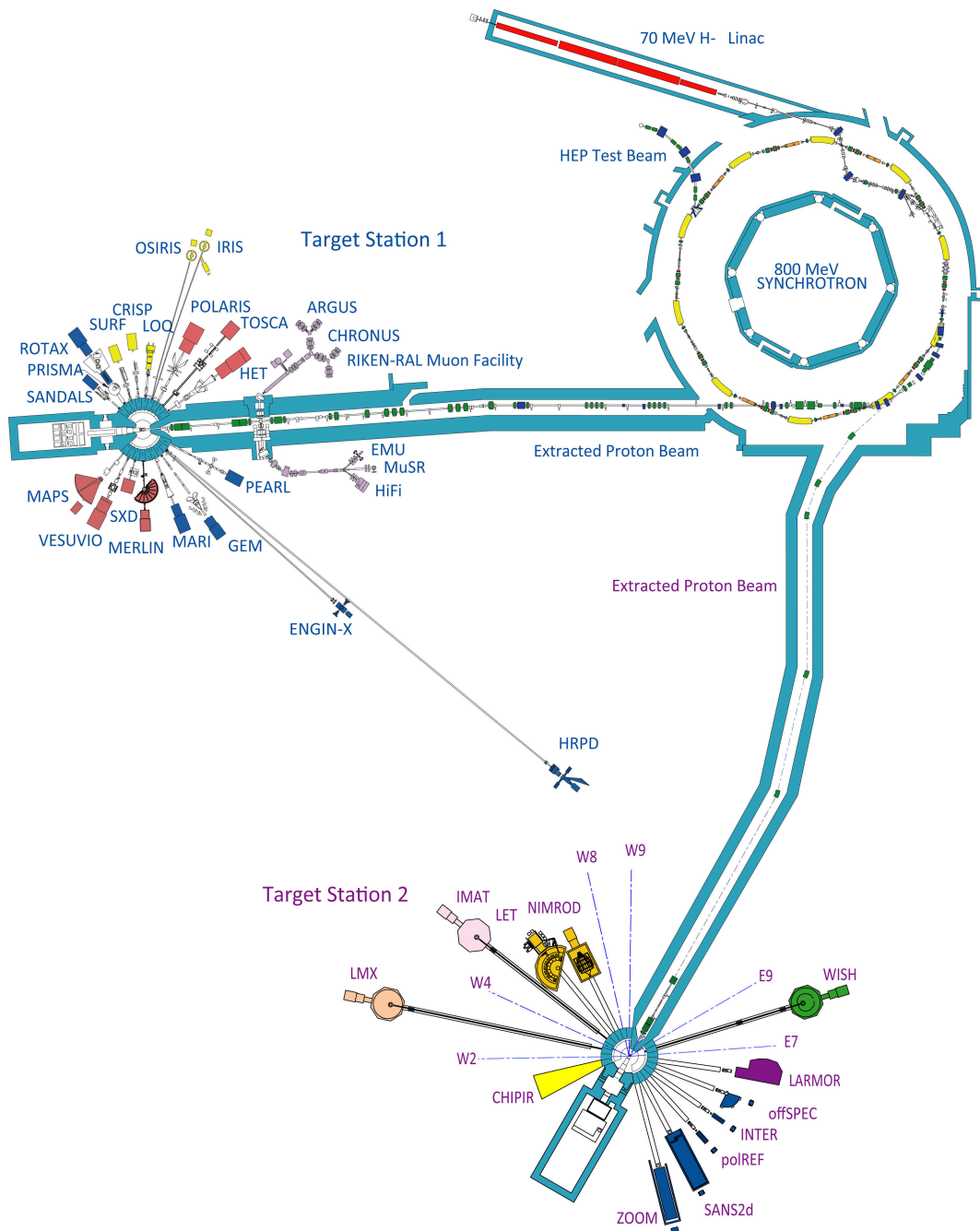


FIGURE 3.7: Scheme of ISIS target stations, ref. [17]

The main object of this thesis is the improvement of the detection system of a specific spectrometer of the ISIS facility: VESUVIO.

## Chapter 4

# The VESUVIO spectrometer

To reconstruct the kinematics in an inelastic scattering measurement, the initial and final neutron energies (wave vector) have to be calculated. The wave vector,  $\mathbf{q}$ , and energy transfer,  $\hbar\omega$ , can be then calculated imposing wave vector and energy conservation:

$$\mathbf{q} = \mathbf{k}_i - \mathbf{k}_f \quad (4.1)$$

$$\hbar\omega = \frac{\hbar^2(k_i^2 - k_f^2)}{2m} = E_i - E_f \quad (4.2)$$

$k_i$  and  $k_f$  being the initial and final neutron wave vectors, and  $m$  the neutron mass, respectively. The conservation laws apply rather stringent limitations to the values of  $\mathbf{q}$  and  $\hbar\omega$  which may be observed. The relation linking  $\mathbf{q}$  and  $\omega$  can be found starting from the relation:

$$q^2 = k_i^2 + k_f^2 - 2k_i k_f \cos\theta \quad (4.3)$$

or in energy units:

$$\frac{\hbar^2 q^2}{2m} = E_i + E_f - 2\sqrt{E_i E_f} \cos\theta \quad (4.4)$$

In the direct geometry configuration  $E_i$  is selected while for an inverse geometry instrument  $E_f$  is fixed using monochromators or analysers. From a kinematical point of view, the main difference between the direct and inverse configuration is that in the direct geometry the maximum energy loss is limited to  $E_i$ , while there is no limit to the energy loss in the inverse geometry instruments.

VESUVIO is an inverse geometry neutron spectrometer operating at ISIS spallation source since 2002. VESUVIO makes use of a polychromatic incident neutron beam, resulting from the use of a water moderator at 295 K, characterized by an energy spectrum peaked at about 0.03 eV and with an  $E_i^{-0.9}$  tail in the epithermal region shown in fig. 4.1. With VESUVIO we can access a region of  $(\mathbf{q}, \hbar\omega)$  kinematic space characterised by high energy ( $\hbar\omega \geq 1\text{eV}$ ) and high wave vector ( $q \geq 30 \text{ \AA}^{-1}$ ).

The main instrumental parameters of the spectrometer are listed in table 4.1, while figure 4.2 represents a schematic drawings of VESUVIO

Incident neutrons with initial energy  $E_i$  travel over a primary flight path  $L_0$  from the moderator

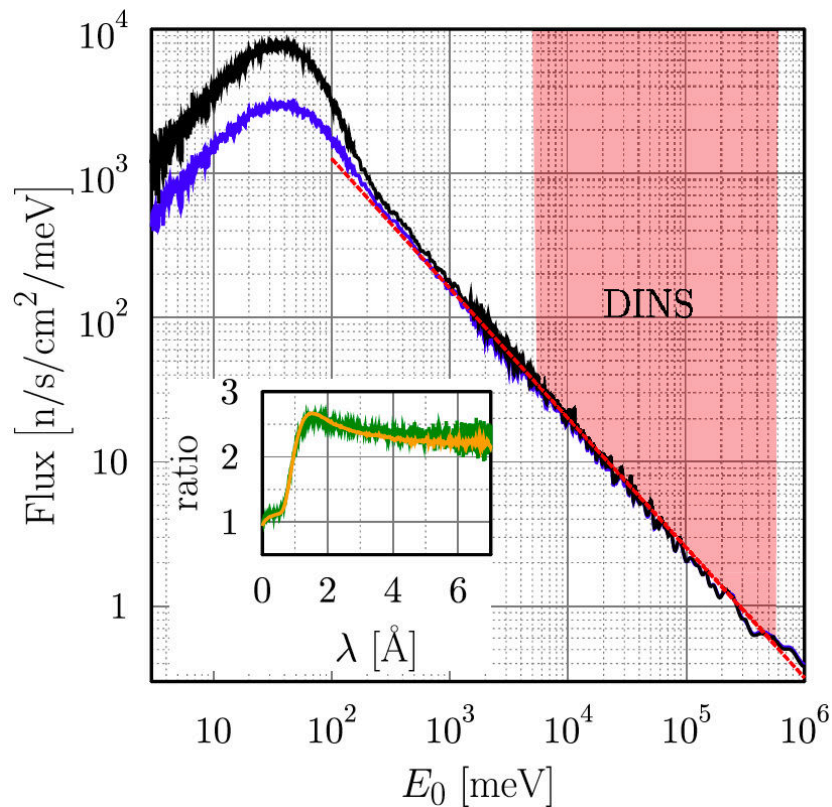


FIGURE 4.1: Incident neutron flux at the sample position at VESUVIO. The blue line is the flux before the moderator upgrade and the black line is the flux after the upgrade. The red dashed line is proportional to  $E^{-0.9}$  and the region shadowed in red represents the energy range used in DINS. The insert shows the spectrum of the incident neutron beam after the upgrade normalised to the spectrum before the change, ref. [18].

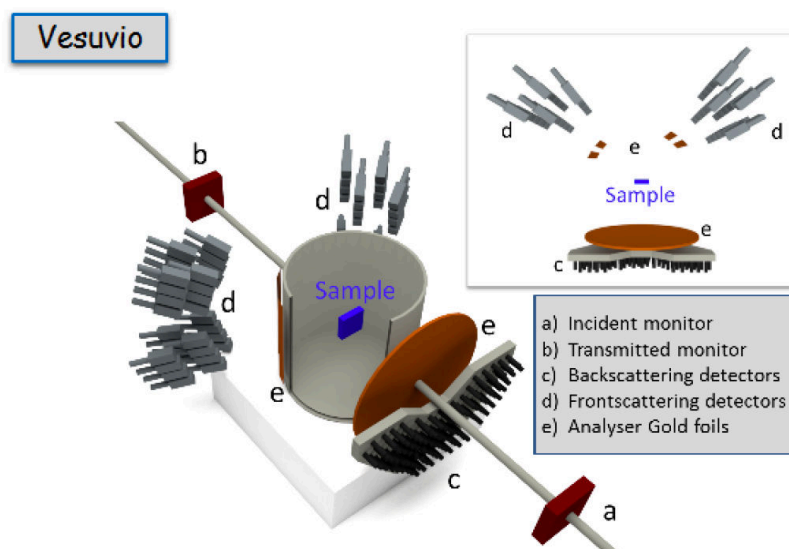


FIGURE 4.2: Schematic drawing of VESUVIO, ref. [19].

to the sample. The sample under study is inside a tank and it can be used a Closed Cycle Refrigerator (CCR) to perform experiments with fixed value of temperature. For example the CCR has

Geometry configuration	Inverse
Energy analysis method	Nuclear resonance
Neutron detectors	$^6\text{Li}$ -glass Cerium activated
$\gamma$ detectors	YAP Cerium activated
$L_0$	$\sim 11m$
$L_1$	$\sim 0.7m$
Forward angular range	$30^\circ$ - $70^\circ$
Backward angular range	$120^\circ$ - $170^\circ$

TABLE 4.1: General characteristics of the VESUVIO spectrometer

a big temperature working range from 5 K to 600 K. After scattering at certain angle, neutrons with final energy  $E_f$  travel over a secondary flight path  $L_1$  to the detector and are counted using different methods. In fact the energy selection and neutron detection on VESUVIO operates in two modes:

- Resonance-Filter (RF) backward detection with  $^6\text{Li}$ -glass (see 4.1.3)
- Resonance-Detector (RD) forward detection with YAP(Ce) (see 4.1.4)

## 4.1 Detectors

As mentioned in the VESUVIO spectrometer two types of detectors are used: YAP and  $^6\text{Li}$ -glass. They are both inorganic scintillators, before the VESUVIO operation method the detection mechanism and pulse processing is described in the following sections.

### 4.1.1 Scintillators

The detection of ionizing radiation by the scintillation light produced in certain materials is one of the oldest techniques on record. The scintillation process remains one of the most useful methods available for the detection and spectroscopy of a wide assortment of radiations. The ideal scintillation material should possess the following properties:

- It should convert the kinetic energy of charged particles, produced for example by photons or neutrons that we want to detect, into detectable light with a high scintillation efficiency
- This conversion should be linear, the light yield should be proportional to deposited energy over as wide a range as possible.
- The medium should be transparent to the wavelength of its own emission for good light collection.
- The decay time of the induced luminescence should be short so that fast signal pulse can be generated.

- Its index of refraction should be near that of glass ( $\sim 1.5$ ) to allow efficient coupling of the scintillation light to a photomultiplier tube or other light sensor.

No material simultaneously meets all these criteria, and the choice of a particular scintillator is always a compromise among these and other factors. The most widely applied scintillators include the inorganic alkali halide crystals, of which sodium iodide is the favourite, and organic based liquids and plastics. The inorganics tend to have the best light output and linearity, but with several exceptions are relatively slow in their response time. Organic scintillators are generally faster but yield less light. The high Z-value of the constituents and high density of inorganic crystals favour their choice for gamma-ray spectroscopy, whereas organics are often preferred for beta spectroscopy and fast neutron detection (because of their hydrogen content). The process of fluorescence is the prompt emission of visible radiation from a substance following its excitation by some means. It is conventional to distinguish several other processes that can also lead to the emission of visible light. Phosphorescence corresponds to the emission of longer wavelength light than fluorescence, and with a characteristic time that is generally much slower. Delayed fluorescence results in the same emission spectrum as prompt fluorescence but again is characterized by a much longer emission time following excitation. To be a good scintillator, a material should convert as large a fraction as possible of the incident radiation energy to prompt fluorescence, while minimizing the generally undesirable contributions for phosphorescence and delayed fluorescence. In most of the cases the scintillators operate in the pulse mode where only the light that contributes to the output is limited to prompt fluorescence. In the VESUVIO spectrometer the scintillators used are inorganic; in particular  $\gamma$ -sensitive YAP(Ce) for forward scattering and  $^6\text{Li}$ -glass neutron sensitive for backward scattering.

#### 4.1.2 Inorganic scintillators

The scintillation mechanism in inorganic materials depends on the energy states determined by the crystal lattice of the material. As shown in fig. 4.3, electrons have available only discrete bands of energy in materials classified as insulators or semiconductors.

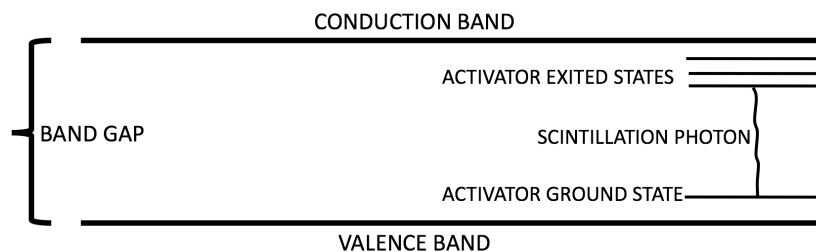


FIGURE 4.3: Energy band structure of an activated crystalline scintillator.

The lower band, called the valence band, represents those electrons that are essentially bound at lattice sites, whereas the conduction band represents those electrons that have sufficient energy to be free to migrate throughout the crystal. There exists an intermediate band of energies, called the forbidden band, in which electrons can never be found in the pure crystal. Absorption of energy can result in the elevation of an electron from its normal position in the valence band across the gap into the conduction band, leaving a hole in the normally filled valence band. In

the pure crystal, the return of the electron to the valence band with the emission of a photon is an inefficient process. Furthermore, typical gap widths are such that the resulting photon would be of too high an energy to lie in the visible range. To enhance the probability of visible photon emission during the de-excitation process, small amounts of an impurity are commonly added to inorganic scintillators. Such deliberately added impurities, called activators, create special sites in the lattice at which the normal energy band structure is modified from that of the pure crystal. As a result, there will be energy states created within the forbidden gap through which the electron can de-excite back to the valence band. Because the energy is less than that of the full forbidden gap, this transition can now give rise to a visible photon and therefore serve as the basis of the scintillation process. These de-excitation sites are called luminescence centres or recombination centres. Their energy structure in the host crystalline lattice determines the emission spectrum of the scintillator.

A charged particle passing through the detection medium will form a large number of electron-hole pairs created by the elevation of electrons from the valence to the conduction band. The positive hole will quickly drift to the location of an activator site and ionize it, because the ionization energy of the impurity will be less than that of a typical lattice site. Meanwhile, the electron is free to migrate through the crystal and will do so until it encounters such an ionized activator. At this point the electron can drop into the activator site, creating a neutral configuration that can have its own set of excited energy states. These states are illustrated in fig. 4.3 as horizontal lines within the forbidden gap. If the activator state that is formed is an excited configuration with an allowed transition to the ground state, its de-excitation will occur very quickly and with high probability for the emission of a corresponding photon. If the activator is properly chosen, this transition can be in the visible energy range. Typical lifetimes for such excited states are of the order of 30-500 ns. It is the decay time of these states that therefore determines the time characteristics of the emitted scintillation light. There are processes that compete with the one just described. For example, the electron upon arriving at the impurity site can create an excited configuration whose transition to the ground state is forbidden. Such states then require an additional increment of energy to raise them to a higher-lying state from which de-excitation to the ground state is possible. One source of this energy is thermal excitation, and the resulting slow component of light is called phosphorescence. It can often be a significant source of background light in scintillators. A third possibility exists when an electron is captured at an activator site. Certain radiationless transitions are possible between some excited states formed by electron capture and the ground state, in which case no visible photon results. Such processes are called quenching and represent loss mechanisms in the conversion of the particle energy to scintillation light. For a wide category of materials, it takes on the average about three times the band-gap energy to create one electron-hole pair. One important consequence of luminescence through activator sites is the fact that the crystal can be transparent to the scintillation light. In the pure crystal, roughly the same energy would be required to excite an electron-hole pair as that liberated when that pair recombines. As a result the emission and absorption spectra will overlap and there will be substantial self absorption. As we have seen, however, the emission from an activated crystal occurs at an activator site where the

energy transition is less than that represented by the creation of the electron-hole pair. As a result the emission spectrum is shifted to longer wavelengths and will not be influenced by the optical absorption band of the bulk of the crystal. To make full use of the scintillation light, the spectrum should fall near the wavelength region of maximum sensitivity for the device used to detect the light. For common inorganic scintillators, the light yield is more nearly proportional to deposited radiation energy than is typically observed in organic scintillators.

### 4.1.3 YAP(Ce)

An X-ray or gamma-ray photon is uncharged and creates no direct ionization or excitation of the material through which it passes. In fact photons interact with electrons of the material ionising them through photoelectric or Compton effect. The detection of gamma rays is therefore critically dependent on causing the gamma-ray photon to undergo an interaction that transfers all or part of the photon energy to an electron in the absorbing material. Because the primary gamma-ray photons are "invisible" to the detector, it is only the fast electrons created in gamma-ray interactions that provide any clue to the nature of the incident gamma rays. These electrons have a maximum energy equal to the energy of the incident gamma-ray photon and will slow down and lose their energy in the same manner as any other fast electron, such as a beta particle. Energy loss is therefore through ionization and excitation of atoms within the absorber material and through bremsstrahlung emission. In order for a detector to serve as a gamma-ray spectrometer, it must carry out two distinct functions. First, it must act as a conversion medium in which incident gamma rays have a reasonable probability of interacting to yield one or more fast electrons; second, it must function as a conventional detector for these secondary electrons.

Beginning in the late 1980s, it was realized that the cerium activator could be incorporated into new categories of crystals, resulting in scintillators with reasonably good to outstanding light yield. The scintillation light is generated when the energy deposited in the crystal is transferred to cerium activator sites, where they undergo a transition from the 5d to 4f states. The principal decay time of the cerium luminescence ranges from about 20 to 80 ns, depending on the host crystal. Thus the timing characteristics of these scintillators occupy an intermediate position between the organics with a few nanosecond decay time and the older inorganics in which it is several hundred nanoseconds. After about two decades of development, it has become evident that both rare earth halides and a range of rare earth oxides are the best scintillator host crystals for cerium activation. The rare earth aluminium perovskites  $YAlO_3$  (or YAP) have shown very good scintillation characteristics. In general, the aluminium perovskites have higher densities, higher indices of refraction, shorter decay times and shorter peak emission wavelengths. YAP displays excellent physical properties of hardness, strength, and inertness that facilitate fabrication and handling. For example, in contrast with many other scintillation materials that are either hygroscopic or fragile, YAP can be cut into thin elements for assembly into arrays for use as a position-sensing scintillator. Small-size crystals show excellent energy resolution for example, 4.4% at 662 keV and at the same time offering outstanding timing resolution as low as 160 ps. A slower component of the decay with about 10  $\mu$ s time constant constitutes

Effective atomic number	36
Density ( $\frac{g}{cm^3}$ )	5.55
Maximum emission $\lambda$ (nm)	350
Refractive index at $\lambda_{max}$	1.94
Light yield ( $\frac{photons}{MeV}$ )	18 $10^4$
Decay time (ns)	27
Hygroscopic	no

TABLE 4.2: General characteristics of the VESUVIO spectrometer

less than 10% of the total intensity. YAP demonstrates excellent proportionality of its light output versus energy gamma rays undergo multiple interactions in the detector. Finally another important characteristic of YAP detectors the absence, in the active medium, of isotopes possessing neutron resonances in the 1-100 eV. These resonances produce a correlated background with the consequent worsening of the signal to background ratio. In table 4.2 the main physical characteristics of YAP(Ce) scintillator are shown.

#### 4.1.4 $^6\text{Li}$ -glass

Neutrons are generally detected through nuclear reactions that result in prompt energetic charged particles such as protons, alpha particles, and so on. In our case we will care only about the detection of a neutron, with no attempt made to measure its kinetic energy. The cross section for the reaction must be as large as possible so that efficient detectors can be built with small dimensions. In our application, intense fields of gamma rays are also found with neutrons and the choice of reaction bears on the ability to discriminate against these gamma rays in the detection process. Of principal importance here is the Q-value of the reaction that determines the energy liberated in the reaction following neutron capture. The higher the Q-value, the greater the energy given to the reaction products, and the easier the task of discriminating against gamma-ray events using simple amplitude discrimination but also higher the Q value (total kinetic energy of the product independent of neutron energy ) higher is the impossibility to distinguish the neutron kinetic energy which would be evident with the difference between the total kinetic energy of the products and the Q value. All the conversion reactions are sufficiently exothermic so that the kinetic energy of the reaction products is determined solely by the Q-value of the reaction and does not reflect the very small incoming energy of the neutron. The distance travelled by the reaction products following their formation also has important consequences in detector design. If we are to capture the full kinetic energy of these products, the detector must be designed with an active volume that is large enough to fully stop the particles. If the detector is large enough so that these losses can be neglected, the response function will be very simple, consisting only of a single full-energy peak as shown in the fig 4.4.

Under these circumstances the detector would exhibit a very flat counting plateau, and the ability to discriminate against low-amplitude events (such as gamma-ray-induced processes)

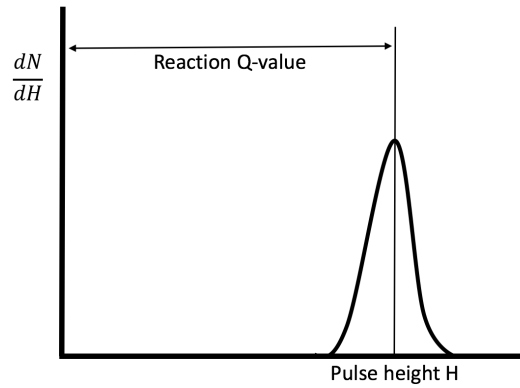
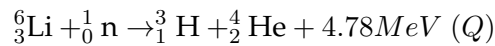


FIGURE 4.4

would be maximized. In our case of  ${}^6\text{Li}$  detectors the principal nuclear reaction is



Calculation of the reaction product energies for negligible incoming neutron energy yields  $E_{3\text{H}} = 2.73\text{MeV}$  and  $E_{4\text{He}} = 2.05$ . This type of detectors are usually used for thermal neutrons in fact to ensure a good detection efficiency at high neutron energies the thickness of the crystals should be scaled proportionally to the variation of the neutron absorption cross section shown in fig 4.5 (typical crystals employed on VESUVIO are 1-2 cm thick). This represents both a technical problem, mostly related to crystal growth techniques (maximum thickness commercially available in the order of 5 cm), and a physical one related to the enhanced background sensitivity of big volume  ${}^6\text{Li}$ -glass detectors which have good  $\gamma$  detection efficiency as well.

#### 4.1.5 Pulse processing

The fundamental output of all the pulse-type radiation detectors, as the scintillators, is a burst of charge  $Q$  liberated by the radiation in the detector. The charge  $Q$  is usually proportional to the energy deposited and is delivered as a transient current  $I(t)$ , where  $Q$  is the time integral of the current pulse. With a continued exposure the input to the pulse processing system is a series of transient current pulses while the output is either a count rate or an energy spectrum. The basic component in a typical signal processing chain are shown in fig. 4.6.

The radiation interacts with the detector depositing energy that is converted into a current pulse. The total charge is usually too small to be sensed directly, in fact the current is sent to a **preamplifier** that produces a voltage step  $\Delta V$  proportional to  $Q$ . Then the shaping amplifier converts the preamplifier output signal into a form suitable for measurements producing an output voltage pulse with pulse height  $V_{peak}$  proportional to  $Q$ . The output of the shaping amplifier should return rapidly to zero (or baseline) to prevent pulses from overlapping and a resulting distortion of measurements. The amplifier is characterized by a time shaping constant that should be as small as possible to minimize overlap or pulse pile-up. After the shaped pulse is sent to circuits that select pulses for further processing, selecting only certain type of signals. There are two types of discriminator: integral discriminator and differential discriminator. The first one selects all pulses with pulse height (therefore energy) above a certain Low Level

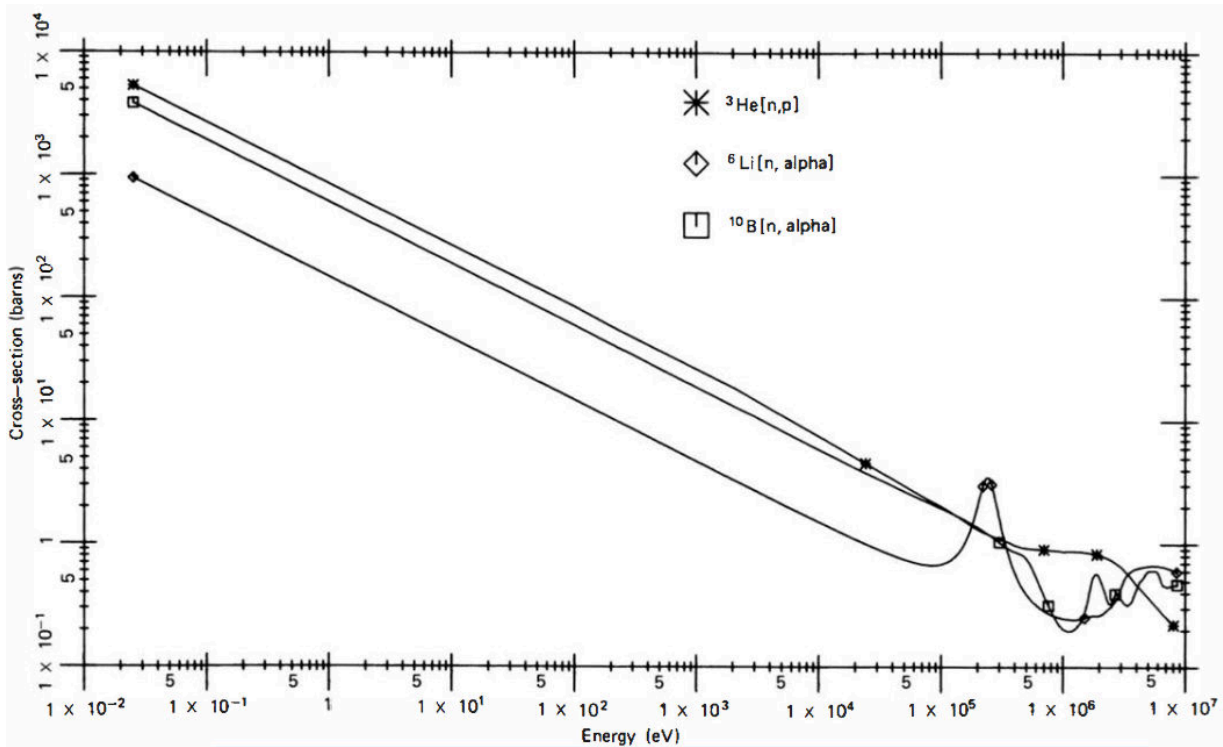


FIGURE 4.5: Cross section versus neutron energy for some reactions of interest in neutron detection, ref. [20].

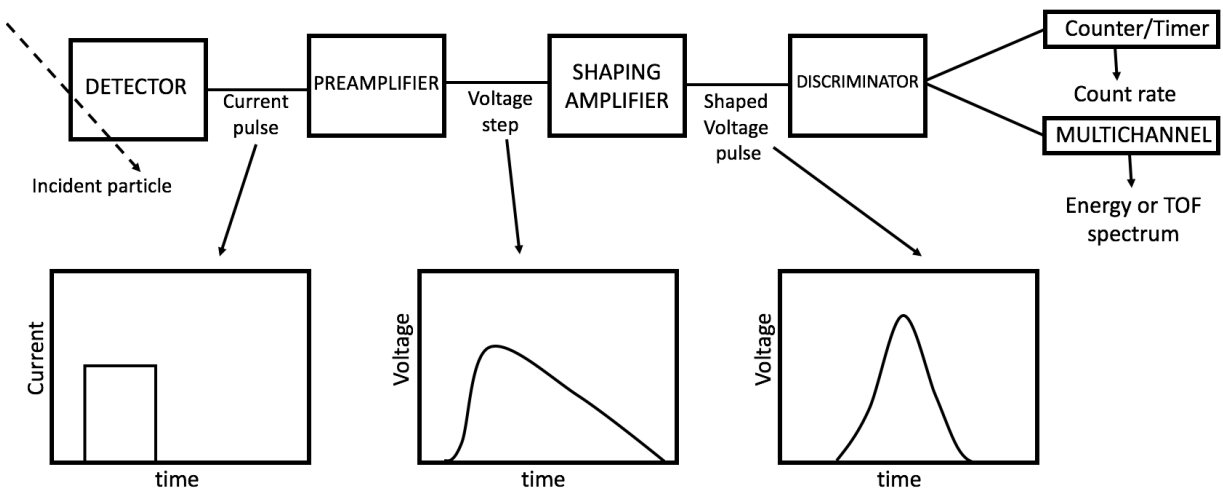


FIGURE 4.6: Scheme of acquisition chain.

Discrimination (LLD) threshold. The second one selects pulses with peak amplitude between a LLD and a Upper Level Discrimination threshold (ULD). The integral discriminator is used for our YAP detectors at VESUVIO, and consists of a device that produces a logic output pulse only if the input pulse amplitude exceeds a set discrimination level. The discrimination level is normally set just above the system noise and is used, as in our case, to enhance the signal-background ratio because the background may be limited to relatively low pulse amplitudes. As a final step the signal is processed in a counting system, multichannel in our case, that accumulates the logic pulses recorded during the time of measurements.

The interrelationship between the various signal pulses at the different steps in the acquisition chain is shown in fig. 4.7

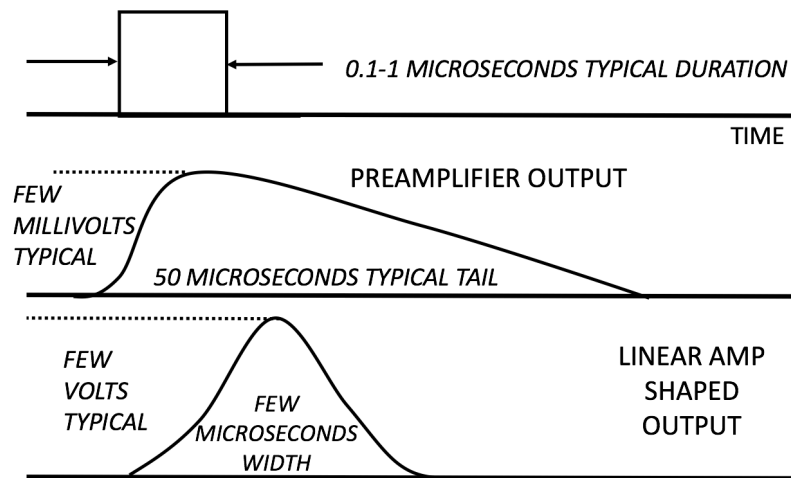


FIGURE 4.7: Comparison of the pulses at different points of the acquisition chain.

## 4.2 Resonance-Filter

The Resonance Filter (RF) spectrometer is an inverse geometry instrument that performs the scattered neutrons energy analysis using nuclear resonances. The neutron absorption cross sections of isotopes such as  $^{238}\text{U}$ ,  $^{197}\text{Au}$  are characterised by the presence of intense and narrow resonances of radiative neutron capture in the electron Volt energy region. Figures 4.8 and 4.9 show the absorption cross section of two isotopes, namely  $^{197}\text{Au}$  and  $^{238}\text{U}$ , which are commonly used as energy filters.

The principle of the measurement in such configuration is very simple. The physical signal is provided by the difference between two measurements: the first with the analyser filter inserted in the scattered neutron beam (the so-called foil-in measurement), the second with the foil removed (foil-out measurement). This procedure is known as the Filter Difference (FD) method. In fig. 4.10 it is shown a scheme of the FD method and a typical TOF spectrum acquired before the difference.

The neutron counting is provided by an array of  $^6\text{Li}$ -glass scintillation detectors which respond to all energies with an efficiency depending on  $\frac{1}{v}$  being  $v$  the neutron velocity. The energy analyser can be described as a pass-band filter as it selects neutron energy within a region corresponding, at a first approximation, with the total width of one of the resonances. The overall response of the spectrometer can be described as a convolution of the filter transmission function with the one describing the geometrical contribution to the total instrument resolution. The instrument resolution is a Gaussian convolution of geometrical error contributes as the one of the solid angle. The transmission function of the single nucleus resonance can be described,

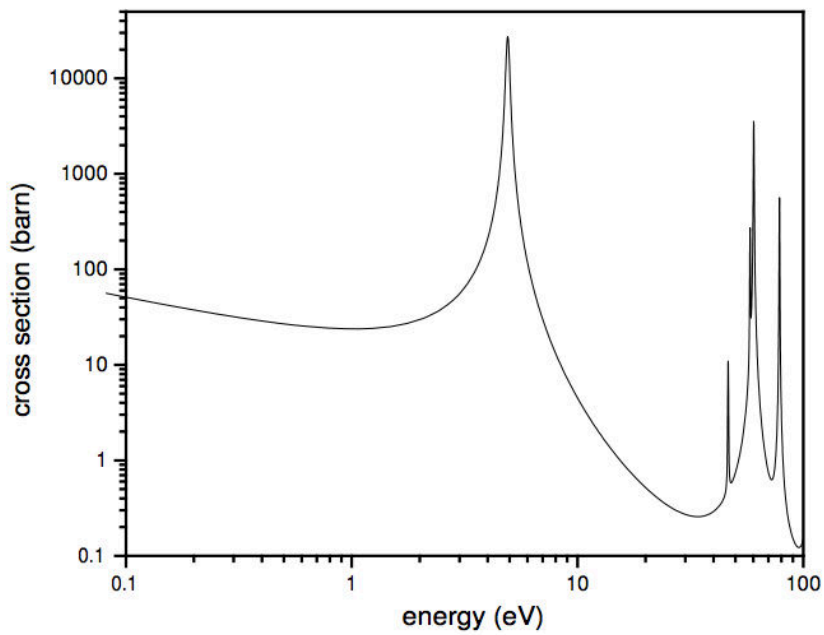


FIGURE 4.8: Neutron absorption cross section of  $^{197}\text{Au}$  in the energy range 0.1 - 100 eV, ref. [21]

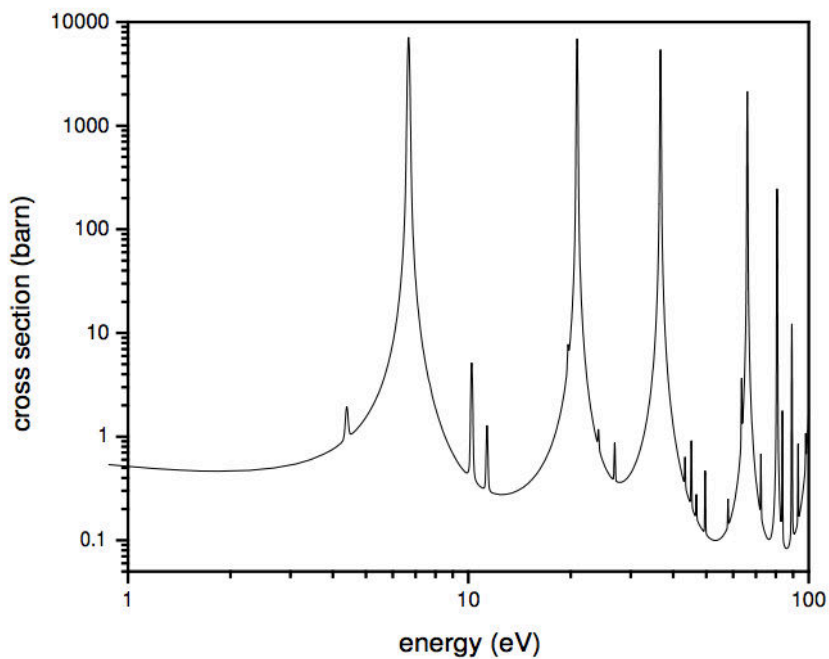


FIGURE 4.9: Neutron absorption cross section of  $^{238}\text{U}$  in the energy range 1 - 100 eV, ref. [21]

with good degree of accuracy, by a Lorentzian function (Breit-Wigner resonance function):

$$\Gamma(E) = \frac{1}{\pi} \frac{\Gamma_r}{\Gamma_r^2 + (E - E_r)^2} \quad (4.5)$$

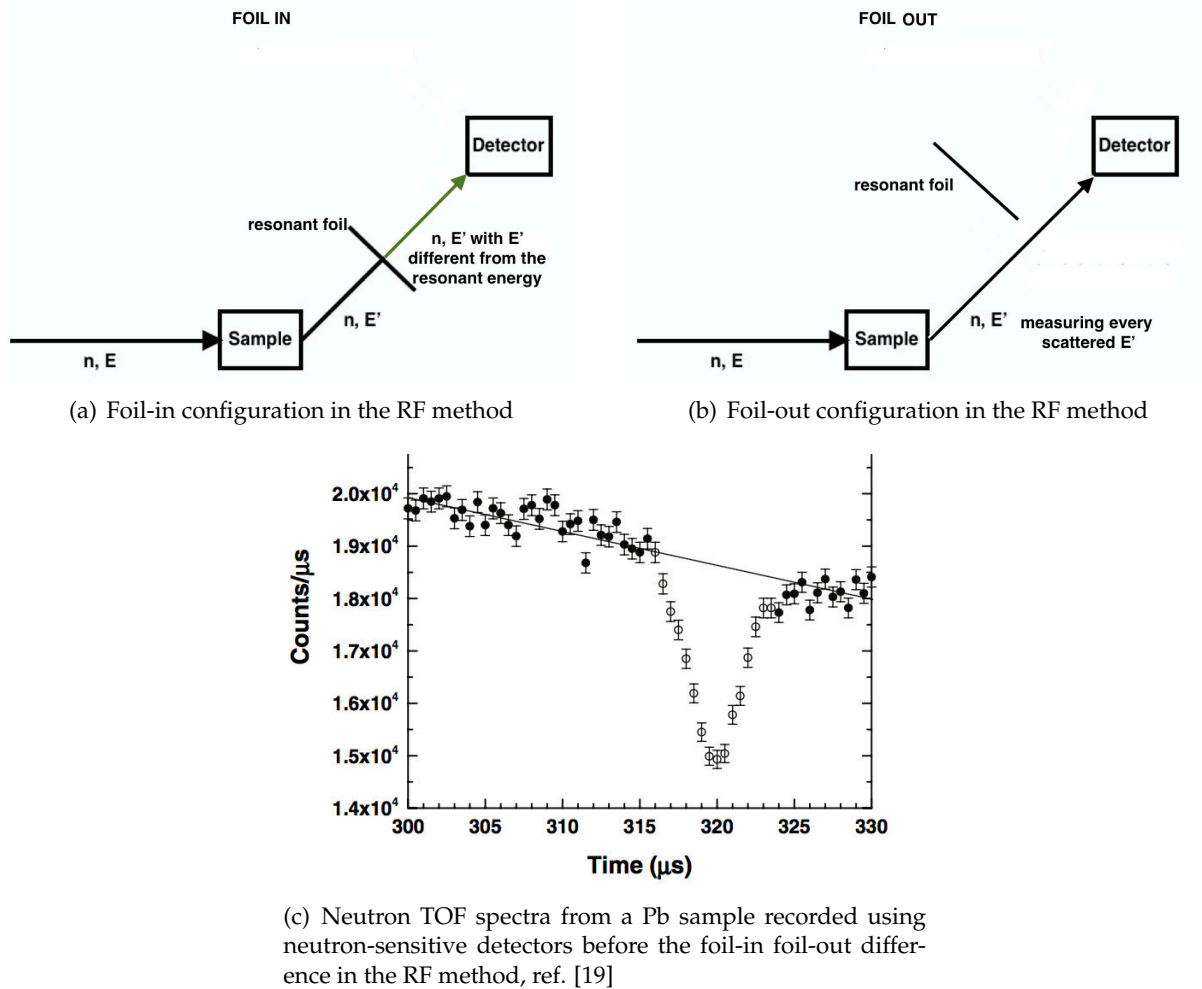


FIGURE 4.10

$E_r$  being the resonance energy ( $E_f = E_r$ ) and  $\Gamma_r$ , independent of  $E$ , the half width at half maximum (HWHM). This expression is assumed to represent the free-nucleus nuclear absorption profile. The latter is broadened due to the thermal motion of the nuclei bound in the lattice, so that the overall lineshape is given by the convolution of the function 4.5 with a Gaussian function, representing the Doppler broadening, providing an overall Voigt profile. So what we see from our result is not only the atom momentum distribution but the convolution with this response function of the spectrometer. Anyway this contribution can be lowered by cooling the filter and/or employing the Double Difference Method (DDM) (see ref. [22]). In the DDM two filters of different thickness,  $t_1$  and  $t_2$  are employed. In this case the scattered signal is obtained using a weighted difference of signals coming from Au foils of distinct thickness. This method achieves a finer experimental resolution than the Single Difference by removing the Lorentzian wings coming from the resonant foil. This DDM is used in the backward direction of the detection system where there is a rotating device (filter chamber), allocating Au analyser filters of different thickness, and by a fixed aluminium hexagonal frame where  $^6\text{Li}$ -glass detectors are placed at an average distance of about 80 cm from the sample position.

As a matter of fact the main limitation of the VESUVIO spectrometer configured in the RF set up, is the decreasing counting efficiency of the  $^6\text{Li}$ -glass detectors with increasing neutron velocity. At high neutron energies (above 10-15 eV) the detection efficiency loss of these neutron counters and their neutron and  $\gamma$  background sensitivity becomes the main limiting factor for their effective employment in scattering measurements. For this reason a different technique, Resonance Detection, for forward direction is employed.

### 4.3 Resonance-Detector

The Resonance Detector (RD) spectrometer is an inverse geometry instrument employing nuclear resonances to select final neutron energy used in the VESUVIO forward scattering. The neutron counting is not provided by standard neutron counters, as it applies in the RF, but by photon detectors which reveal the prompt  $\gamma$  - ray cascade produced, via  $(n, \gamma)$  reactions, by scattered neutron absorption by an analyser foil. The RDS counting procedure relies upon two main steps: in the first step, the scattered neutron beam impinges onto the analyser foil which provides the energy analysis by means of  $(n, \gamma)$  resonant absorption at a given resonance energy  $E_r$ . In the second step, the prompt gamma rays are detected and provide the total TOF of the absorbed neutron. It has to be emphasized that the gamma detector is used as a counter: simply provides a trigger to the counting electronics if the signal is above a discrimination threshold that can be set electronically, in this way they work under a Low Level Discrimination (LLD) threshold. The analyser foil has to fulfil some important requirements:

- the radiative capture cross section has to show isolated and intense resonances in the energy region of interest
- these resonances should have small widths
- the emitted  $\gamma$  - ray spectrum should contain lines with appreciable relative intensities

The first two requirements are important in order to properly select the scattered neutron energy and to ensure a low contribution to the energy component of the resolution function of the spectrometer, respectively. The third requirement allows for selecting gamma rays that provide the best signal to background (S/B) ratio. In table 4.3, a number of suitable isotopes that can be used in the RDS configuration are listed together with their main physical parameters.

The gamma emission lines of  $^{197}\text{Au}$  and  $^{238}\text{U}$ , the two most widely used isotopes, are shown in figure 4.11.

The choice of the preferred isotope for the analyser foil depends on the neutron scattering experiment that is performed. The preferred isotope depends for example on the momentum transfer that is assessed, the energy resolution that is required and the data collection time that is allocated for the experiment. The width of the  $^{238}\text{U}$  resonances are narrower than the  $^{197}\text{Au}$  resonance, giving a better energy resolution, but this narrower width results in less neutrons being absorbed in the analyser foil. For relatively short allocated data collection times, the limited counting statistics with a  $^{238}\text{U}$  foil might give less accurate lineshape functions than with a  $^{197}\text{Au}$  analyser foil. Furthermore the numerous and close peaks in the  $^{238}\text{U}$  radiative neutron

Isotope	$E_r$ (eV)	$\sigma_0$ (b)	$\Gamma_\gamma$ (meV)
$^{113}\text{In}_{49}$	14.6	9965	67
$^{139}\text{La}_{57}$	72.2	5969	96
$^{150}\text{Sm}_{62}$	20.7	56207	109
$^{160}\text{Dy}_{66}$	20.5	16165	124
$^{168}\text{Er}_{68}$	79.7	11203	121
$^{178}\text{Hf}_{72}$	72.6	16830	112
$^{182}\text{W}_{74}$	21.1	46800	104
$^{190}\text{Os}_{76}$	91.0	6777	105
$^{197}\text{La}_{79}$	4.96	36592	60
$^{238}\text{U}_{92}$	6.67	23564	25
$^{238}\text{U}_{92}$	20.8	37966	34
$^{238}\text{U}_{92}$	36.6	42228	57
$^{238}\text{U}_{92}$	66	20134	48

TABLE 4.3: List of physical properties for suitable isotopes in RDS

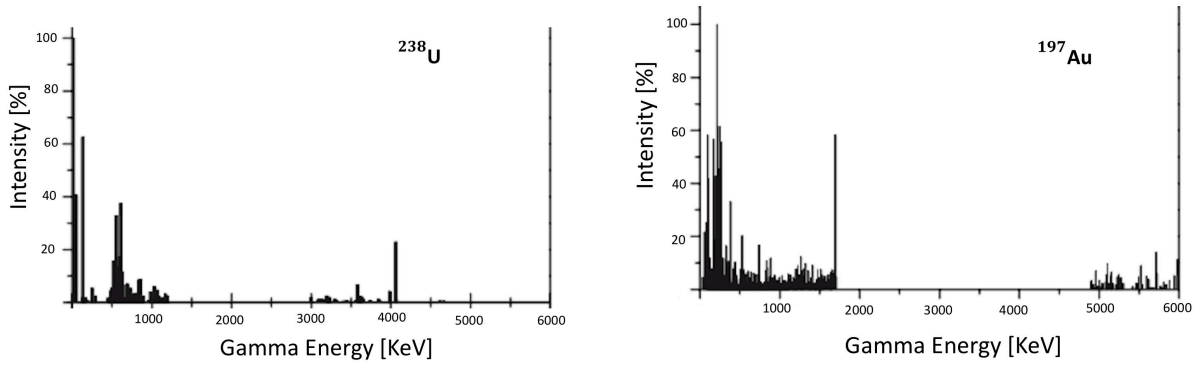
(a) Gamma emission lines of  $^{197}\text{Au}$  from  $(n, \gamma)$  reaction, ref. [21](b) Gamma emission lines  $^{238}\text{U}$  from  $(n, \gamma)$  reaction, ref. [21]

FIGURE 4.11

capture absorption shown in fig. 4.9 could give superposition effects in the TOF spectra that are not present for the  $^{197}\text{Au}$  case (see fig. 4.8). For these reasons now at VESUVIO  $^{197}\text{Au}$  analyser foils are used. In fig. 4.12 the acquisition set-up for the RD configuration is showed; the RD counting procedure relies upon two main steps. In the first step the scattered neutron beam impinges onto the analyser foil which provides energy analysis by means of resonant absorption. In fact a neutron having an energy within the width of the resonance is strongly absorbed while an off-resonance neutron interacts with less probability. In the second step the prompt  $\gamma$  are detected to assign the total neutron TOF. The  $\gamma$  detection produces a voltage signal which is processed by a fast electronic chain, providing the stop signal for the acquisition electronics. Once the detector, the foil area and their relative distance have been chosen, the total detection efficiency depends on the  $(n, \gamma)$  cross section, the  $\gamma$  detection efficiency and on the probability of  $\gamma$  self-absorption in the analyser.

In figure 4.13 is shown a scheme of simple RD configuration and a typical TOF spectrum acquired before the background subtraction.

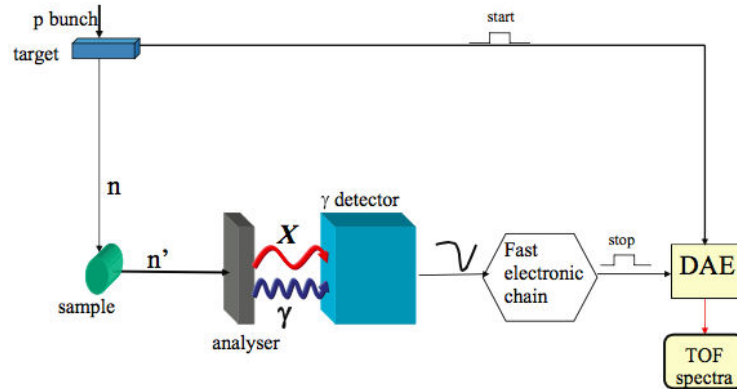


FIGURE 4.12: Schematic drawing representing the experimental set-up of a resonance detector spectrometer, ref. [19].

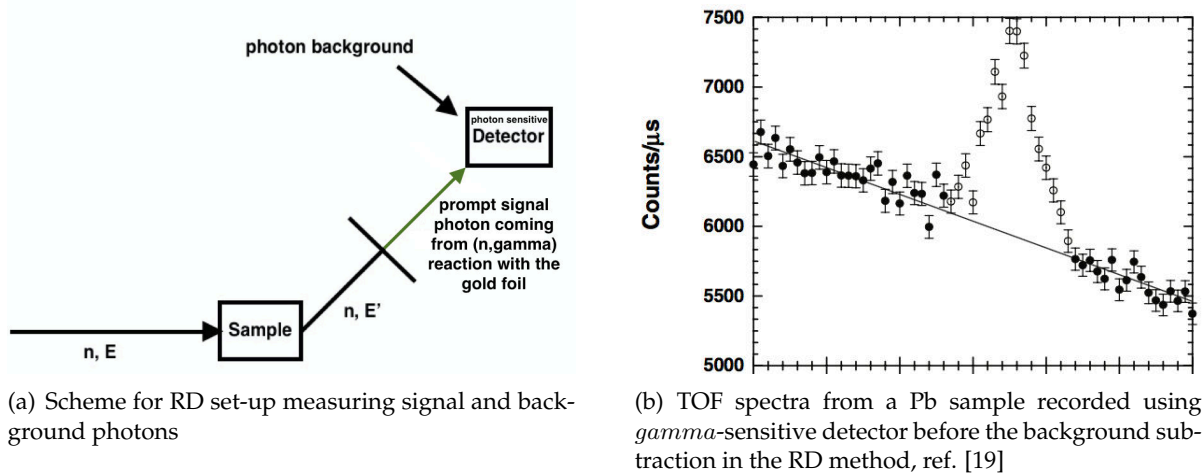


FIGURE 4.13

For resonance radiative capture detectors to be competitive in instruments that operate continuous user-programmes, a couple of issues have to be addressed: energy resolution improvement and gamma background reduction. Indeed, an epithermal neutron spectrometer utilizing neutron detectors provides a slightly better resolution than that achievable with a resonant detector spectrometer (RDS) operating in the set-up shown in figure 4.12. Both the energy resolution and gamma background drawbacks of RDS can be effectively solved by using the foil cycling technique. The foil cycling technique (FCT) provides the possibility to enhance the overall resolution of the spectrometer and obtain a good subtraction of the gamma background. This allows a more reliable lineshape analysis of the recoil peaks. FCT introduces an additional foil, between the sample and detector, that can be cycled in and out of the flight path of the neutrons, see figure 4.14.

The final signal is obtained by subtracting the signal recorded in the foil-out position with the signal recorded in the foil-in position. In fact for the foil-out configuration the photons detected are background photons from the environment (interaction between neutrons and the block-house) and signal photons from the gold foil (radiative neutron capture); in the foil-in configuration the photons detected are in the same number for the background but are less for

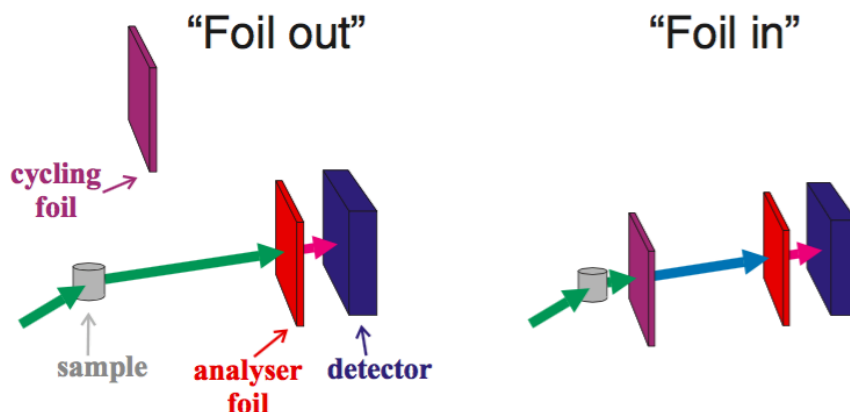


FIGURE 4.14: Schematic representation of the set-up used in the foil cycling technique, ref. [19].

signal. In fact the second gold foil reduces neutrons that impinge on the gold analyser in front of the detector, in this way we obtain a less intense peak characterised by the Lorentzian tails of the resonance that were present also in the foil-out measurement. Making the difference between this two spectra we get an isolation of signal photons with a good energy resolution. The signal isolation obtained with the FCT is shown in fig. 4.15 for a polyethylene sample, where the black spectrum is acquired in foil-out configuration, the red one in foil-in configuration and finally the green spectrum is the difference between foil-in and foil-out, it is shifted by a value of 1000 counts per microseconds to represent all the spectra in the same figure.

Another source of background is the  $\gamma$  "delayed" emission from the activated gold atoms of the foils which are  $\beta^-$  unstable. In fact after the  $\beta^-$  emission the atoms could be in an excited state and emit photons randomly in time giving only a rigid shift to the spectra which is subtracted with the cycling method.

In fig. 4.16 there is a scheme of the foil cycling technique where we can see two types of gold foils: fixed in front of the  $\gamma$  - sensitive detectors and moving on a cylindrical slide.

RDS does not require the use of gamma detectors with a good energy resolution. Scintillator detectors are therefore attractive because of their high density and relatively low cost per unit area. The detectors are used as counters and do not require a significant amount of gamma to be absorbed by the photoelectric effect, allowing the use of scintillators with a relatively low atomic number ( $Z$ ). YAP(Ce) is therefore an attractive scintillator material because it has no neutron absorption resonances in the energy range of interest for RDS and has favourable scintillation properties. The result obtained using YAP instead of  $^6\text{Li}$ -glass is showed in fig. 4.17 using the previous  $^{238}\text{U}$  analyser foils. The YAP detector is clearly superior as far as the S/B ratio is concerned.

To further optimise the S/B ratio of the YAP detection system with  $^{238}\text{U}$  foils, a bi-parametric acquisition (see appendix B) system was setup during DINS experiment. These measurements, performed in a realistic setup for the RDS configuration, allowed to determine the best operating conditions for DINS measurements on VESUVIO. A thorough characterization of the background radiation present at the spectrometer was undertaken to facilitate the analysis of

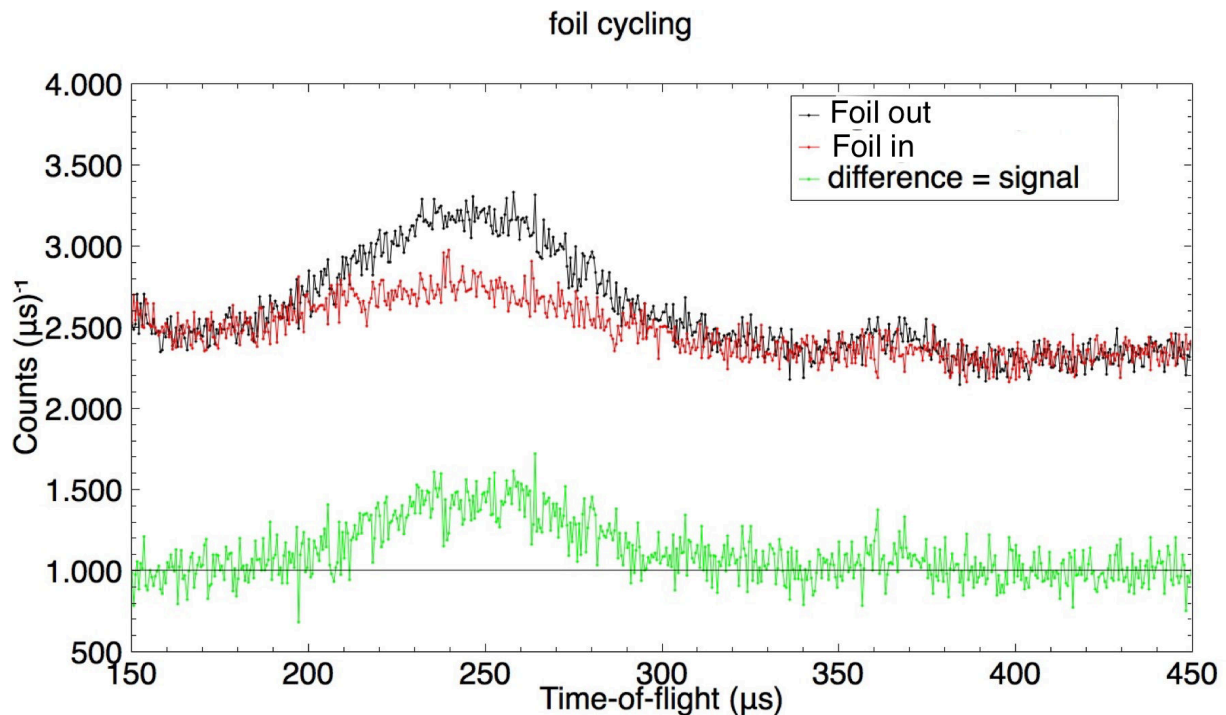


FIGURE 4.15: Measurement of a polyethylene sample using FCT with gold foils and YAP(Ce) detectors. The black spectrum is acquired in foil-out configuration, the red one in foil-in configuration and the green spectrum is the difference between foil-in and foil-out shifted by a value of 1000.

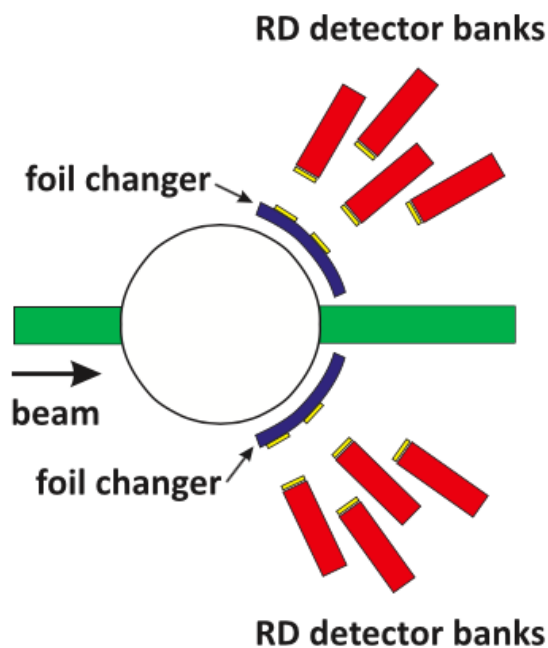


FIGURE 4.16: Scheme of the RD configuration on VESUVIO, ref. [19]

the bi-parametric data. It was found that using a discrimination threshold above 600 keV, it was possible to maximise the S/B and count rate, ref. [23]. This can be explained by the suppression of the 480 keV gammas coming from neutron capture on Boron that is used as absorbing material in the walls surrounding the spectrometer as well as in the beam dump . From 2007

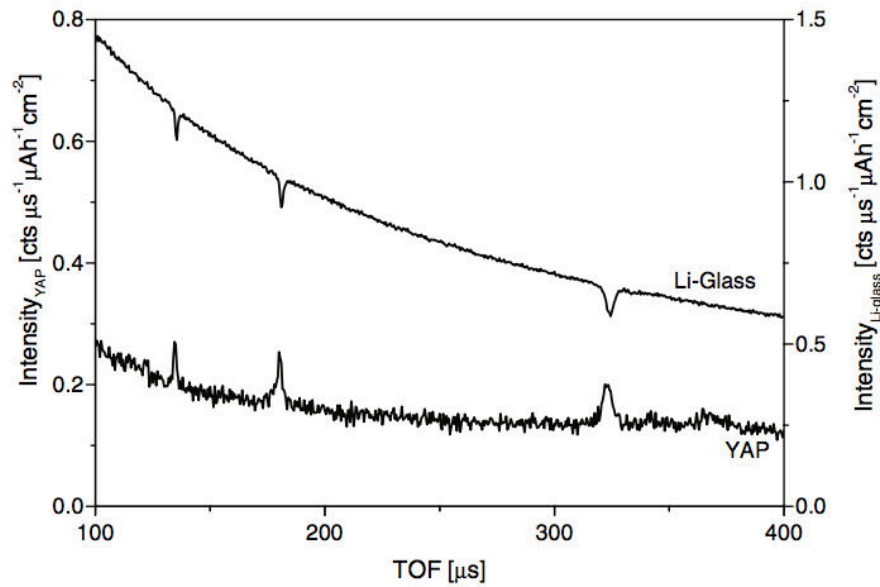


FIGURE 4.17: DINS spectra from a Pb sample and  $^{238}\text{U}$  analyser foils recorded with a  $^6\text{Li}$ -glass and YAP detectors placed at the same scattering angle, ref. [19].

the  $^{238}\text{U}$  analyser foils were substituted by gold foils but no one studied the new best threshold for the new detection system and it was left to 600 keV even if the most intense  $\gamma$  peak after radiative neutron capture are concentrated at energy smaller than 600 keV. This statement is evident from fig. 4.3 but also from recent work such as ref. [24] where a measurement of the  $(n, \gamma)$  gold emission peak are measured at the INES (RAL) beam line. Reference [24] shows that the gold line emission of fig. 4.3 are present but there is another "prompt" gamma contribution which is attributed to the *internal conversion* emission. This emission is due to the de-excitation of  $^{198}\text{Au}^*$  nucleus that produces a gamma ray that doesn't emerge from the atom but interact with an electron that leaves the atom. Now the unstable configuration turns in the stable state emitting a prompt gamma ray at low energy (under 300 keV) characteristic of the electronic configuration. The process is schemed in fig. 4.18.

The aim of this thesis is to demonstrate that lowering the LLD threshold of YAP detectors, using Au analyser foils, we obtain a decreasing effect on the poissonian error bars and in the fluctuation of counts in the TOF and experimental  $J(y)$  spectra which leads to a more precise measurements of the atom momentum distribution and every information coming from that.

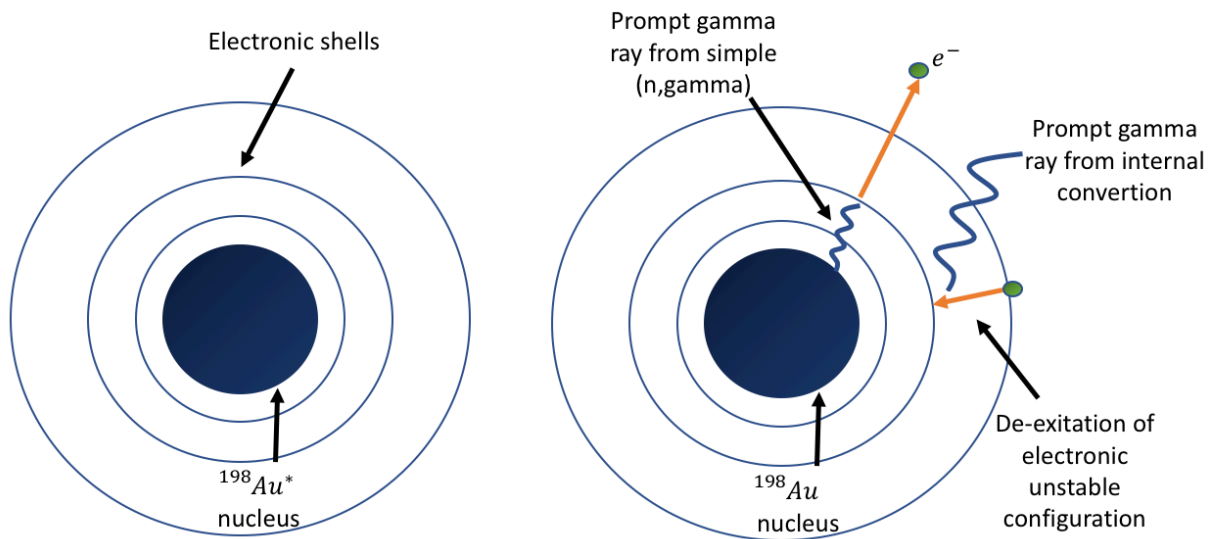


FIGURE 4.18: Scheme of the internal conversion emission.

## Chapter 5

# Measurements and data Analysis

In this chapter I will describe the results obtained from the experiment RB1710136 where we were looking for a possible improvement of the detection procedure on the VESUVIO spectrometer. In this spectrometer several detection methods are employed, including Resonant Filter (RF) and Resonant Detector (RD). In particular since 2007 neutron  ${}^6\text{Li}$  forward sensitive detectors were substituted by photon yttrium-aluminium-perovskite (YAP) sensitive detectors that work in a Low Level Discrimination (LLD) threshold condition where they measure only photons with energy greater than a certain energy value. In this way the signal is given by photons emitted by the resonant foil, through radiative neutron capture, put in front of the detectors. The advantage is the time resolution but, in this configuration, there is a big amount of sample-environment dependent gamma background that is eliminated using difference techniques. The first material used as resonant foils was  ${}^{238}\text{U}$ . For this material the most intense prompt gamma emission peaks from radiative neutron capture are concentrated at high energies (4060 keV and 6395 keV, see ref. [25]). In order to discard the photon background from the Boron peak at  $\sim 500$  keV the threshold chosen was 600 keV. After, the resonant foils were changed using gold instead of uranium; in fact uranium has many peaks in the radiative neutron capture cross section for neutrons with energy very close giving rise to overlap signal problems, while gold has one main big resonance  $\sim 4.9$  eV. Our intention is to find a new threshold for this gold RD configuration.

In this context our experiment is for many respects a proof of concept that shows a decreasing effect on the statistical poissonian error bars (seen as the oscillation of counts around a certain value) and noise after the variation of YAP LLD threshold. Such improvement is obtained at the expenses of a little increase of the S/B ratio that becomes, anyway, irrelevant after the foil cycling subtraction method. This improvement is supported by the  $\gamma$  energy distribution emission spectra of gold for radiative neutron capture. As we can see from figure 5.1 and 5.2 the most intense lines (underlined or in bold in the table, fig. 5.1, and indicated with an arrow in the bi-parametric map, fig. 5.2) are characterized by energy lower than 600 keV and other are available at very low energy from the prompt (emission time  $t < 10^{-9}$  s) internal conversion that is proportional to the atomic number. As each gold peak represents a portion of signal, if we measure only photons with energy greater than 600 keV we are cutting off a great part of good low energy signal. Our intention is to prove it. The best situation would be if we were able to select only the energy windows where the photons of the gold ( $n, \gamma$ ) resonance are present. It would be possible to do this using a bi-parametric acquisition (see appendix A) but, because

of a saturation of the bi-parametric chain of the germanium detector at low time of flight, it was possible only to lower the LLD threshold of the standard YAP detectors installed at VESUVIO using a simple TOF acquisition. The optimization obtained in the acquired spectra is described in the following sections.

79: Gold  $A_r = 196.96655(2)$  u  $\alpha_c = 98.65(9)$  b 100 of 737  $\gamma$   $k_0(\text{H}) = 0.01539(3)$   $\alpha_r$   $k_0(\text{Cl}) = 0.02843(18)$   $\alpha_r$   $k_0(\text{Au}) = 0.010610(12)$   $\alpha_r$   
<sup>197</sup>Au: 98.65(9) b

A	$E_\gamma(\text{keV})$	$\sigma_\gamma(\text{b})$	A	$E_\gamma(\text{keV})$	$\sigma_\gamma(\text{b})$	A	$E_\gamma(\text{keV})$	$\sigma_\gamma(\text{b})$	A	$E_\gamma(\text{keV})$	$\sigma_\gamma(\text{b})$
197	35.8240(10)	0.41(5)	197	219.4190(20)	0.42(4)	197	529.1650(20)	1.9(10)	197	1111.461(7)	0.37(6)
197	55.1810(10)	2.90(12)	197	<b>236.0450(10)</b>	<b>4.1(5)</b>	197	529.954(4)	0.39(5)	197	1239.572(5)	0.49(8)
197	66.3950(10)	0.42(12)	197	<b>247.5730(10)</b>	<b>5.56(8)</b>	197	540.3010(20)	0.49(23)	197	1281.377(7)	0.49(12)
197	75.171(6)	0.390(23)	197	260.8820(10)	0.83(13)	197	544.008(5)	0.52(5)	197	1283.442(7)	0.35(11)
197	82.3560(10)	2.3(4)	197	<b>261.4040(10)</b>	<b>5.3(20)</b>	197	548.9350(20)	0.67(9)	197	1297.124(6)	0.43(10)
197	82.5240(10)	1.4(3)	197	271.8940(10)	0.40(13)	197	565.784(5)	0.38(5)	197	1306.851(5)	0.70(9)
197	<b>97.2500(20)</b>	<b>2.1(5)</b>	197	291.7240(20)	1.05(17)	197	565.810(3)	0.43(6)	197	4957.83(10)	0.63(11)
197	101.9390(10)	0.953(17)	197	307.7180(10)	0.44(6)	197	571.683(3)	0.50(7)	197	5088.46(10)	0.50(8)
197	122.6520(10)	0.81(13)	197	311.9040(20)	0.47(6)	197	574.381(3)	0.36(5)	197	5102.85(10)	0.87(13)
197	123.7860(10)	0.83(13)	197	328.4840(20)	1.48(19)	197	579.297(3)	0.53(8)	197	5140.74(10)	0.395(18)
197	145.1540(10)	0.46(13)	197	346.9050(20)	0.44(11)	197	625.4280(20)	0.44(4)	197	5148.90(10)	0.46(8)
197	146.3460(20)	0.43(4)	197	350.8280(10)	1.0(5)	197	640.669(3)	0.59(5)	197	5225.49(10)	0.42(9)
197	154.7940(20) <sup>+</sup>	0.38(6)	197	371.0790(20)	0.44(6)	197	672.6550(10)	0.55(7)	197	5246.72(10)	0.51(20)
197	158.4360(10)	1.250(18)	197	381.1990(10)	3.0(4)	197	675.8840(10)	0.793(3) <sup>a</sup>	197	5271.86(10)	0.38(20)
197	158.479(11)	0.67(9)	197	<b>411.8044(11)</b>	<b>95.58(12)<sup>a</sup></b>	197	678.208(10)	0.41(12)	197	5279.44(10)	0.524(20)
197	<b>168.3340(10)</b>	<b>3.60(22)</b>	197	418.8400(20)	0.70(9)	197	690.046(6)	0.388(20)	197	5355.00(10)	0.401(16)
197	170.1030(10)	1.66(22)	197	440.3290(20)	0.9(4)	197	702.474(5)	0.51(7)	197	5493.81(10)	0.42(10)
197	170.3990(20)	0.38(5)	197	441.070(5)	0.7(5)	197	836.432(3)	0.76(3)	197	5524.66(10)	0.80(14)
197	180.8640(10)	0.63(11)	197	444.3910(20)	0.56(7)	197	839.516(5)	0.73(20)	197	5710.52(10)	1.27(17)
197	188.1670(20)	0.63(15)	197	449.5700(20)	0.50(6)	197	868.771(4)	0.364(15)	197	5722.94(10)	0.55(16)
197	<b>192.3920(10)</b>	<b>3.9(18)</b>	197	456.287(4)	0.47(6)	197	902.478(6)	0.38(6)	197	5879.74(10)	0.30(8)
197	192.9440(10)	1.70(22)	197	509.175(4)	0.37(9)	197	933.928(6)	0.47(14)	197	<b>6252.11(6)</b>	<b>4.82(7)</b>
197	204.1580(10)	0.513(10)	197	511.5170(20)	0.68(11)	197	1028.564(6)	0.46(7)	197	6319.27(6)	2.89(6)
197	204.1620(10)	0.59(10)	197	516.0620(10)	0.35(5)	197	1107.562(9)	0.52(10)	197	6457.01(6)	1.89(4)
197	<b>214.9710(10)</b>	<b>9.0(12)</b>	197	525.1340(20)	0.35(4)	197	1109.196(4)	0.49(10)	197	6512.25(6)	1.33(3)

a) <sup>198</sup>Au (2.69517 d, 0.5 % / 12 %)

FIGURE 5.1: Energy peaks of  $\gamma$  ray spectra induced by gold thermal radiative neutron capture from ref. [25].

## 5.1 Materials and methods

Our experiment was performed at the Rutherford Appleton Laboratory, near Oxford using the VESUVIO spectrometer. In this experiment we performed measurements on standard polyethylene sample allowing a reliable comparison of spectra with changed and unchanged LLD threshold. During the experiment we have modified only five YAP detectors settings in forward scattering. Figure 5.3a shows the acquisition electronic bank, for each detector there is a specific card.

In order to modify the acquisition setting, an oscilloscope was used to acquire signals from the electronic card for each of the five detectors as we can see in figure 5.3b.

The IN pin is where the signal go inside the acquisition chain, the OUT pin is used to analyse the signal after the shaping and the amplification, the THR screw is used to change the threshold of the detector using a discriminator and finally the MON pin gives a special *time pick-off* digital signal only when the pulse overcomes the threshold. The latter is used only for monitoring the threshold value. Triggering on the MON signal the oscilloscope begins the measurements only when the pulse is at the threshold level. In this way the oscilloscope displays the pulses that

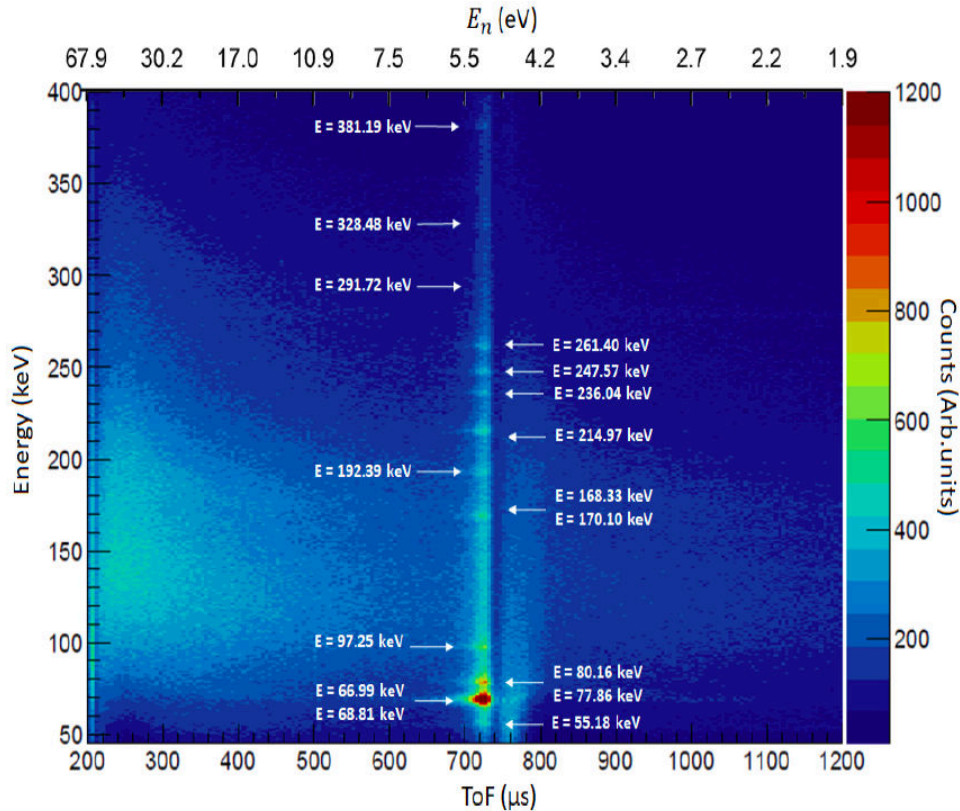


FIGURE 5.2: Intensity contour map of  $\gamma$  emission for radiative neutron capture of the gold foil in a bi-parametric (neutron TOF - photon energy) map (see appendix A), ref. [24].

intersect each other at the value of detector threshold, as that value begins the measurement of the oscilloscope.

Focusing our attention on the intersection point (called A), shown in figure 5.4a, we can study the threshold value and how it changes after our manipulation of the THR pin. For the original configuration that point was around 500 mV. Associating 500 mV to 600 keV (original threshold value), we assumed a linear relation between voltage and threshold energy values.

Using the THR screw we were able to change the detector threshold. The changing was realized through a fine use of a screwdriver, checking at every screw movement the A point signal voltage on the oscilloscope. To obtain a comparison between the measurements, original-changed threshold, we performed two measurements remaining coherent with our set-up.

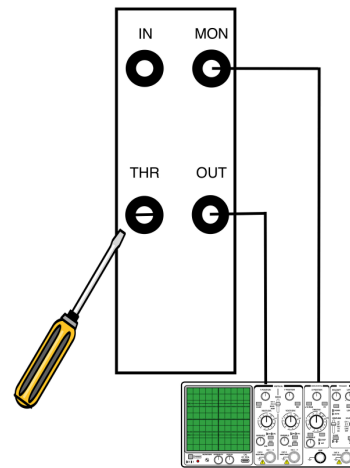
In a first part of the experiment we measured the DINS spectra of a 0.25 mm thick polyethylene sample (the thickness is chosen to avoid multiple neutron scattering) without the introduction of the CCR. Table 5.1 shows the thresholds chosen for detectors 151-155.

First we used that changed set-up and then we repeated the measurement in standard condition to make the comparison.

In a second part of the experiment a preliminary data analysis of the collected data allowed us to find a first best choice for threshold. As a result we turned detectors from 151 to 155 to 120 keV (100 mV). Then we repeated the same procedure of the first part of experiment measuring

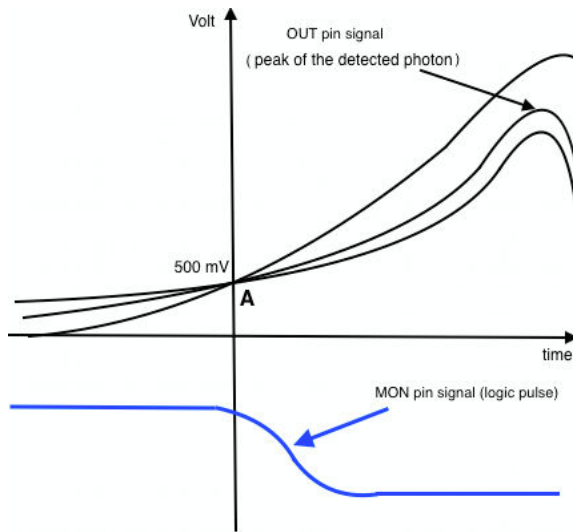


(a) electronics bank

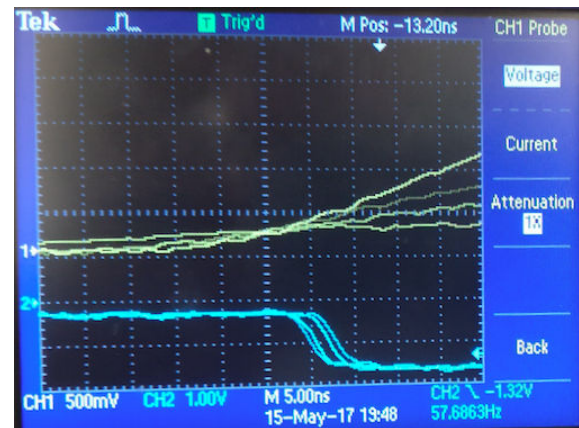


(b) scheme of the acquisition and electronic card

FIGURE 5.3



(a) Scheme of signal measured by the oscilloscope



(b) Experimental measurement with the oscilloscope

FIGURE 5.4: Scheme and experimental measurement acquired with the scope. It is shown the signal of the OUT pin which represent the photons detected and the MON pin which represent the logic pulse emitted when the out signal overcome the threshold.

in the modified set-up and the original one to make the comparison. In Tabular 5.2 there are the VESUVIO runs associated to the measurements.

The raw data was analysed trough MantidPlot, a framework that supports high-performance computing of material science data from neutron scattering experiments. In MantidPlot many

Detector	Threshold (A point)
151	0 keV (0 mV)
152	120 keV (100 mV)
153	240 keV (200 mV)
154	360 keV (300 mV)
155	480 keV (400 mV)

TABLE 5.1: Threshold and A point voltage value of detectors in the first part of experiment

run	experiment
27628 - 27644	first part modified threshold
27660 - 27676	first part original threshold
27681 - 27705	second part modified threshold
27714 - 27738	second part original threshold

TABLE 5.2: Run associated to the different sections of the experiment, each run is associated to 30 min of measurement divided into three foil-in and three foil-out periods.

fundamental functions are implemented; for example a special function *LoadVesuvio* allows the subtraction foil-out and foil-in and the normalization to the proton current useful when we need to compare measurements that last different runs. Every acquisition run of  $\sim 30$  min was acquired in six periods. These periods are characterised by different position of the movable gold foil (three of foil-in and three of foil-out) enabling the difference method.

## 5.2 First measurement without CCR

### 5.2.1 Time of flight spectra

In what concerns the first part of the experiment (without CCR), first we compare the signal spectra of original configuration with the changed one normalising them only to the proton charge and then also to the area of the DINS peak. In figure 5.5 the former type of spectrum is shown. This figure is the most significant, it comes from the detector 151 where there is a big difference between original and changed setting. We can see the recoil peaks of hydrogen (lower TOF) and carbon (higher TOF). It is evident that lowering the threshold there is a counts increment (red spectrum is always over the black one). This increment is very significant in detector 151 and it decreases gradually for the other detectors (see appendix B).

In figure 5.6 is shown the TOF spectrum of detector 151 normalised to the proton charge and to the peak area (for other detector see appendix B). This operation is needed to compare in a simple way the poissonian statistical relative errors associated to the counts (red error bars smaller than black one).

To show in a clearer way the decreasing of the relative error bars it is useful to calculate and show the ratio

$$\frac{\text{Relative error bars of changed threshold}}{\text{Relative error bars of original threshold}} = \frac{\Delta_c}{\Delta_o}$$

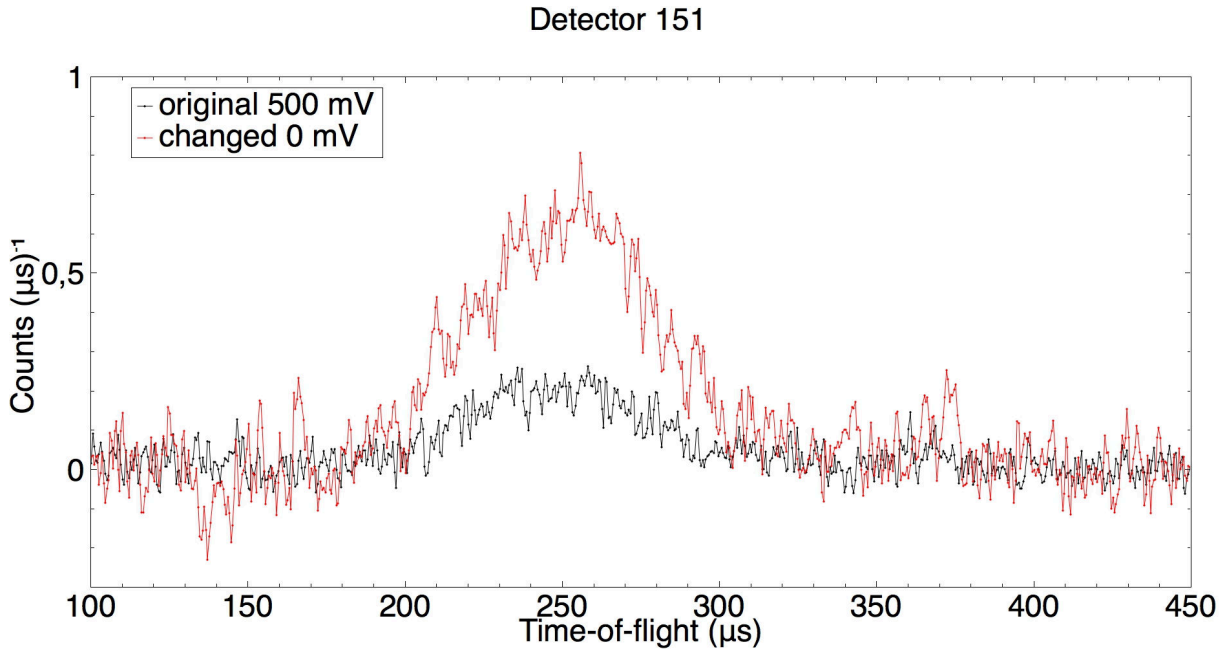


FIGURE 5.5: Comparison of polyethylene spectra, without error bars, between original and changed threshold from detector 151 using a binning of  $0.5 \mu s$  normalized only to the proton charge

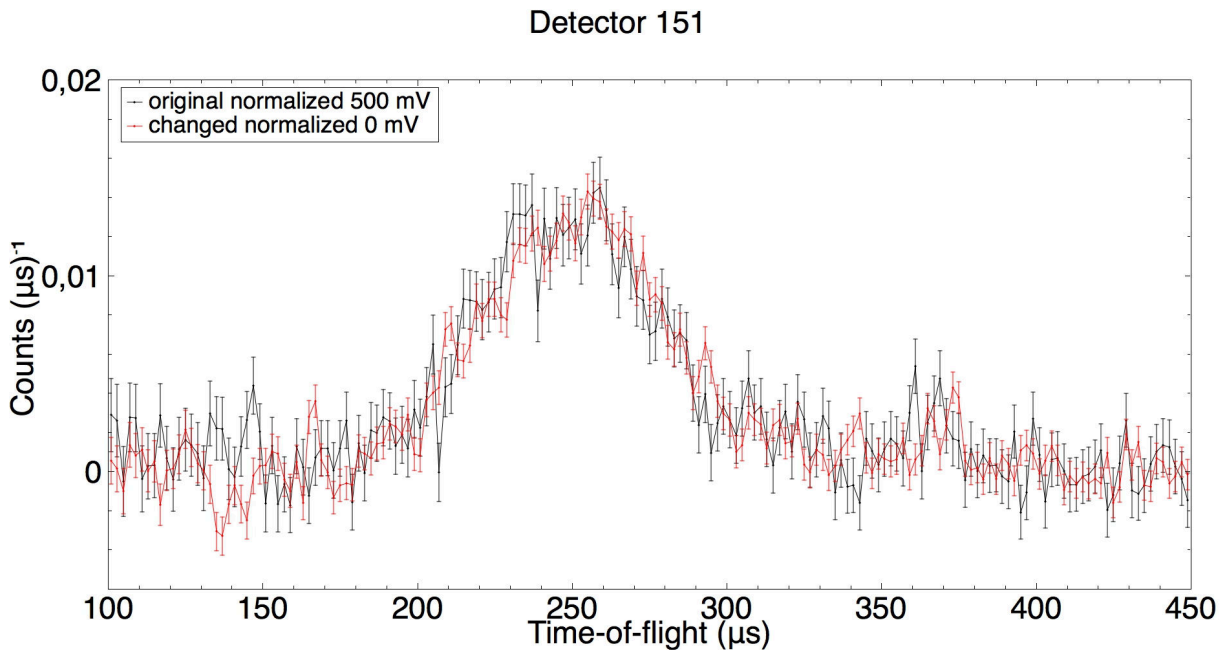


FIGURE 5.6: Comparison of polyethylene spectra, with error bars, between original and changed threshold from detector 151 using a binning of  $2 \mu s$  normalized to the proton charge and to the peak area

This ratio is shown in Figure 5.7

In this figure we can note that the ratio between relative errors is less than one for every detector (from 10 % to 40 %) in almost the TOF range. It seems that detectors 151 would be the best choice (reduction of 40 %) but at this point this statement is hasty because we are not considering the sensitivity of detectors to the changing of threshold i.e. the gain of detector 151 could be due

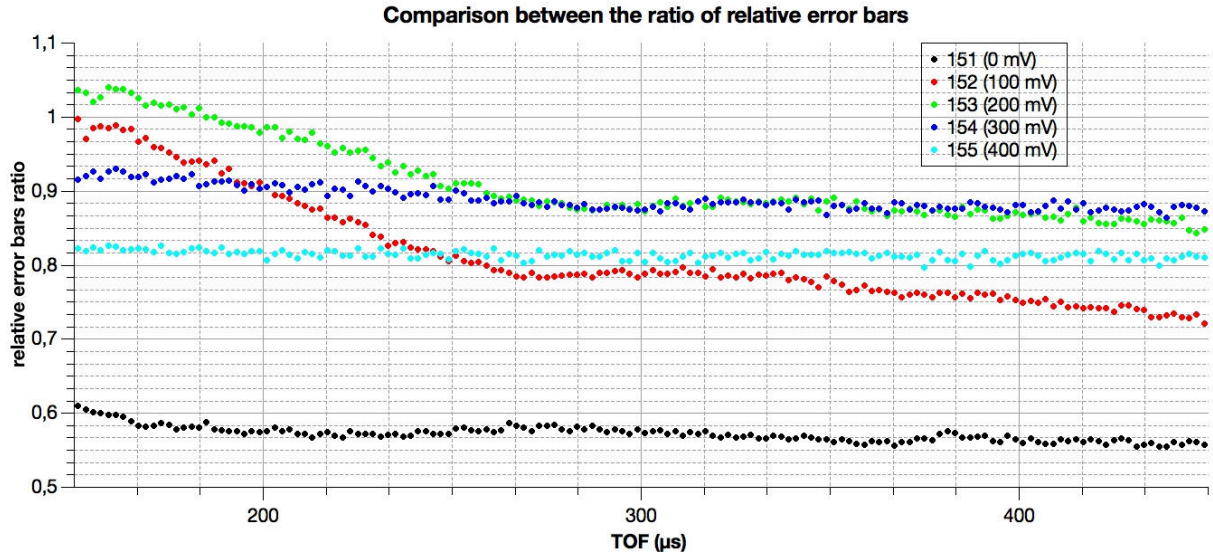


FIGURE 5.7: Comparison between ratio  $\frac{\Delta_c}{\Delta_o}$  of relative error bars from different detectors of polyethylene spectra using a binning of  $2 \mu s$

to a great detector-sensitivity and not at all for the new setting. This sensitivity is due probably to the history of the detector (detectors could be more efficient also in different energy ranges) and this implies a detector-dependence of the ratio  $\frac{\Delta_c}{\Delta_o}$ . On the other hand  $\frac{\Delta_c}{\Delta_o}$  doesn't seem to be peak-dependent (for a fixed detector) because it is almost constant in time of flight (carbon and proton signal independent). This is justified by the fact that we are including the number of signal events in the same way for each peak (lowering the threshold we include the same number of signal gold peak for each recoil peak).

## 5.2.2 $y$ -space spectra

It is important to make sure that this result is reflected also in the Compton profile, in fact we must take into consideration that before going up to the momentum distribution and average kinetic energy. Owing the properties of the  $y$  space we can sum all the spectra from different detectors associated with the same mass, in fact in this space the DINS peaks that are at different time of flight, because they have different  $\mathbf{q}$ , coincides at  $y = 0$ . Figure 5.8 shows the experimental Compton profile of the sum of the hydrogen  $F(y, \mathbf{q})$ <sup>1</sup> coming from detectors 151-155 normalized to the peak area in the original and changed threshold case.

From its relative error bars ratio  $\frac{\Delta_c}{\Delta_o}$  shown in figure 5.9 we can note the decrease of the relative error (from 10 % to 30 %) also in this case.

<sup>1</sup>  $F(y, \mathbf{q})$  is the Compton profile  $J(y, \hat{\mathbf{q}})$  convolved with the resolution function of the spectrometer considering also the final state effects (which give the  $\mathbf{q}$  dependence and not only the  $\hat{\mathbf{q}}$  dependence).  $\bar{F}(y)$  is the sum (average) of  $F(y, \mathbf{q})$  for different detectors

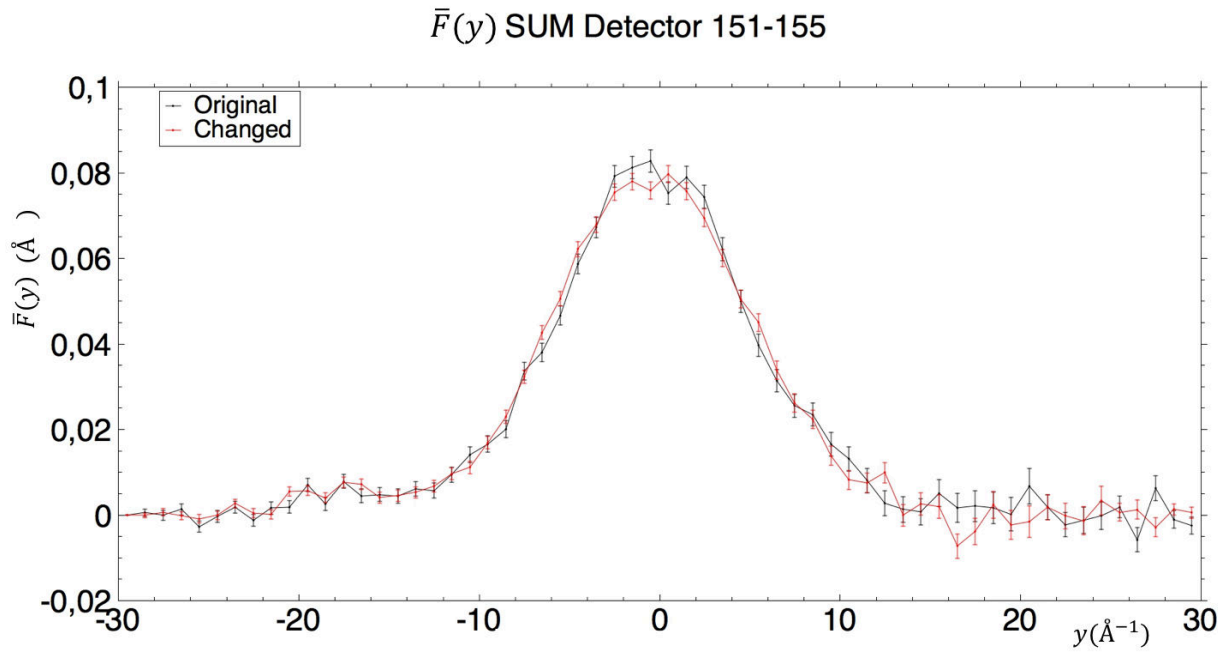


FIGURE 5.8:  $\bar{F}(y)$  spectra with normal and modified threshold summing detectors 151-155 using a binning of  $1 \text{ \AA}^{-1}$

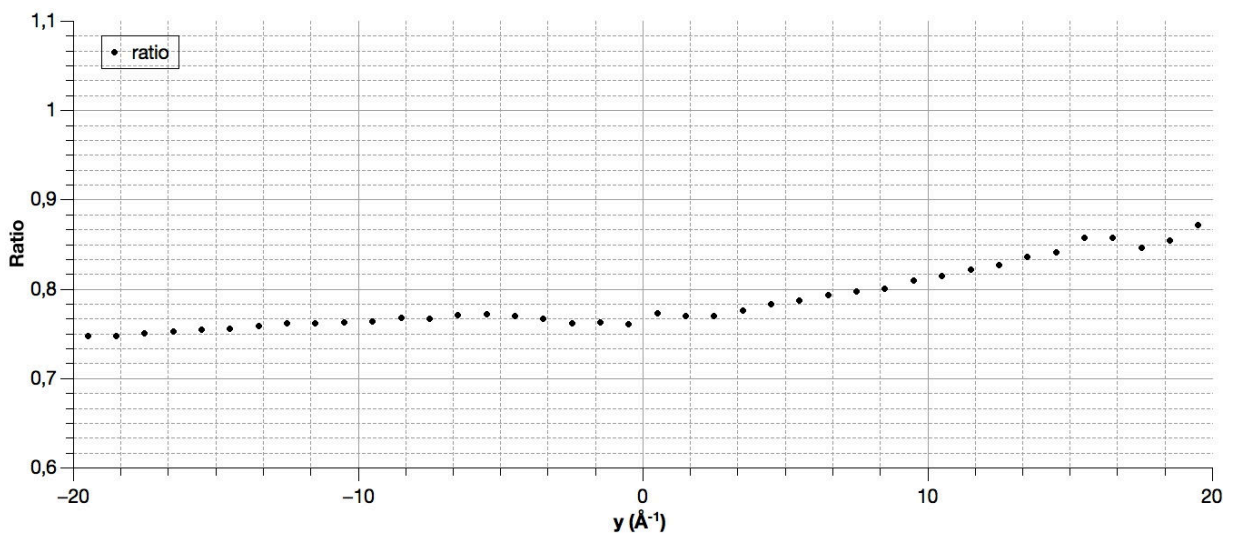


FIGURE 5.9: Ratio  $\frac{\Delta_c}{\Delta_o}$  of polyethylene  $\bar{F}(y)$  (sum 151-155) spectrum using a binning of  $1 \text{ \AA}^{-1}$

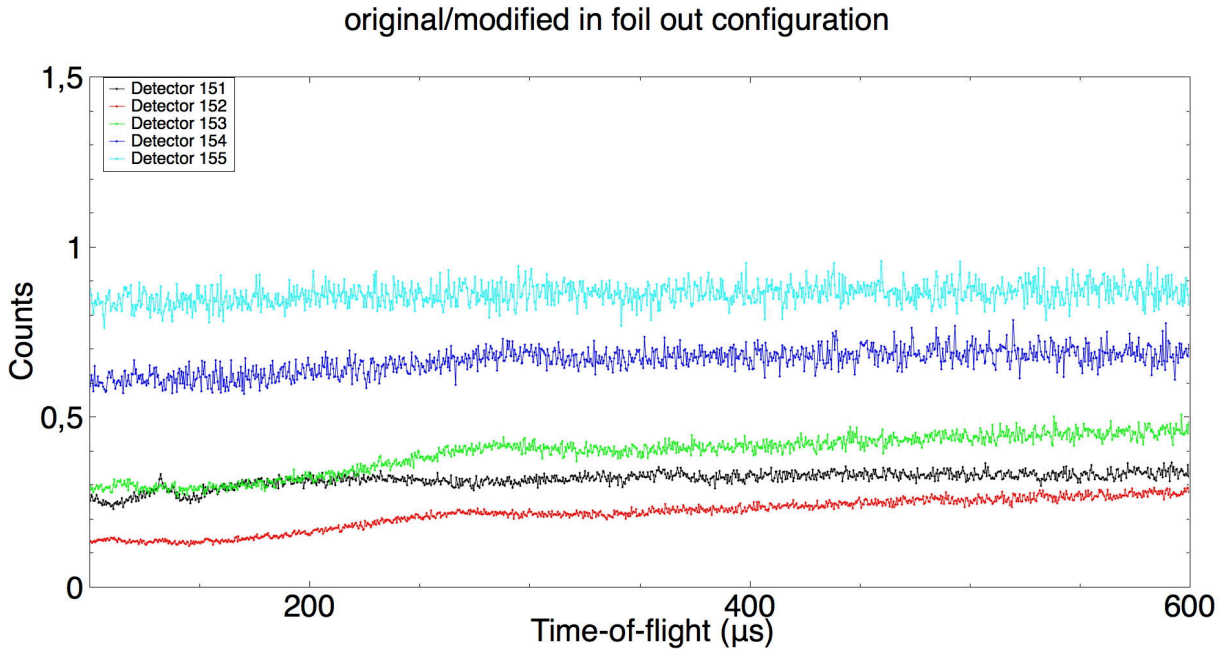


FIGURE 5.10: Ratio between the spectra in original and modified configuration acquired in the foil-out gold position

### 5.2.3 Signal background ratio

Finally we can study what is the percentage of signal in our raw data. In figure 5.10 there is the ratio, in the foil-out configuration, between counts in the original configuration and counts in the changed one; we can see that lowering the threshold we have much more events and they increase (ratio decrease) as the threshold became lower (detector 151-152 respect to 154-155).

In figure 5.11 is shown what is considered as signal and what as background.

In particular the signal (S) comes from the difference foil-out and foil-in while the signal more background (S+B) comes from the foil-out geometry. In order to obtain that values we have integrated the proton (hydrogen) TOF peak (more intense than carbon) in a range of  $80 \mu s$  around the centroid. In table 5.3 there are the integration ranges associated with different detectors (each of them has the TOF peak in a different position).

Detector	Range
151	(215-295) $\mu s$
152	(215-295) $\mu s$
153	(240-320) $\mu s$
154	(250-330) $\mu s$
155	(210-290) $\mu s$

TABLE 5.3: Integration range for different detectors to calculate S and S+B of the proton peak

By calculating the ratio between S and S+B in the original and changed configuration we find the figure 5.12.

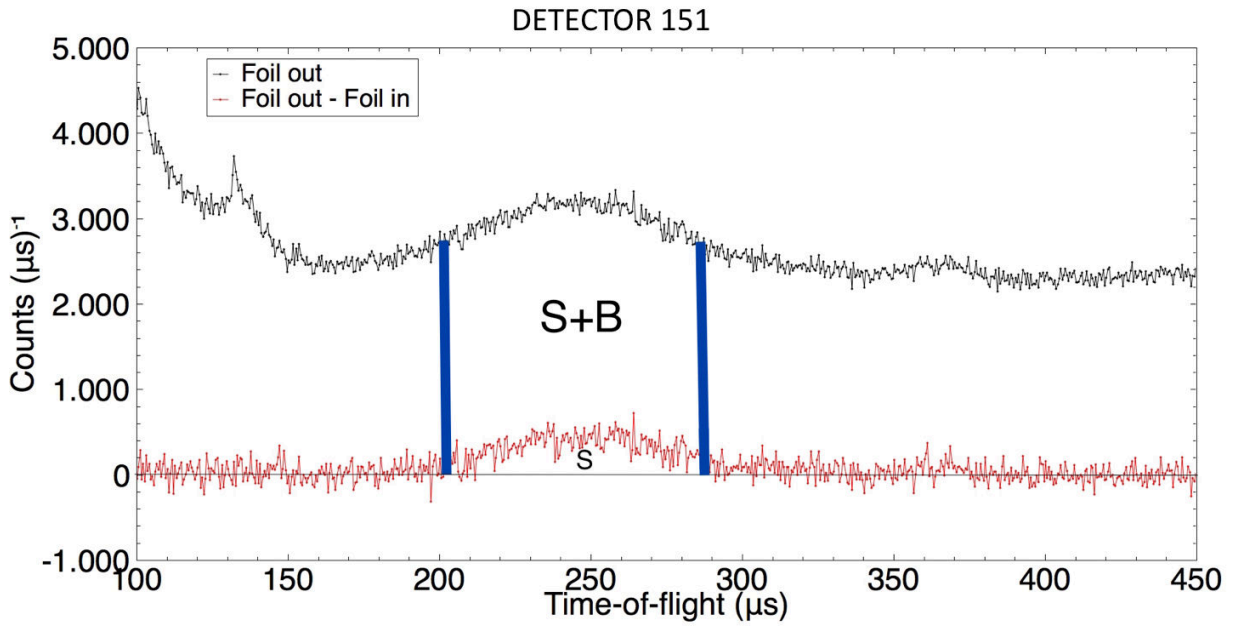


FIGURE 5.11: TOF spectra representing the foil-out measurements and the difference between foil-out and foil-in measurements not normalized.  $S+B$  is the area under the foil-out peak,  $S$  is the area under the difference peak. Binning  $0.5 \mu s$

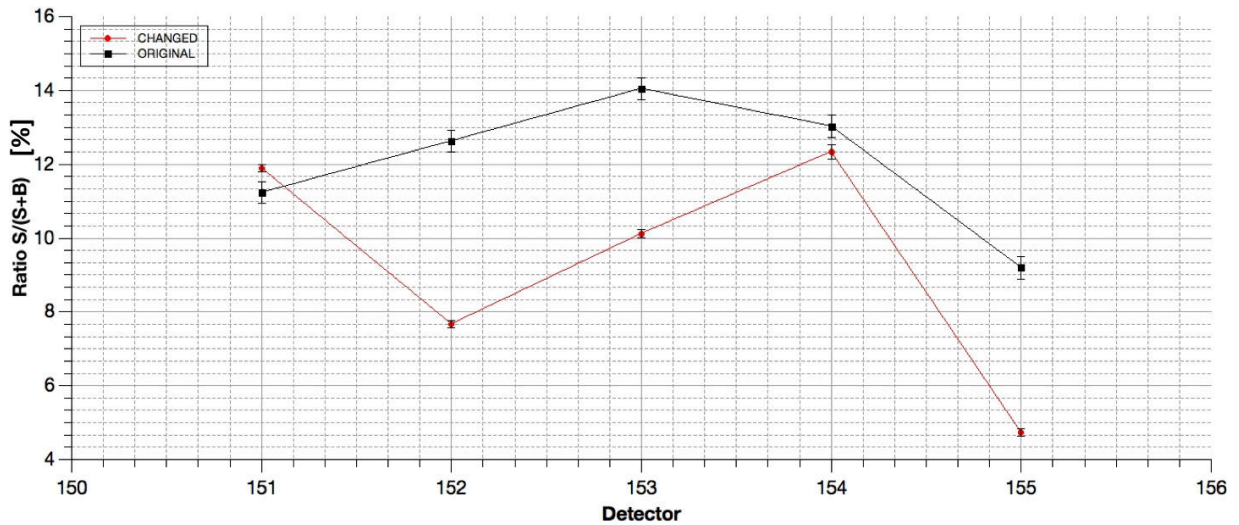


FIGURE 5.12:  $\frac{S}{S+B}$  ratio for different detectors with modified and original threshold

We can see that only in the detector number 151 (0 mV) we have a better ratio in the changed configuration. This ratio is probably peak-dependent other than detector-dependent. In fact lowering the threshold we get for sure more background that we can consider, as first approximation, constant in TOF and more signal that is TOF-dependent because different recoil peaks has different intensities (hydrogen peak more intense than carbon peak). For example at fixed detector we can consider recoil peaks of different atoms (i.e hydrogen and carbon), now lowering the threshold we add, to the acquired spectra, the same number of background events for

both peaks but less number of signal events for the smaller peak because the gold peaks added with the changing are in the same number but less intense for lower signal.

At this point we can say that the net result is a decreasing effect on the statistical relative error bars; someone could argue that it is straightforward because we have increased the number of counts and the relative errors in our experiment goes like  $\frac{1}{\sqrt{N_1}} + \frac{1}{\sqrt{N_2}}$  (where  $N_1$  and  $N_2$  are the counts of the foil-in and foil-out measurement); but we have to underline that our ability was to increment the signal and not only the background. We can say that our signal is the same that could be reached by a longer measurement and we get this just for free, modifying only some parameters. For what concerns the  $S/(S+B)$  ratio we should not be worried because what we call background is something that we can manage in a very good way trough the difference method. This is reasonable because we can distinguish background and then eliminate it. A serious problem would be if the increased background generates oscillation in the measurement (noise) but we will see that is not our case.

## 5.3 Second measurements with CCR

### 5.3.1 Time of flight spectra

We can perform the same analysis for the measurements with the CCR, same sample, were a 120 keV (100 mV) threshold is set for detectors 151-155. In figure 5.13 and 5.14 we have the comparison of the TOF spectra normalized to the proton charge between original and changed case for detector 151-152 (see appendix B for other detectors).

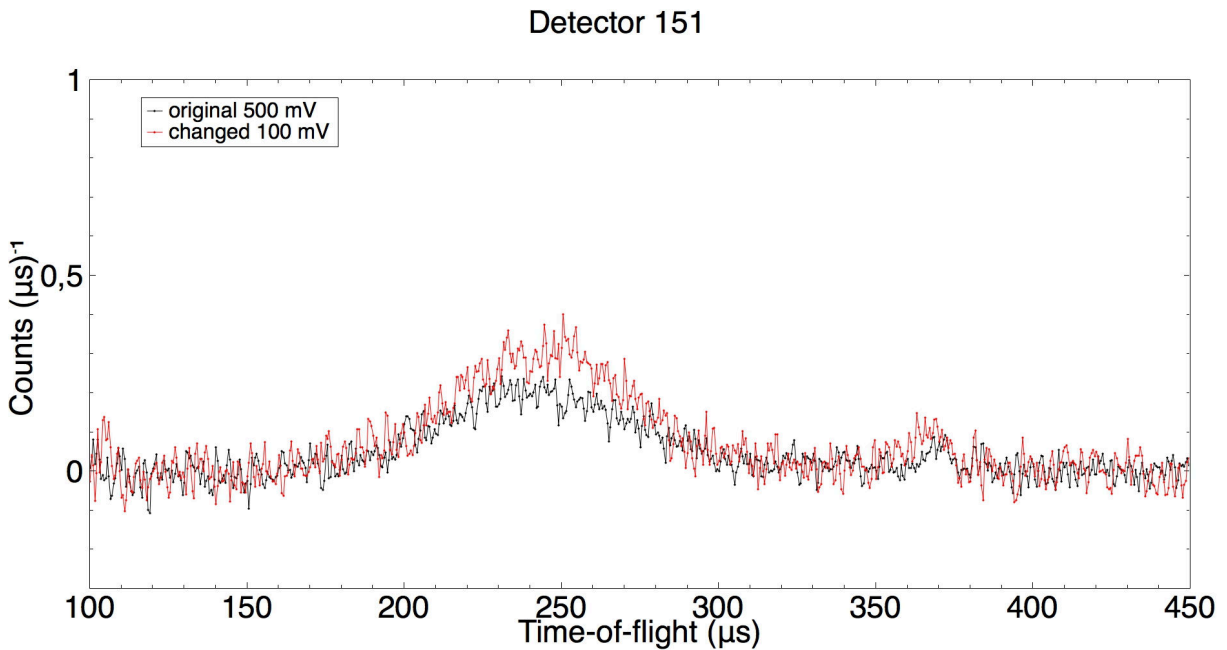


FIGURE 5.13: Comparison of polyethylene spectra, without error bars, between original and changed threshold from detector 151 using a binning of  $0.5 \mu s$  normalized only to the proton charge

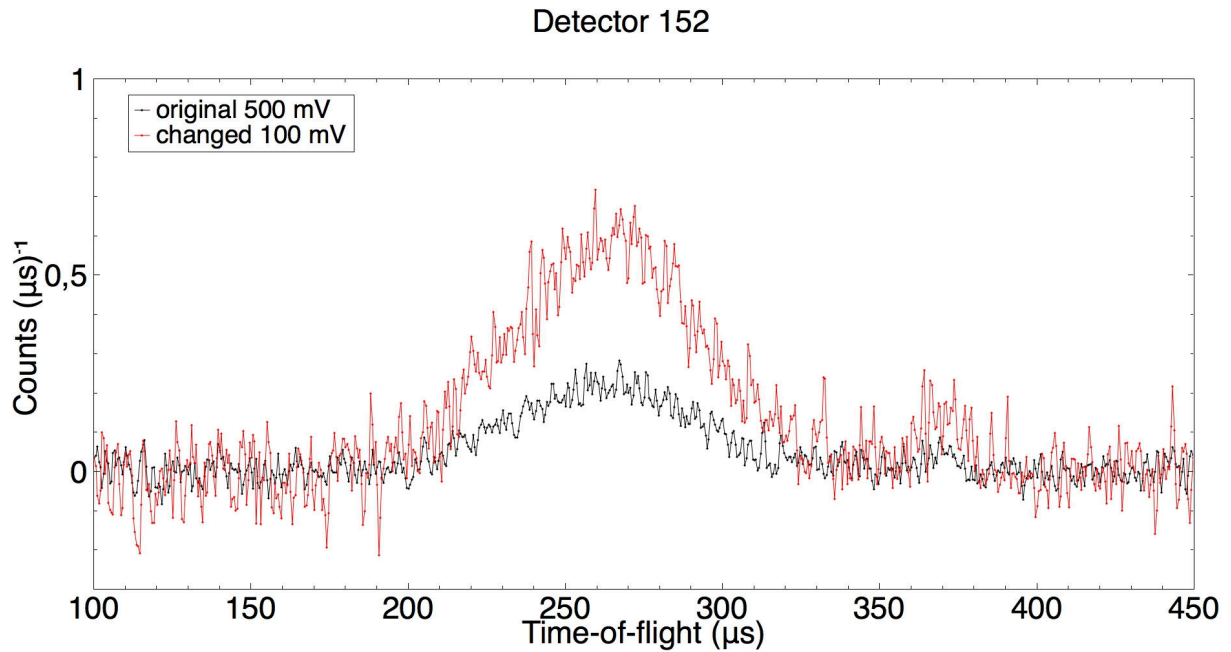


FIGURE 5.14: Comparison of polyethylene spectra, without error bars, between original and changed threshold from detector 152 using a binning of  $0.5 \mu s$  normalized only to the proton charge

As we can see from figure 5.13 probably the detector number 151 was not set in the right way because the count are not compatible with the configuration so we can't deduce conclusions coming from this detector.

In figure 5.15 it is shown the spectra normalized also to the peak area for detector 152 (see appendix B for other detectors) and in figure 5.16 the relative error bars ratio  $\frac{\Delta_c}{\Delta_o}$  for all the detectors.

As usual the relative error bars ratio is decreased in any detectors at any TOF of the spectra from 5 % to 35%.

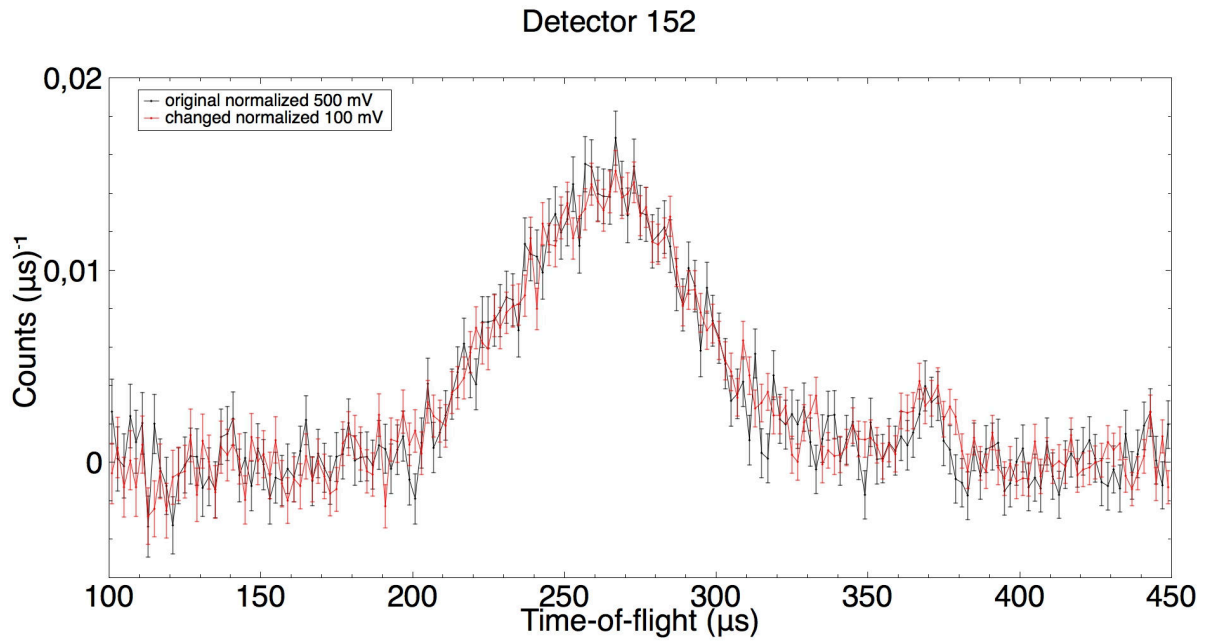


FIGURE 5.15: Comparison of polyethylene spectra, with error bars, between original and changed threshold from detector 152 using a binning of  $2 \mu s$  normalized to the proton charge and to the peak area

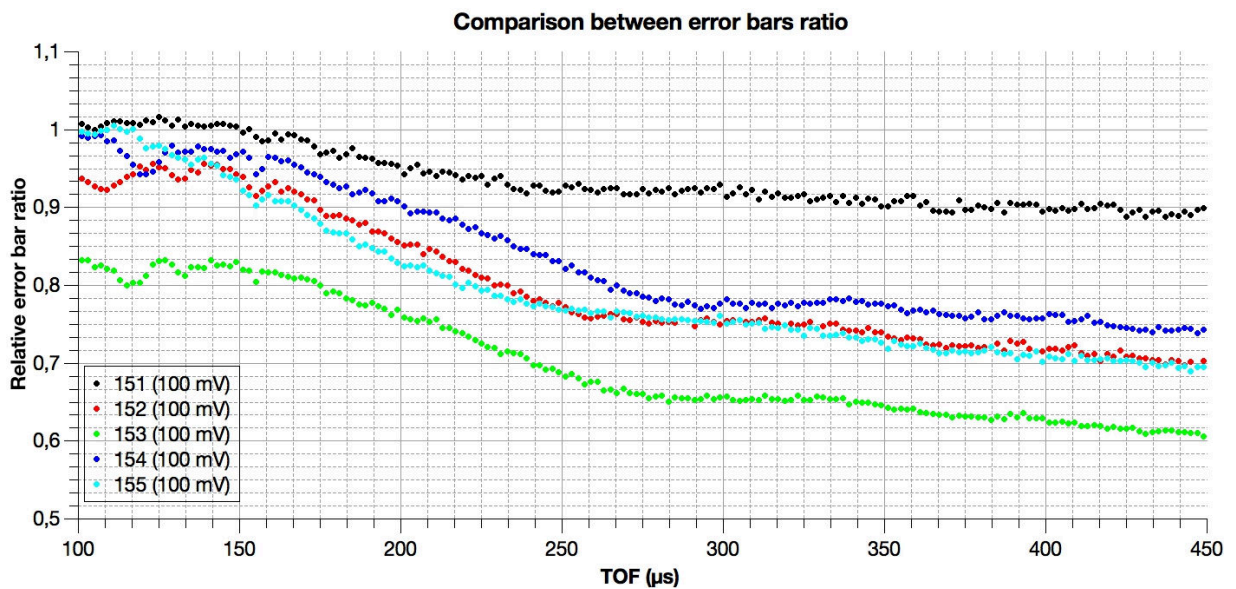


FIGURE 5.16: Comparison between ratio  $\frac{\Delta_c}{\Delta_o}$  of relative error bars from different detectors of polyethylene spectra using a binning of  $2 \mu s$

### 5.3.2 y-space spectra

Considering also the  $F(y, \mathbf{q})$  and the associated error bars ratio (figure 5.17 and 5.18) also for the second measurement we can confirm the hypothesis with a reduction from 10 % to 30 %.

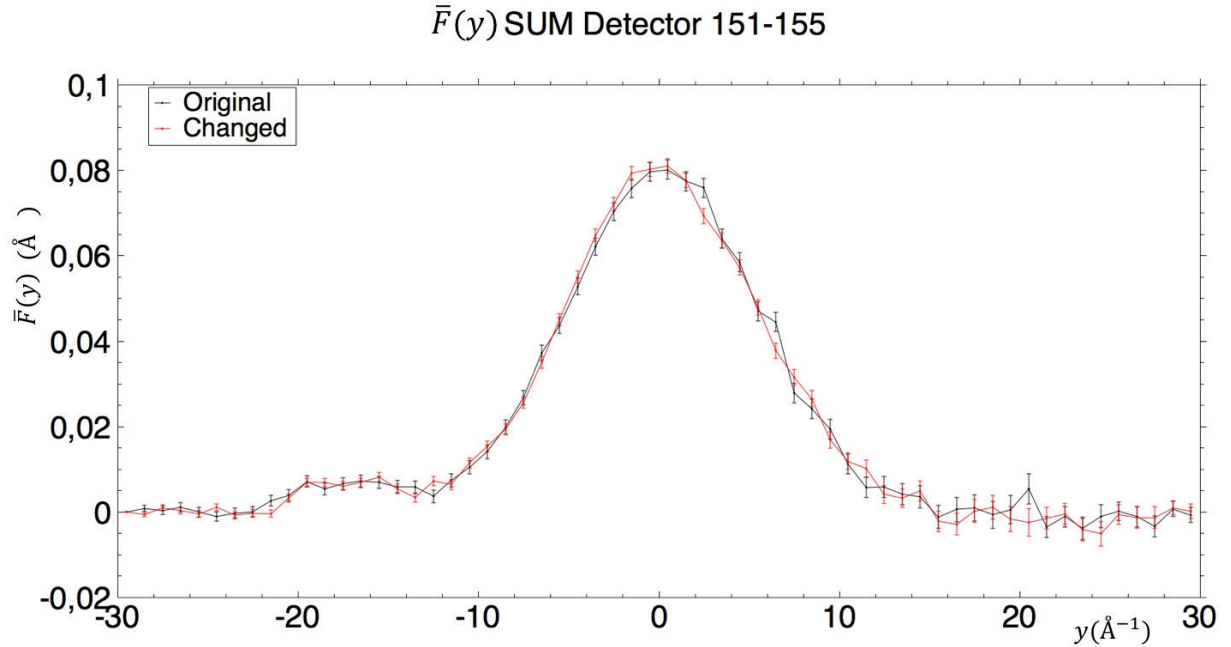


FIGURE 5.17:  $\bar{F}(y)$  spectra with normal and modified threshold summing detectors 151-155 using a binning of  $1 \text{ \AA}^{-1}$

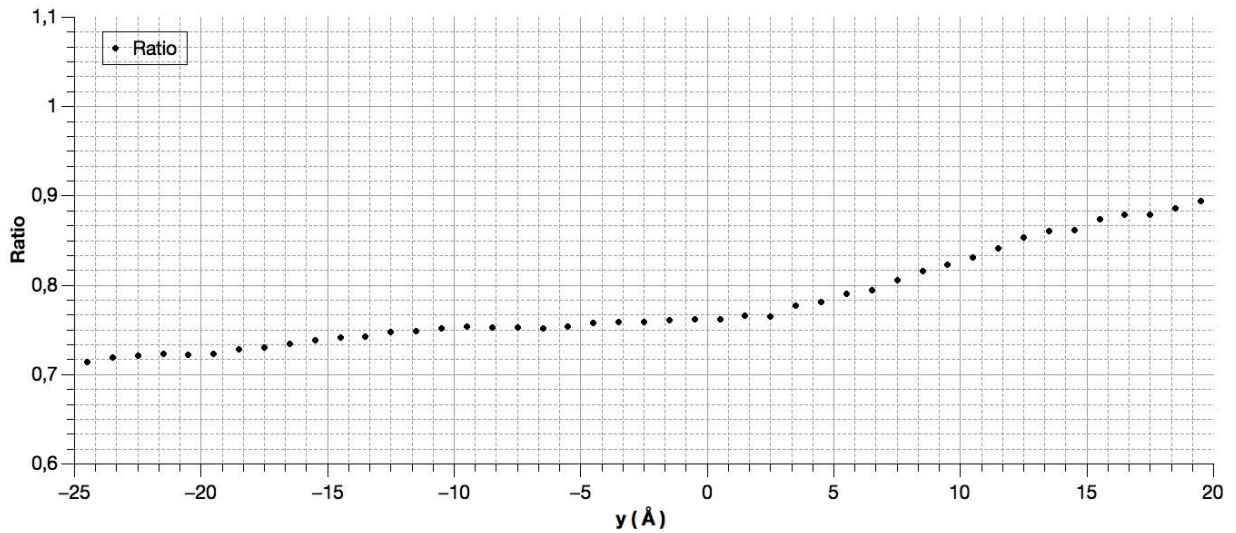


FIGURE 5.18: Ratio  $\frac{\Delta_c}{\Delta_o}$  of polyethylene  $\bar{F}(y)$  ( sum 151-155) spectrum using a binning of  $1 \text{ \AA}^{-1}$

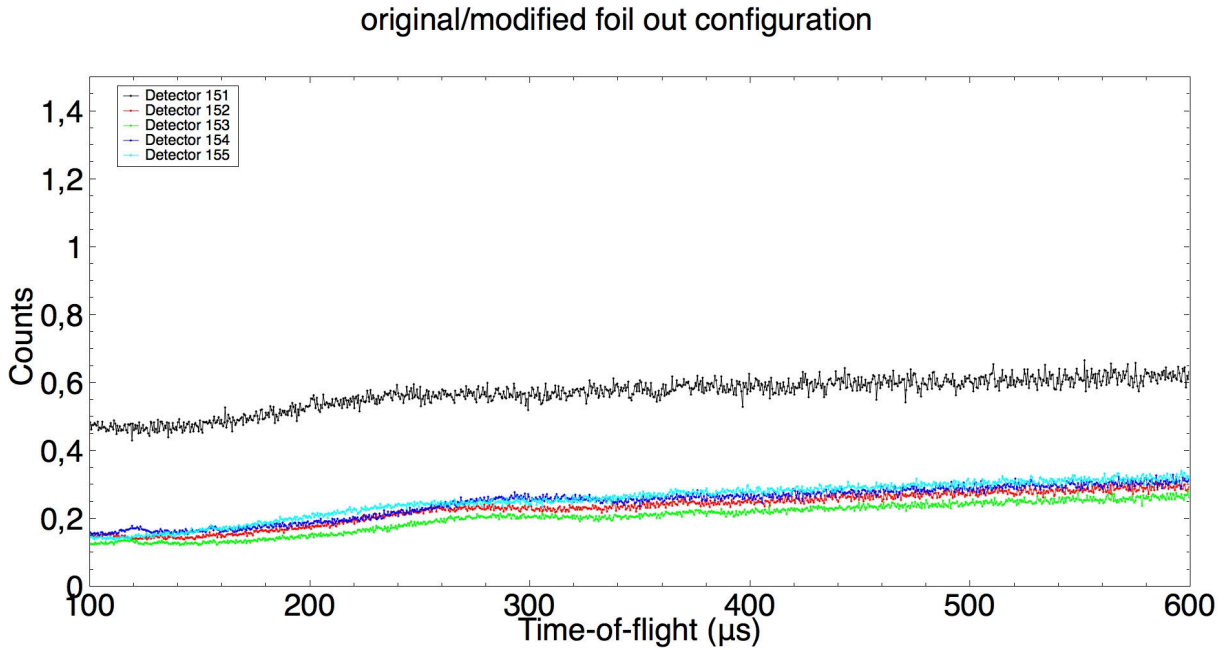


FIGURE 5.19: Ratio between the spectra in original and modified configuration acquired in the foil-out gold position

### 5.3.3 Signal background ratio

In figure 5.19 there is the ratio, in the foil-out configuration, between counts in the original configuration and counts in the changed one; we can see that lowering the threshold we have much more events (ratio less than one) and they are quite the same as the thresholds are the same. We can confirm that detector 151 was set in a wrong threshold position as we can see by its different ratio.

Analysing the  $S/(S+B)$  in the same range of table 5.3 we see from figure 5.20 that it is not improved (black line over the red one) but as we said before if the background doesn't bring to noise we can be satisfied.

## 5.4 Detector dependence

In the first measurement we wanted to discover which threshold would be the right one, but it was not possible because we need to consider the sensitivity of detectors to the threshold changing. In fact as we can see in figure 5.16 after the same threshold change we have a different responses. Now, thanks to the second measurement, we have the weapon to overcome the climb. In fact in the second part of the experiment we can quantify how much for each detector the relative error bars decrease after an identical change and that is the sensitivity. For this reason we can introduce a  $F$  factor defined as (see ref. [23])

$$F = \frac{S}{\Delta S}$$

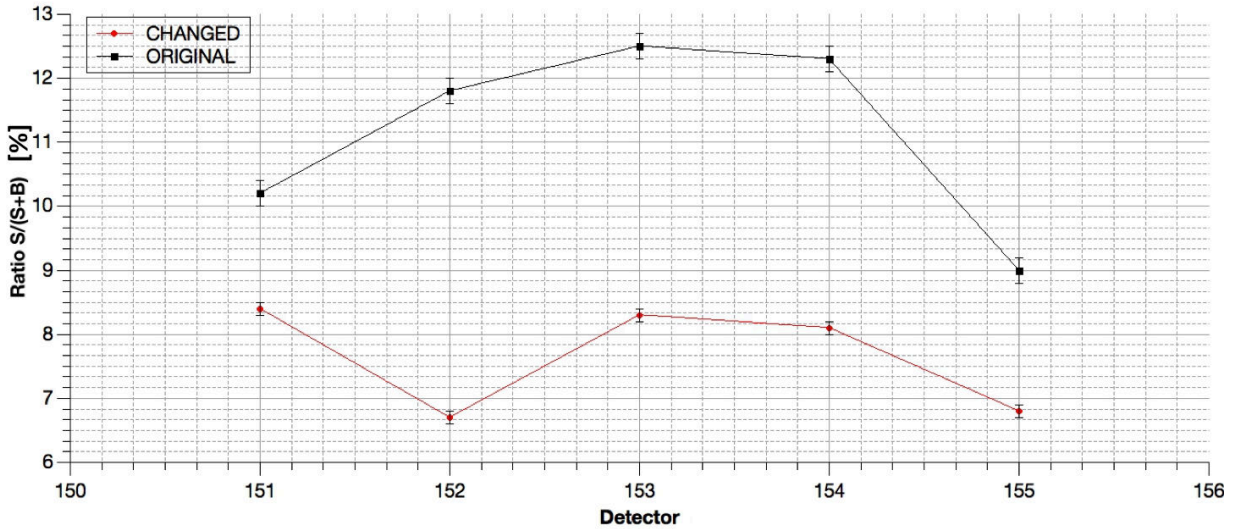


FIGURE 5.20:  $\frac{S}{S+B}$  ratio for different detectors with modified and original threshold

It is the inverse of the signal relative error and it is very useful to make some simple comparisons. First we can plot that factor in the original and modified setting, for the measurements done without the CCR (figure 5.21) and with CCR (figure 5.22).

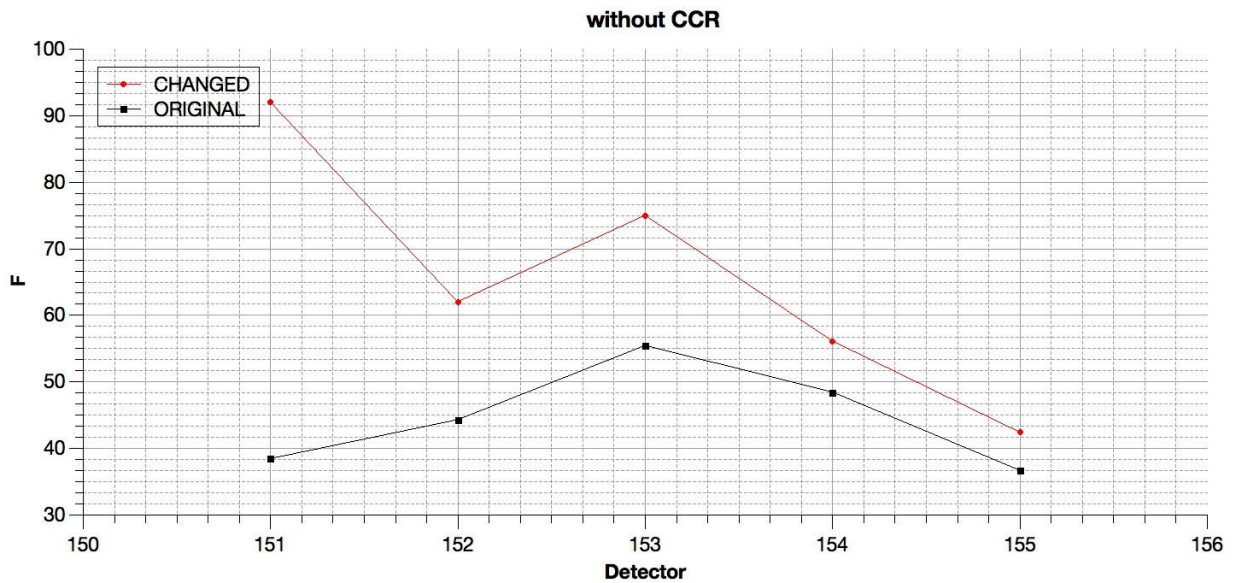


FIGURE 5.21: Comparison between the calculated F factor between original and modified setting in the measurements without CCR

Bigger is F smaller is the relative errors and we can see from these plots (5.21 and 5.22) that the line associated with the changed configuration is always over the other. In order to obtain a sensitivity  $\alpha$ , assumed constant in our energy range of interest, we can consider the measurement with CCR where every detector is at the same threshold and calculate

$$\alpha = \frac{F_{changed} - F_{original}}{(F_{changed} + F_{original})/2}$$

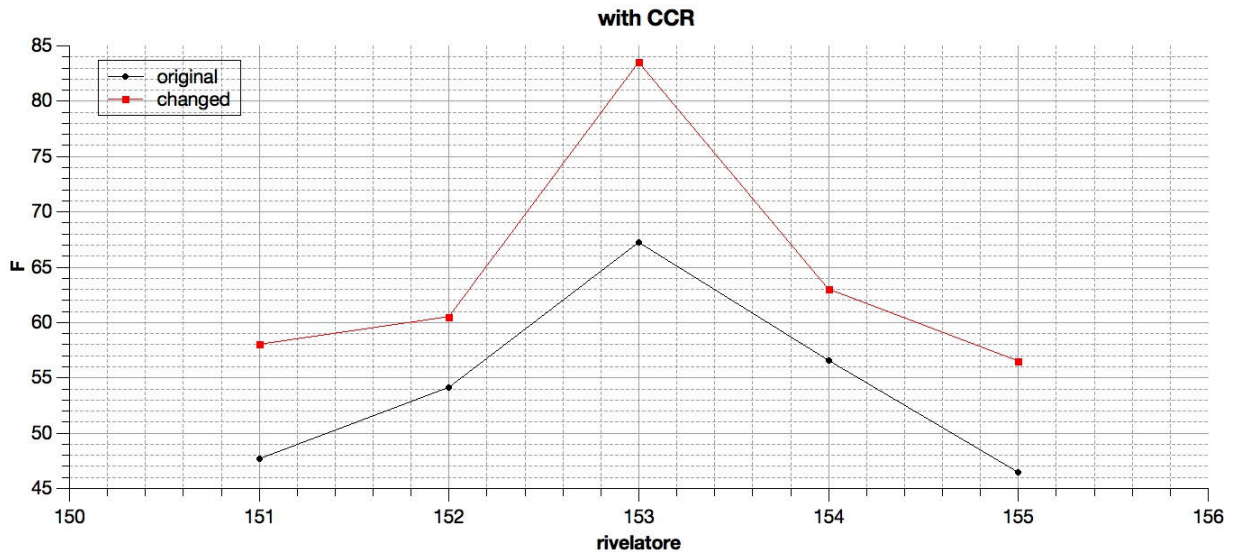


FIGURE 5.22: Comparison between the calculated F factor between original and modified setting in the measurements with CCR

After that we have taken the F factors without the CCR (different threshold for each YAP) normalising them to the sensitivity  $\alpha$  (calculated from the measurements with CCR), obtaining figure 5.23. Now it is like if we were detecting events with equal-sensitive detectors.

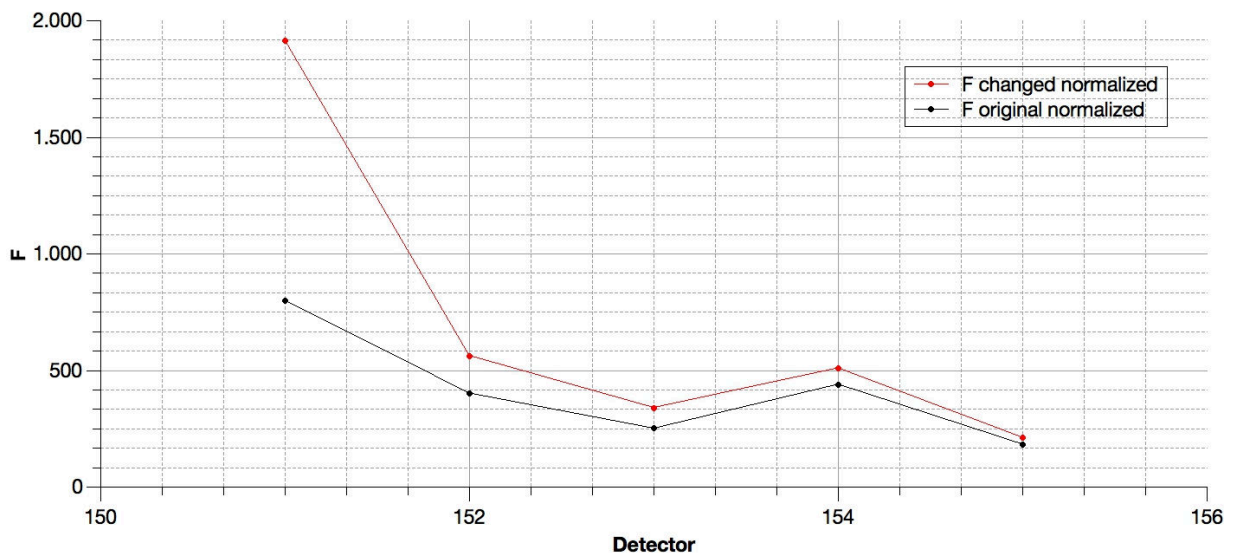


FIGURE 5.23: Comparison between the calculated F factor normalized to the sensitivity between original and modified setting in the measurements without CCR

Going easy with the detector 151 we can say looking at the F factor normalized that for sure the 100 mV threshold (detector 152) is at least the second best choice because the difference between  $F_{normalized}$  changed-original (that is the improvement) is bigger than in the other YAPs.

## 5.5 Noise reduction

In this section our concern is to verify that, despite the slight worsening of  $S/(S+B)$ , the noise, *i.e.* oscillation in the measurement, is decreased. For this purpose we can concentrate our attention on a certain region of the TOF spectra where we are sure that there are no peak (signal is around 0) and then calculate the  $\sigma$  (around the medium value  $\sim 0$ ) of the counts dispersion for the original and changed setting in the first and second part of the experiment, quantifying in this way the fluctuation, the noise. The ranges chosen are

$$\text{period 1 } (100 < t < 160) \mu s$$

$$\text{period 2 } (390 < t < 450) \mu s$$

respectively to the left of the proton peak (period 1) and to the right of the carbon peak (period 2) where the signal is around 0. The standard deviation is calculated using

$$\sigma = \sqrt{\frac{\sum_i (x_i - \rho)^2}{N - 1}}$$

Where  $x_i$  is the value of the  $i$  th bin,  $\rho$  the average value and  $N$  the total number of bin in the TOF range analysed. The result for the two periods associated with the first part of the experiment is shown in figure 5.24 where is represented the ratio  $\frac{\sigma_{\text{changed}}}{\sigma_{\text{original}}}$  for each detector.

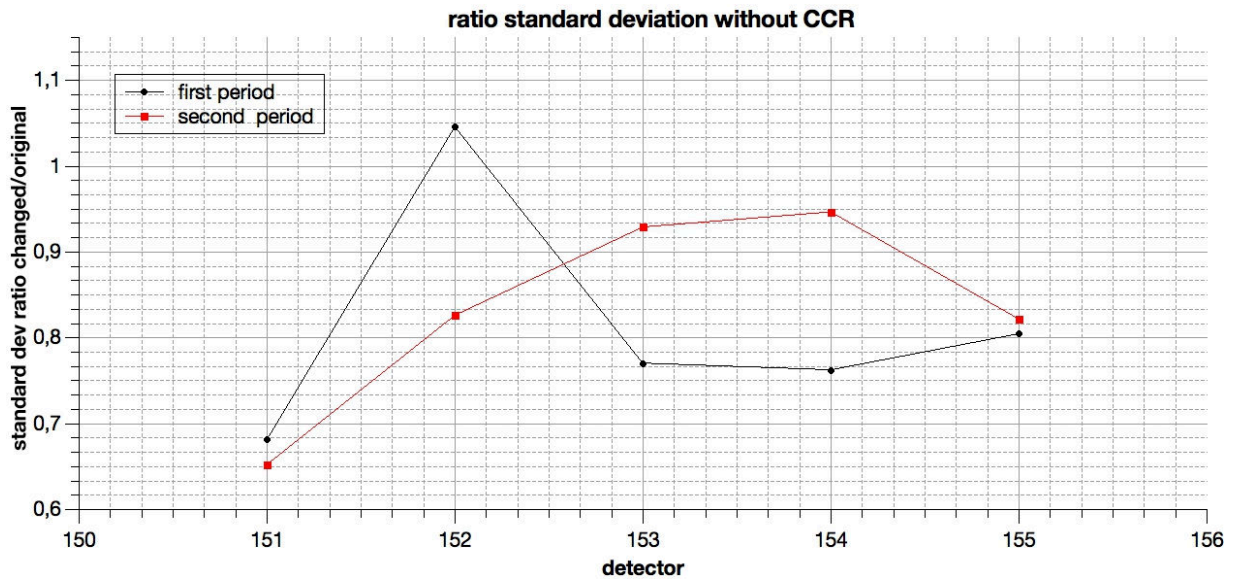


FIGURE 5.24:  $\frac{\sigma_{\text{changed}}}{\sigma_{\text{original}}}$  in the first and second period without CCR

The noise is reduced in the most detectors (the ratio is under one). Observing also the results obtained by the second part of the experiment reported in figure 5.25 we can confirm the statement.

From figure 5.26 we can see an example: there are two DINS spectra by detector 151 (0 mV), the black one comes from the changed setting and the red one comes from the original setting

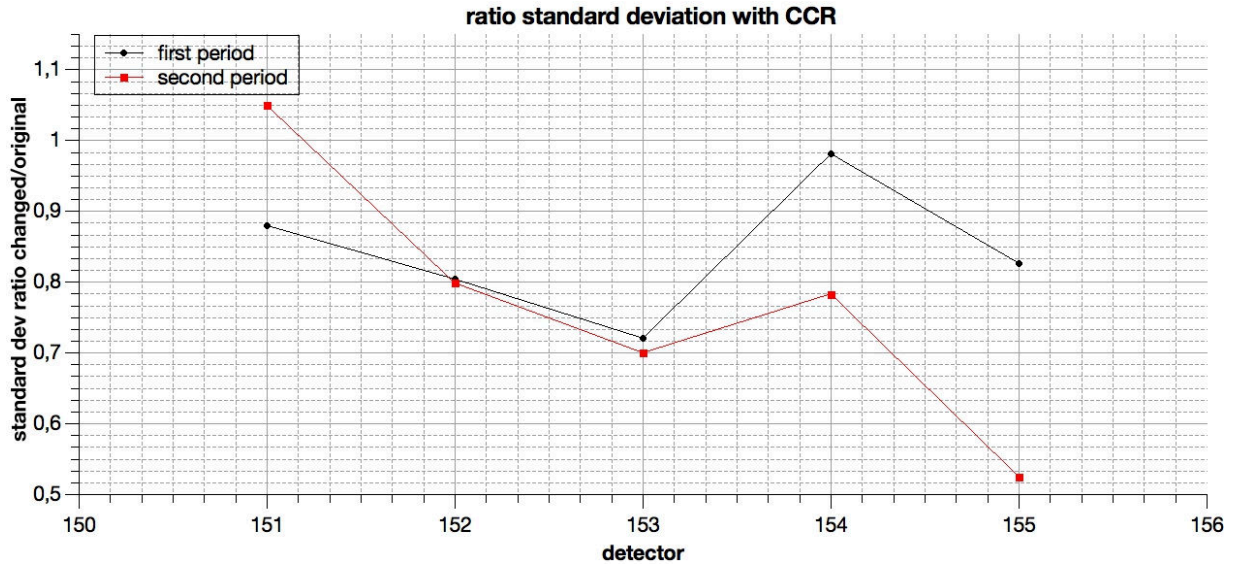


FIGURE 5.25:  $\frac{\sigma_{changed}}{\sigma_{original}}$  in the first and second period with CCR

both in the case without CCR; they are shifted by a 0.016 factor to represent more clearly our intentions. The dark green line represent the average value  $\rho$  of the counts dispersion in the different periods, the light green lines represent

$$\rho_{changed} \pm \sigma_{changed}$$

and the dark blue lines represent

$$\rho_{original} \pm \sigma_{original}$$

It is evident that the range delimited by the light green lines is smaller than the one delimited by the blue lines; it means a smaller fluctuation around the average value.

What is interesting is the distribution of all the  $\frac{\sigma_{changed}}{\sigma_{original}}$  (both periods with and without CCR for each detector) shown in figure 5.27. As we can see the histogram maximum is in the bin 0.8-0.9 associated with a noise reduction of the 20-10 %

It is so demonstrated that, even if  $S/(S+B)$  doesn't improve, there is a noise reduction. It is very a good result because what we call background is what we eliminate and control but the noise distortion is something that we cannot control in particular on the line shape of the peak, but the line shape is a crucial characteristic for the momentum distribution and so for DINS experiment itself.

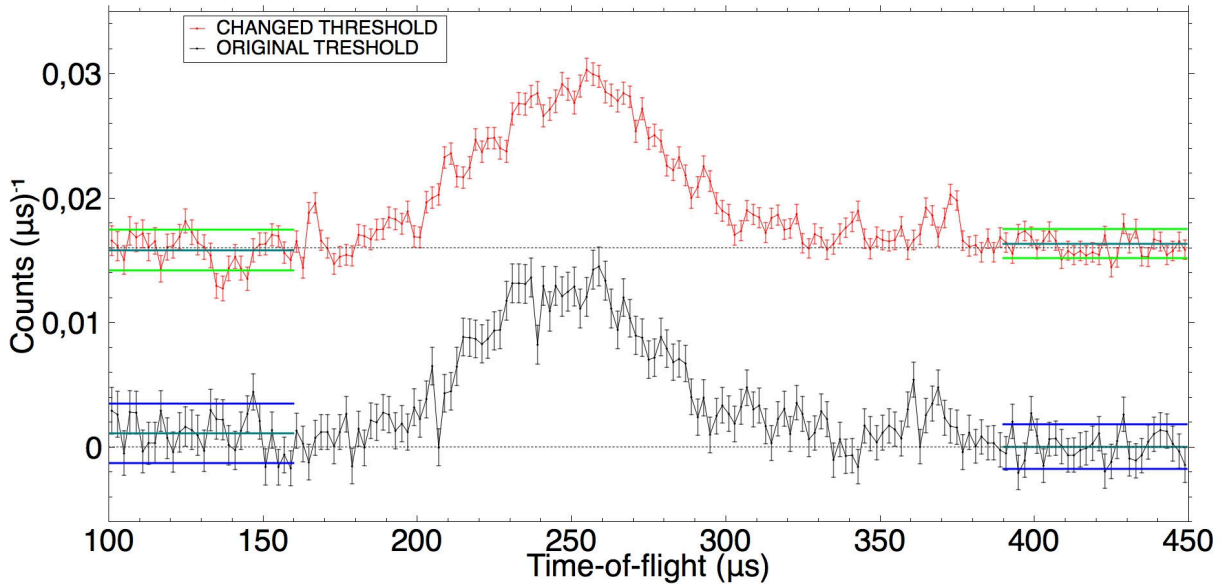


FIGURE 5.26: Two DINS spectra acquired without CCR by detector 151 (0 mV), the red one (modified setting) is shifted from the black one (original setting) by a 0.016 value. There is the representation of the TOF range of interest and the fluctuation around the average value in both cases. Light green for the fluctuation range in the modified setting and dark blue for the original setting.

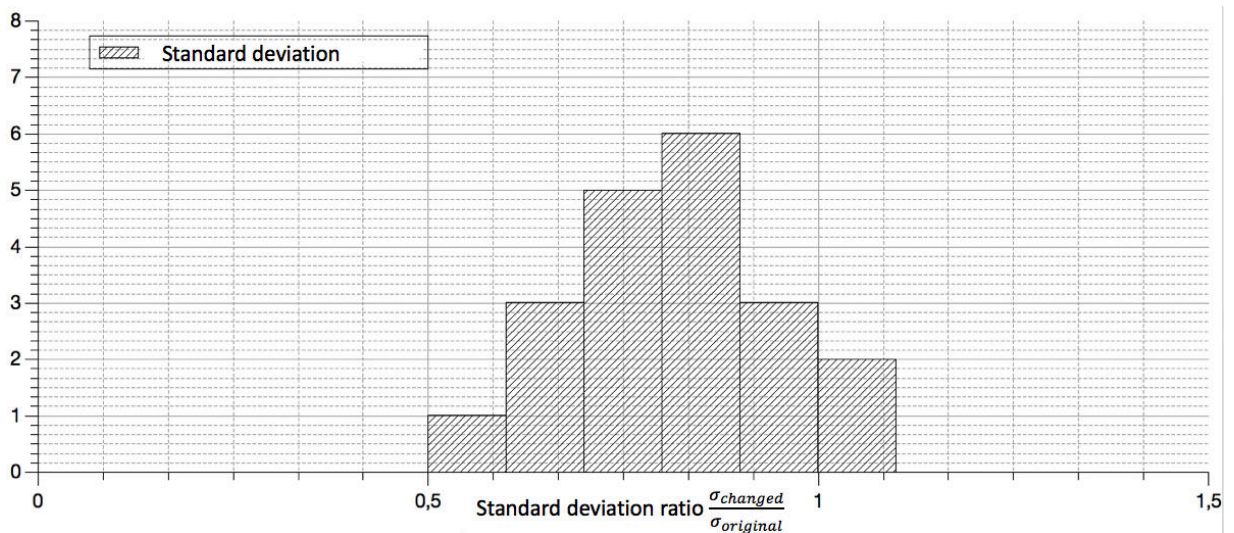


FIGURE 5.27: Distribution of the ratios  $\frac{\sigma_{changed}}{\sigma_{original}}$  coming from the first and second period of both measurements

## 5.6 Fit of the Compton profile

In the previous sections we have described the  $J(y, \hat{\mathbf{q}})$  (more precisely the experimental  $\bar{F}(y)$ ) spectra obtained in the two parts of the experiment for the changed and original setting. In fig. 5.8-5.9 and 5.17-5.18 is clear that decreasing the thresholds we have incremented the counts and optimized the relative error bars. Then in section 5.5 we have underlined also that in most of cases there is a noise reduction of  $\sim 20\%$ .

All this thing are very important improvements but we would like that this optimizations were reflected on the physical parameters generally obtained with DINS experiments. In particular we can analyse the average kinetic energy of atoms in the sample which is apart from a factor  $\frac{3\hbar^2}{2M}$  the second moment of the Compton profile distribution. The value of the variance  $\sigma^2$  is obtained fitting the distribution, the fit gives the value of  $\sigma^2$  and the associated error. In this section I will show that the error associated to  $\sigma^2$  obtained is bigger for the measurements with the standard set-up in both the first and second part of the experiment.

The python script used for fitting is reported in appendix C.

In this script first of all we insert information about the position of the detectors with an *ip file* then we load the data subtracting foil-in and foil-out with the *loadVesuvio* function and then, to avoid overlaps, we rebin the spectra focusing ourself only to a region where we are sure that there are not contributions of the second resonance of gold ( $\sim 70eV$ ).

In a second part of the script there is an analytical correction of the background that is not eliminated by the subtraction method. In fact the gamma background emitted by the cycling gold foil is different when it is in the two different position. After that, to focus ourselves on the hydrogen peak, we remove the carbon peak. In order to do this we fit the carbon peak with the constraint that it should have a certain intensity determined by the stochiometric presence of carbon in the sample and by the carbon cross section. In our case the carbon is twice the hydrogen in polyethylene and  $\sigma_H = 82b$ ,  $\sigma_C = 5.51b$  so

$$\frac{I_H}{I_C} = 2 \frac{\sigma_H}{\sigma_C} = 29.8$$

The fit used to eliminate the carbon peak is shown in fig. 5.28

After the carbon subtraction we perform the transformation to the  $y - space$  for the hydrogen peak and create a workspace with  $\frac{1}{q}$  for the final state correction proportional to  $\frac{1}{q} \frac{d^3 J(y)}{dy}$ . As we can see in fig. 5.29 the real spectrum finishes at a certain value of  $q$  because the time of flight spectrum used was cut to eliminate the second gold resonance so at that  $y$  the kinematic space ends.

In order to avoid that our fit will be influenced by the 0 value of the spectrum, and associated errors, after the end of the kinematic space, we have incremented the error bars, see fig. 5.30. In this way the fit will not feel constraints from that points.

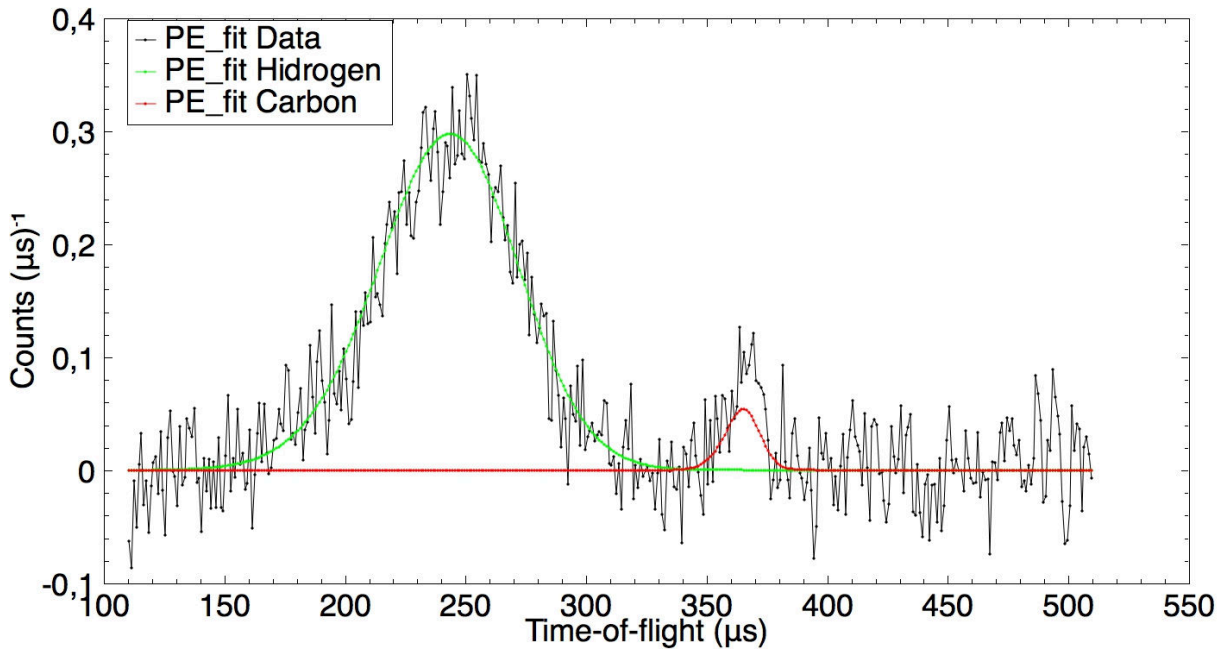


FIGURE 5.28: Fit of the recoil peaks to eliminate the carbon peak of the spectrum acquired with detector 151 in the second part of the experiment (same threshold for the detectors) with threshold lowered. In green the hydrogen peak fit and in red the carbon peak fit.

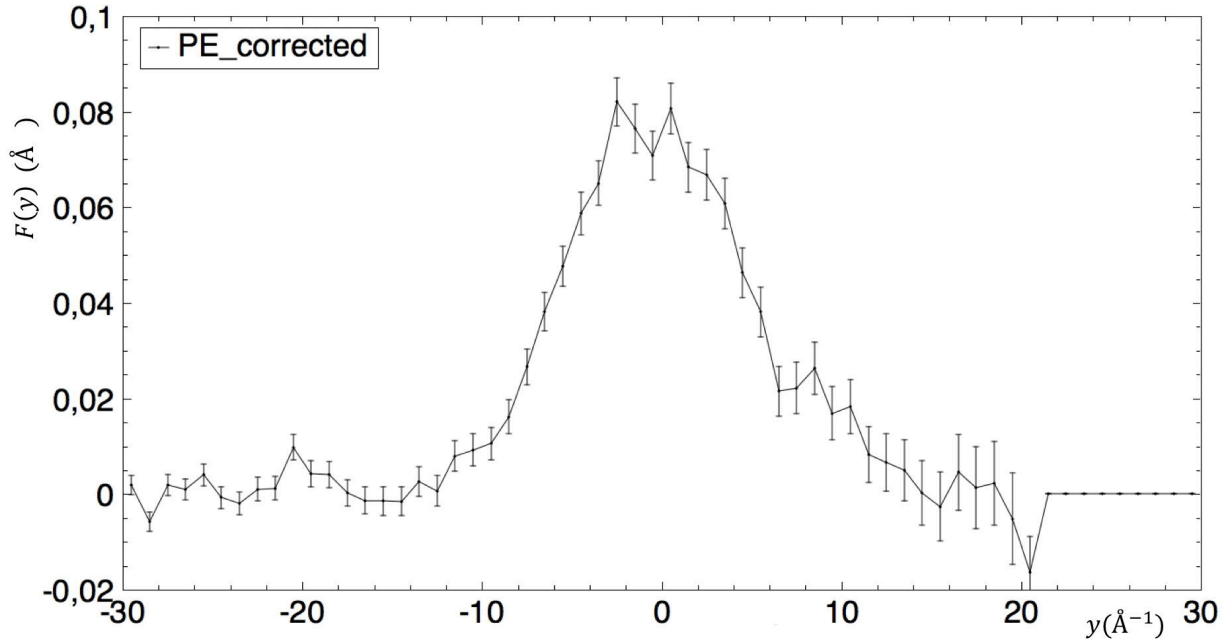


FIGURE 5.29: Isolated experimental hydrogen Compton profile of the spectrum acquired with detector 151 in the second part of the experiment (same threshold for the detectors) with threshold lowered.

Before the final fit we have to define the resolution function. In fact the fit function will be the convolution of the  $J(y, \hat{q})$  distribution (connected to  $n(p)$  and taken as a simple Gaussian) and the resolution function of the spectrometers. In particular the resolution function is the

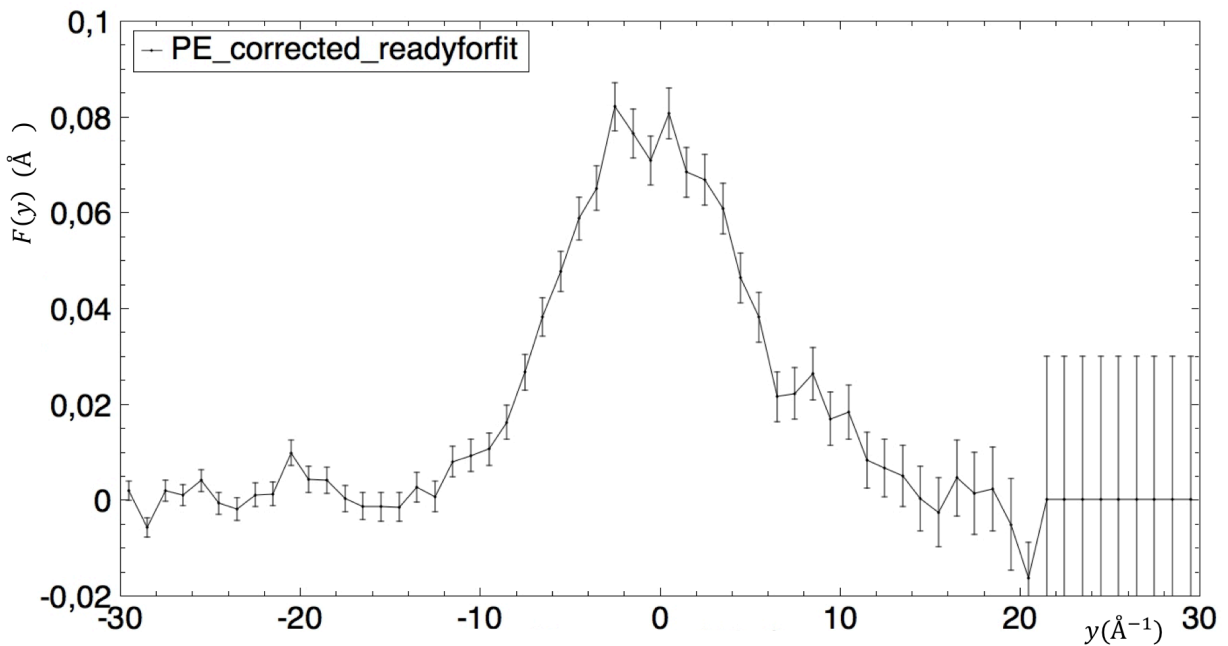


FIGURE 5.30: Isolated experimental hydrogen Compton profile whit errors associated to the end of kinematic space modified. The spectrum is acquired with detector 151 in the second part of the experiment (same threshold for the detectors) in the modified setting.

convolution of the geometrical Gaussian uncertainty functions (due for example to the solid angle covered by detectors uncertainty), the Gaussian function of the Doppler broadening of the gold foils atoms (temperature effect) and the Lorentzian function of the radiative neutron capture resonance (Brait-Weigner).

The fit used is a global fit because we have five distributions  $F(y, \mathbf{q})$  to fit (one for each detector modified). It is used a global  $\chi^2$  minimization in fact instead of

$$\chi_r^2 = \sum_i \left[ \frac{F_r(x_i) - M_r(x_i)}{E_r(x_i)} \right]^2 \quad (5.1)$$

is used

$$\chi^2 = \frac{1}{N} \sum_r \sum_i \left[ \frac{F_r(x_i) - M_r(x_i)}{E_r(x_i)} \right]^2 \quad (5.2)$$

where  $r$  is associated to the  $r$  detector,  $i$  is associated to a certain point of the spectrum,  $N$  is the total number of detectors,  $F(x)$  is the experimental data,  $M(x)$  is the fit function value and  $E(x)$  is the experimental error. As we can see in the 5.2 we don't have the detector dependence. In fact for each detector the fit algorithm calculate the  $\chi_r^2$  using the value of the three free parameters in the fit function (centroid, heigh and standard deviation of the real  $J(y, \hat{\mathbf{q}})$  in fact the resolution function is considered fixed) and then sum for all the detectors obtaining  $\chi^2$ . The constraint is that the  $\sigma^2$  value is the same for all detectors because it is the expression of the same physics. Then the fit changes the parameters obtaining another value of  $\chi^2$  building the  $\chi^2$  distribution. The best value of this distribution ( $\chi^2$  near as possible to 1) defines the value of the parameters.

In fig.5.31 is represented the calculated fit function, the experimental data and the difference between them.

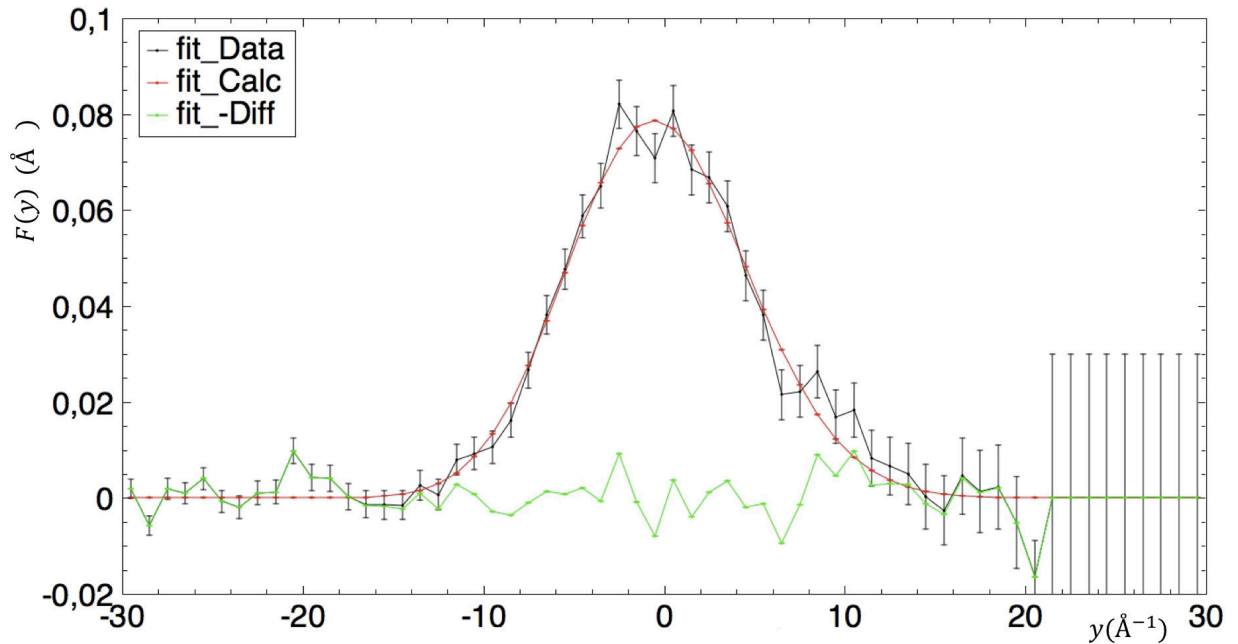


FIGURE 5.31: Calculated fit function in red , the experimental data in black and the difference between them in light green. The experimental Compton profile spectrum is acquired with detector 151 in the second part of the experiment (same threshold for the detectors) in the modified setting.

Now we can compare the  $\sigma_{original}^2$  and  $\sigma_{changed}^2$  obtained in the first (without CCR and different threshold for detector 151-155) and second part of the experiment (with CCR and same threshold 120 keV for detector 151-155). The results are shown in table 5.4

	First measurement ( $\text{\AA}^{-1}$ )	Second measurement ( $\text{\AA}^{-1}$ )
$\sigma_{original}^2$	$4.97 \pm 0.18$	$5.12 \pm 0.16$
$\sigma_{changed}^2$	$4.92 \pm 0.10$	$4.86 \pm 0.14$

TABLE 5.4:  $\sigma^2$  values obtained fitting the Compton profile distribution in the two measurements for both changed and original threshold.

As we can see for the first measurement we have decreased the error associated to  $\sigma^2$  by  $\sim 45\%$  and in the second measurement by the  $\sim 13\%$ ; probably it could mean that a great contribution of signal is under 120 keV. Furthermore the results in the changed and original threshold are compatible so we are not modifying the physics under the detection method.

## Chapter 6

# Conclusions

In this thesis I have shown that if we decrease the photon forward detectors' threshold we get a lower relative statistical error and a lower noise at the expense of the signal background ratio. It is achieved in both parts of the experiment with a reduction from 5 % to 40 % of the relative error. At a first instance, in the first type of measurements, it was difficult to decide the best threshold for this resonance detector system because we didn't have access to detector sensitivity; only after the second part of the experiment we could find the right choice normalizing the data to the sensitivity. Anyway because of the probable error done setting the threshold of detector 151 ,in the second part of the experiment, we have to neglect the results associated to it and consider 100 mV as the best choice (for sure at least the second one). The second result of this experiment is the fluctuation and noise reduction of  $\sim 20\%$  on average.

These two goals are of primary importance in the study of the line shape of  $J(y, \hat{\mathbf{q}})$ . In fact usually performing a fit on  $F(y, \mathbf{q})$  dispersion we have a lot of function that can be used and a big error on some important parameter of the fit function, i.e. the mean kinetic energy coming from the second momentum of  $n(p)$ . As a consequence the improvements are reflected also in the average atom kinetic energy, strictly connected to the variance  $\sigma^2$  of the Compton profile distribution. This value are reported in table 6.1 where is clear the optimization the  $\sigma^2$  uncertainty changing the LLD threshold that decrease the errors by the 45% and 13% of the original value.

	First measurement ( $\text{\AA}^{-1}$ )	Second measurement ( $\text{\AA}^{-1}$ )
$\sigma_{original}^2$	$4.97 \pm 0.18$	$5.12 \pm 0.16$
$\sigma_{changed}^2$	$4.92 \pm 0.10$	$4.86 \pm 0.14$

TABLE 6.1:  $\sigma^2$  values obtained fitting the Compton profile distribution in the two measurements for both changed and original threshold.

The apparently worse result of the signal background ratio is overturned noting that we don't have to be afraid of something that we can manage, subtract and eliminate unless it brings other effects. In our case a bigger background could cause a saturation of detectors or an increasing noise, but we didn't see them both; on the contrary we find a fluctuation reduction.

There is the necessity to perform other experiments like this to analyse in a more systematic way the possible improvement, maybe using more detectors increasing the statistics. Furthermore in

future measurements an Upper Level Discrimination threshold could be used to measure only photons with energy lower than 300 keV, for example, or low energy sensitive detectors such as Gas Electron Multiplier (ref. [26] and [27]). This procedure could give the possibility to enlarge in an ulterior way the signal counts

What is analysed in this thesis could be of great importance on the VESUVIO neutron science because a problem that can be underlined in this spectroscopy is the big errors due to the subtraction foil cycling system. We can also assert that decreasing noise and error bars will open the way to a new type of experiments not only more precise but also with more physical information. For example the supercritical water, probably used in the future nuclear reactors of 4<sup>th</sup> generation because of its high specific heat, has a low density ( $\sim 0.3 \frac{g}{cm^3}$ ); it means that only incrementing the neutron scattering signal we could perform a proper characterization making possible its application. Finally the optimization of the detection systems which exploits the  $(n, \gamma)$  reaction is useful also in every set-up where is present a mixed *neutron* –  $\gamma$  field.

## Appendix A

# Bi-parametric measurements

There are two important techniques used to study the isotope identification and quantification in samples that can be very useful in our experiment:

- Neutron Resonance Capture Analysis (NRCA)
- Prompt Gamma Activation Analysis (PGAA)

In the NRCA is exploited the  $(n, \gamma)$  reaction (radiative neutron capture) to study the photons emitted by a sample (ref. [28]). In this technique is analysed the time of neutron travel (the travel time of photons is negligible) obtaining the energy value of the radiative absorption (smaller TOF-higher neutron energy-resonance peak at higher energy) which is characteristic of an isotope. The different peaks give information about the different isotopes and so about the elemental composition.

In the PGAA is used the radiative neutron capture  $(n, \gamma)$  to study the energy of photons emitted by a sample (ref. [29]). In fact each isotope has a characteristic emission spectrum of  $(n, \gamma)$ , in other words after the absorption of a neutron there is the emission of a photon but the energy of the photon has a certain value with a probability described by a cross section. This emission is different for different elements obtaining the elemental composition.

The bi-parametric acquisition is obtained merging the PGAA and NRCA technique (ref. [30]). In this way we get the Time resolved Prompt Gamma Activation Analysis (T-PGAA) with 3-D bi-parametric map (see fig. A.1) which gives information about the energy spectrum of photon emitted at a certain TOF. The T-PGAA could be useful for example when two resonance TOF peaks (energy peaks) of different element of isotopes are indistinguishable, in this case the NRCA (PGAA) nature of T-PGAA is useless and it could be used the PGAA (NRCA) nature.

In our experiments the bi-parametric (T-PGAA) acquisition has a different function. In fact we are studying the  $(n, \gamma)$  photons emitted by the analyser foil that is not our sample but only a tool to select energy and isolate the signal. The result, in the standard forward VESUVIO measurements with YAP detectors, is a TOF spectra characterized by recoil peaks due to photons emitted by the gold foil analyser. The recoil peaks are situated at a certain TOF value and we don't have information about the energy of photons who build the peak but only the neutron travel time. This measurement is very similar to the NRCA.

Sometime it is useful to study the energy distribution of the photons emitted by the analyser due to the neutrons scattered by a certain sample. In fact each TOF peak is *built* by photons

emitted by the gold foil but also background photons emitted by the blockhouse. Using the tabulated (or measured) energy distribution of photon emitted by  $(n, \gamma)$  analyser reaction we are able to distinguish the signal from the background simply because background photons have a different energy distribution. This measurements are usually performed with an High Purity Germanium detector which have a good time and energy resolution. The Germanium-based detectors are not used in the VESUVIO bank. So if we can't select only the energy region where there is only signal photons because we don't have bi-parametric acquisition for standard detectors we can use the Germanium detector to individuate regions where the signal is dominant and finally chose the right threshold for the Low Level Discrimination threshold for the YAP detectors.

In fig. A.1 there is a typical bi-parametric acquisition

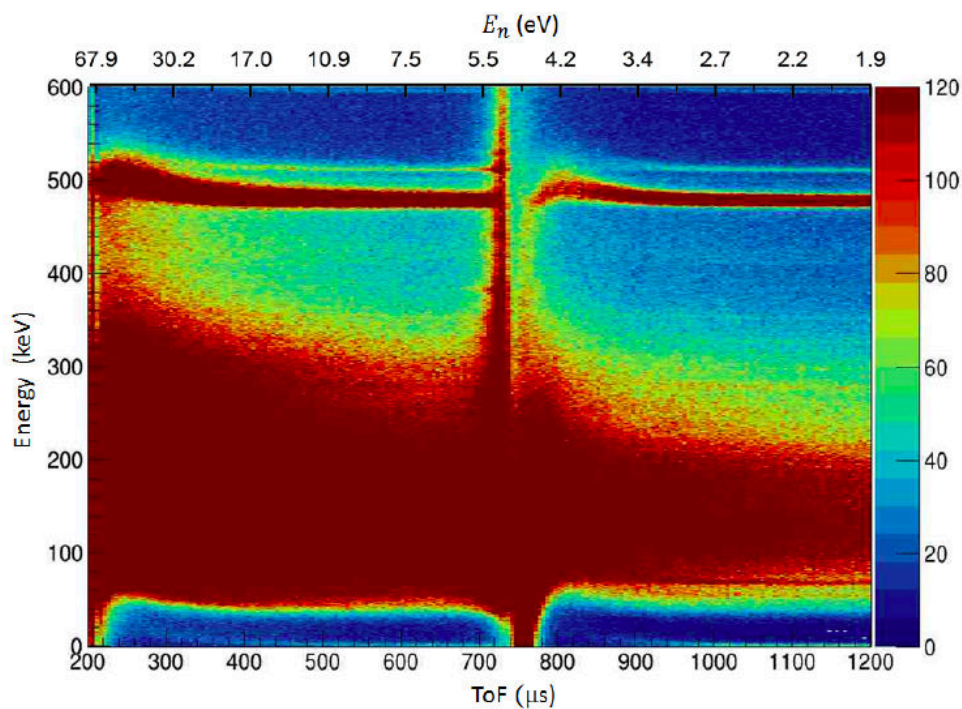


FIGURE A.1: Bi-parametric map ( $\gamma$  energy - TOF) of gold measured with High Purity Germanium, ref. [24].

## Appendix B

# Other time of flight spectra

In this section I insert the total number of spectra acquired, omitted in the text to facilitate the lecture. Figures B.1 - B.8 are comparison associated to the first part of experiment where thresholds were different for each detector and figures B.9 - B.15 are comparison associated to the second part of the experiment where the threshold is the same for each detectors.

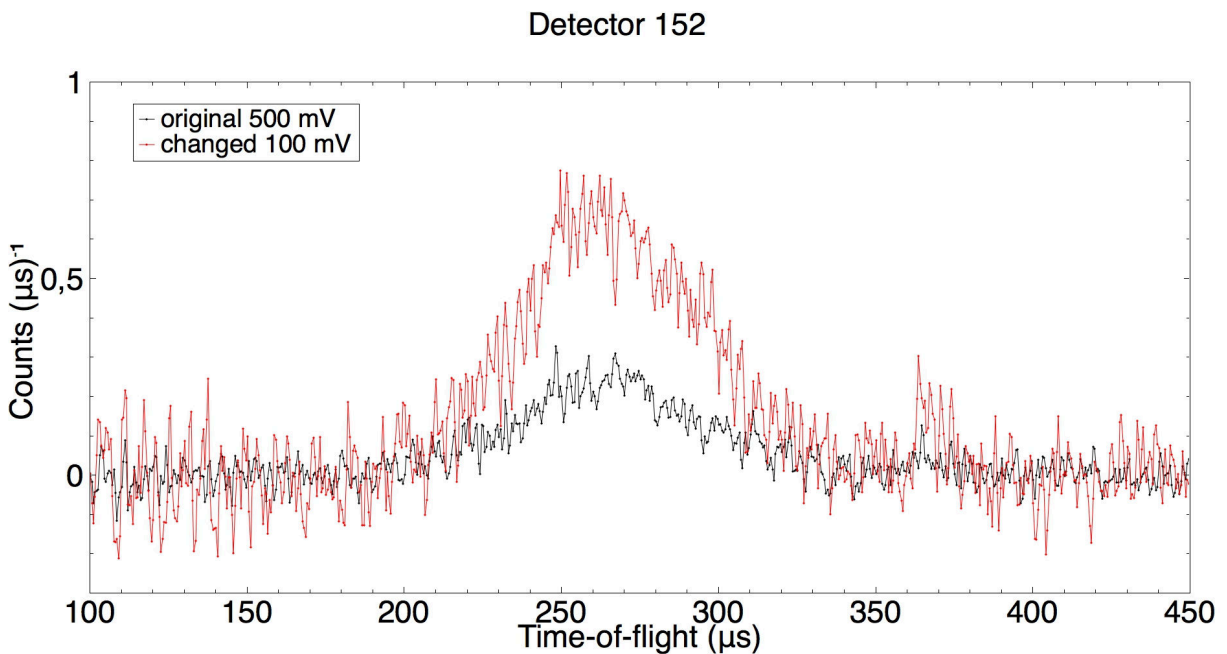


FIGURE B.1: Comparison of polyethylene spectra, without error bars, between original and changed threshold from detector 152 using a binning of  $0.5 \mu\text{s}$  normalized only to the proton charge

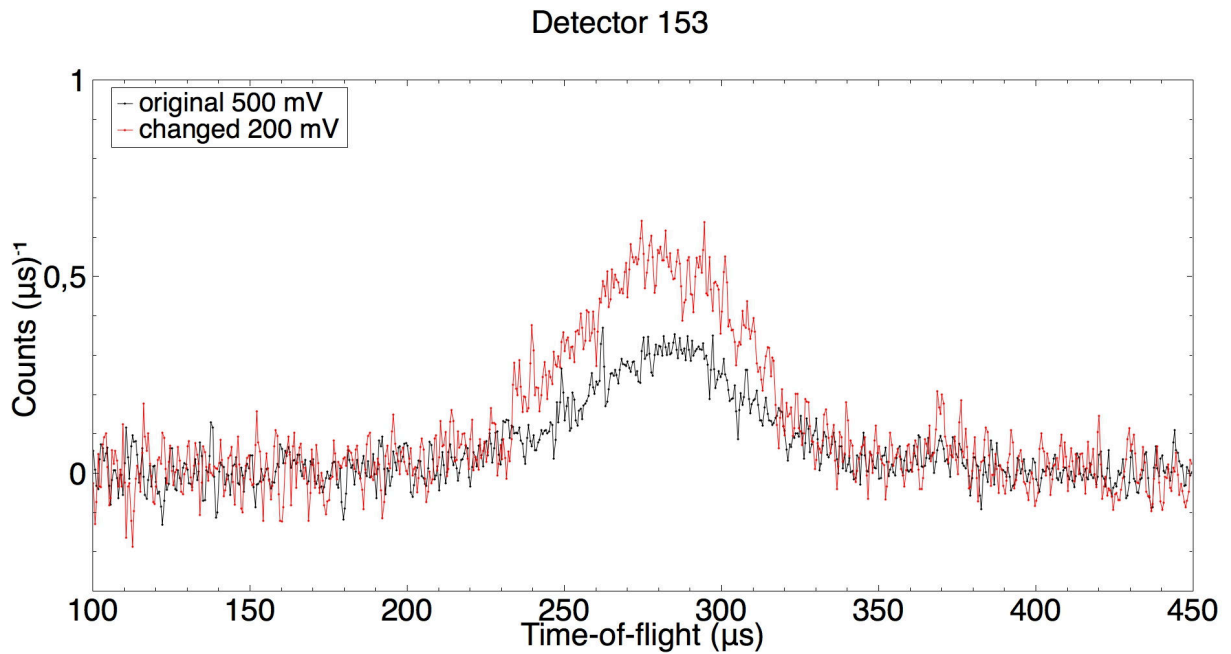


FIGURE B.2: Comparison of polyethylene spectra, without error bars, between original and changed threshold from detector 153 using a binning of  $0.5 \mu\text{s}$  normalized only to the proton charge

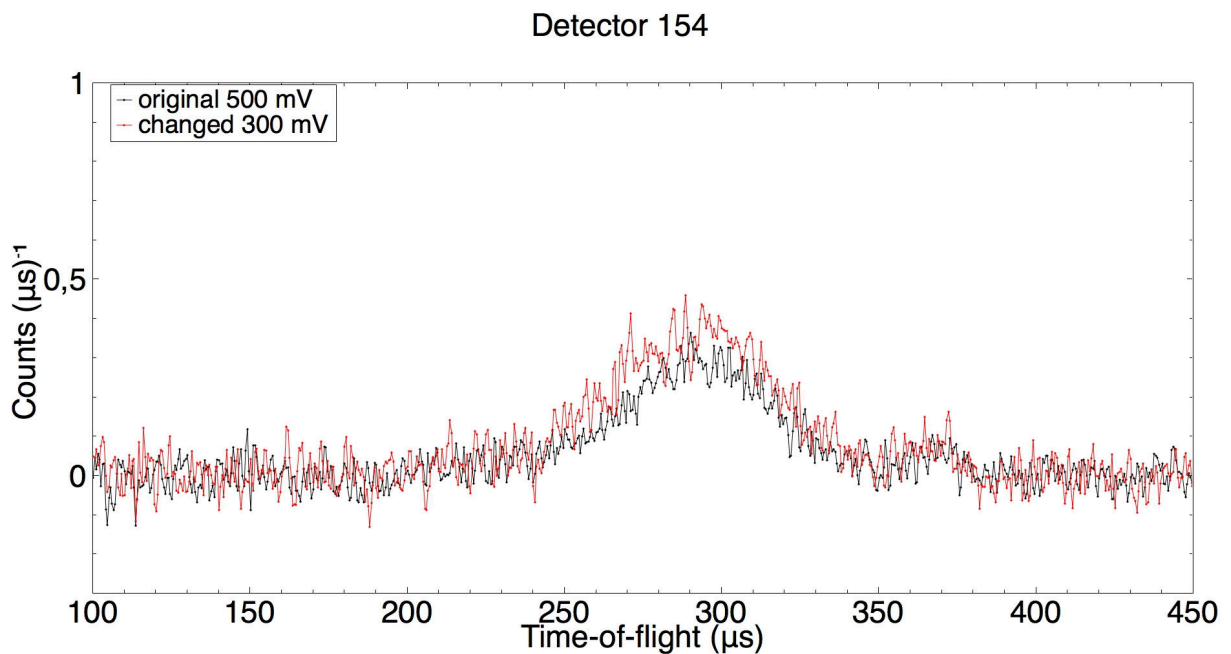


FIGURE B.3: Comparison of polyethylene spectra, without error bars, between original and changed threshold from detector 154 using a binning of  $0.5 \mu\text{s}$  normalized only to the proton charge

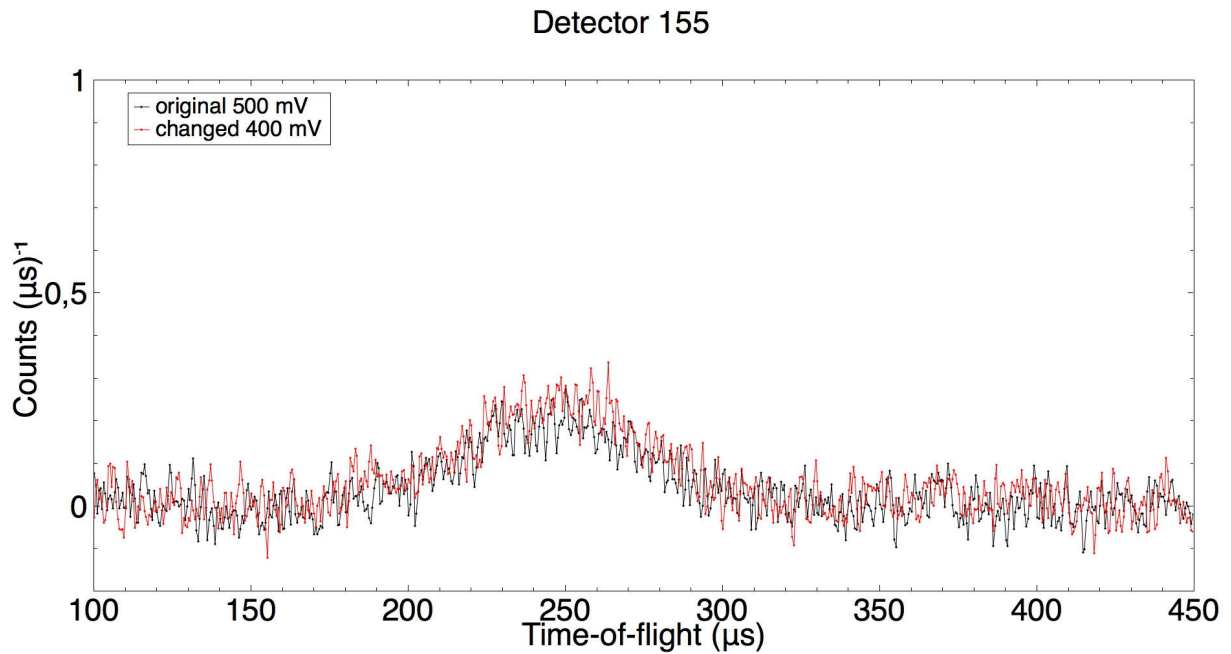


FIGURE B.4: Comparison of polyethylene spectra, without error bars, between original and changed threshold from detector 155 using a binning of  $0.5 \mu\text{s}$  normalized only to the proton charge

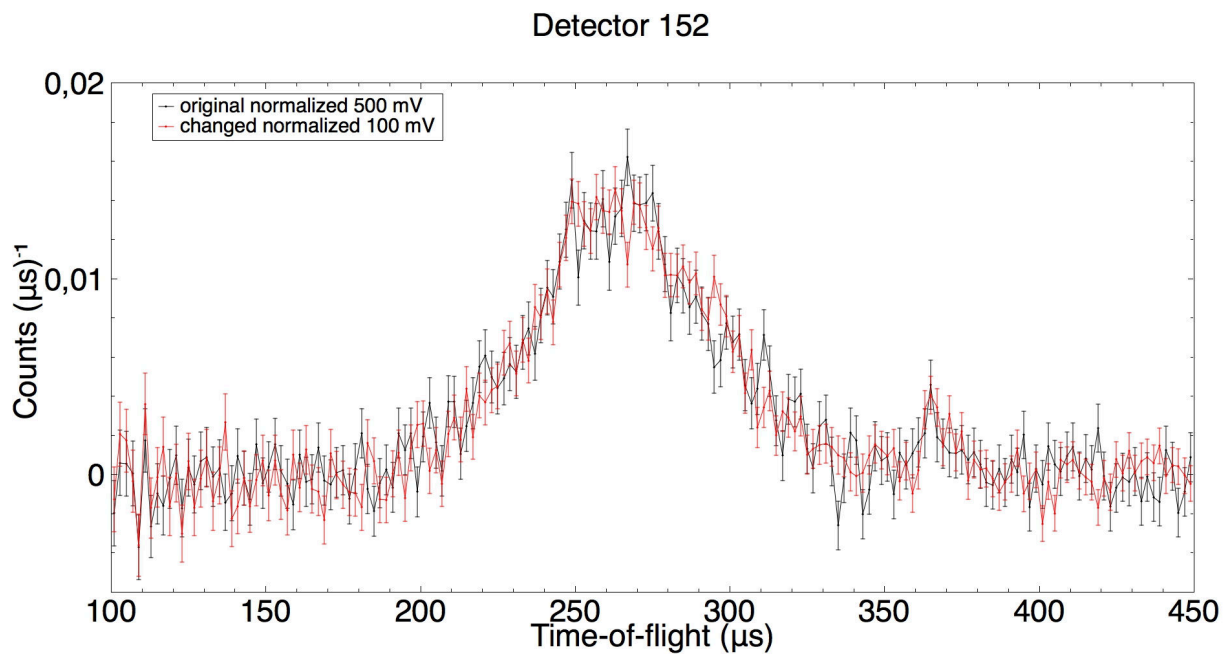


FIGURE B.5: Comparison of polyethylene spectra, with error bars, between original and changed threshold from detector 152 using a binning of  $2 \mu\text{s}$  normalized to the proton charge and to the peak area

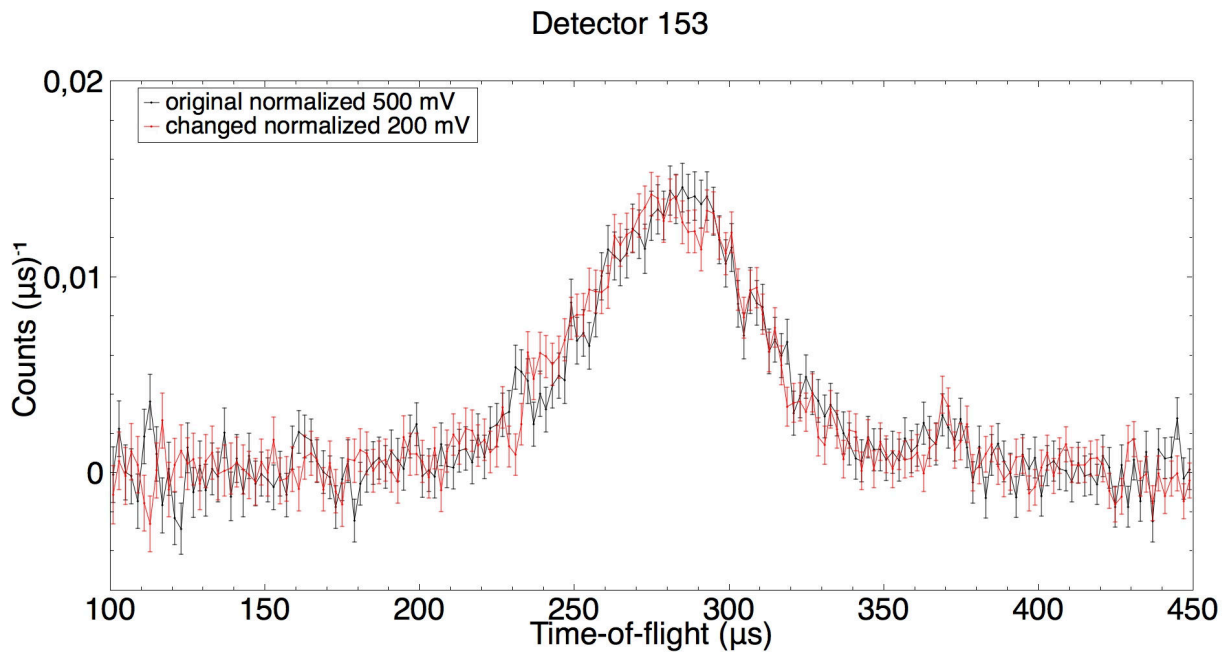


FIGURE B.6: Comparison of polyethylene spectra, with error bars, between original and changed threshold from detector 153 using a binning of  $2 \mu\text{s}$  normalized to the proton charge and to the peak area

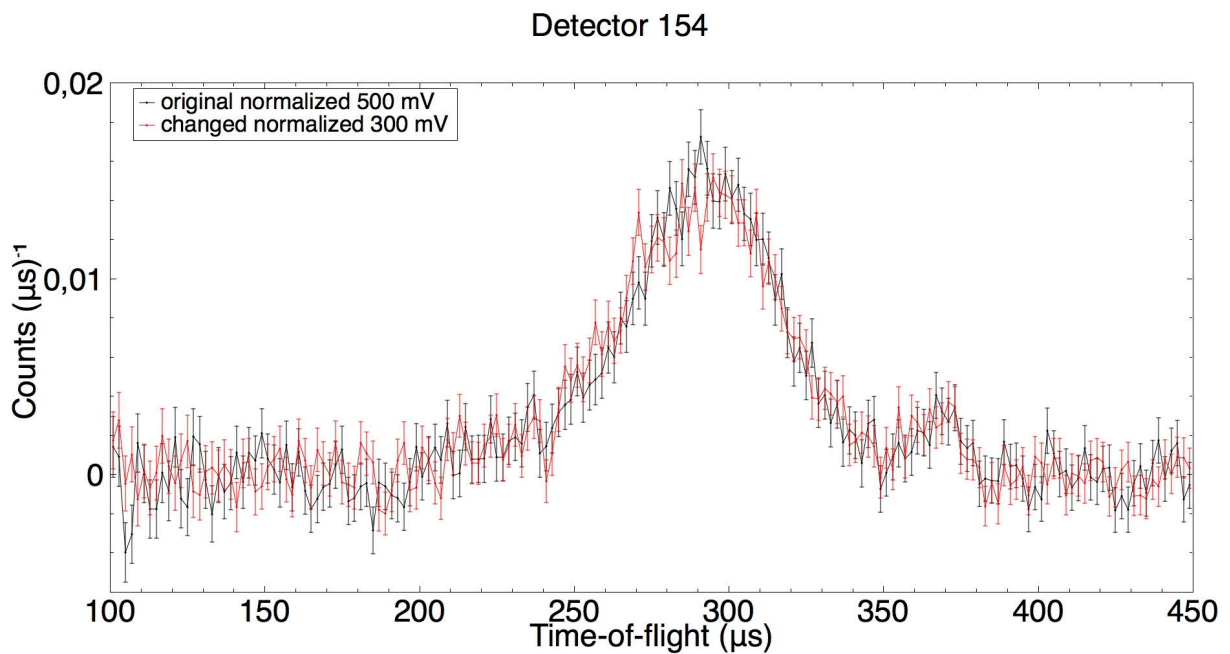


FIGURE B.7: Comparison of polyethylene spectra, with error bars, between original and changed threshold from detector 154 using a binning of  $2 \mu\text{s}$  normalized to the proton charge and to the peak area

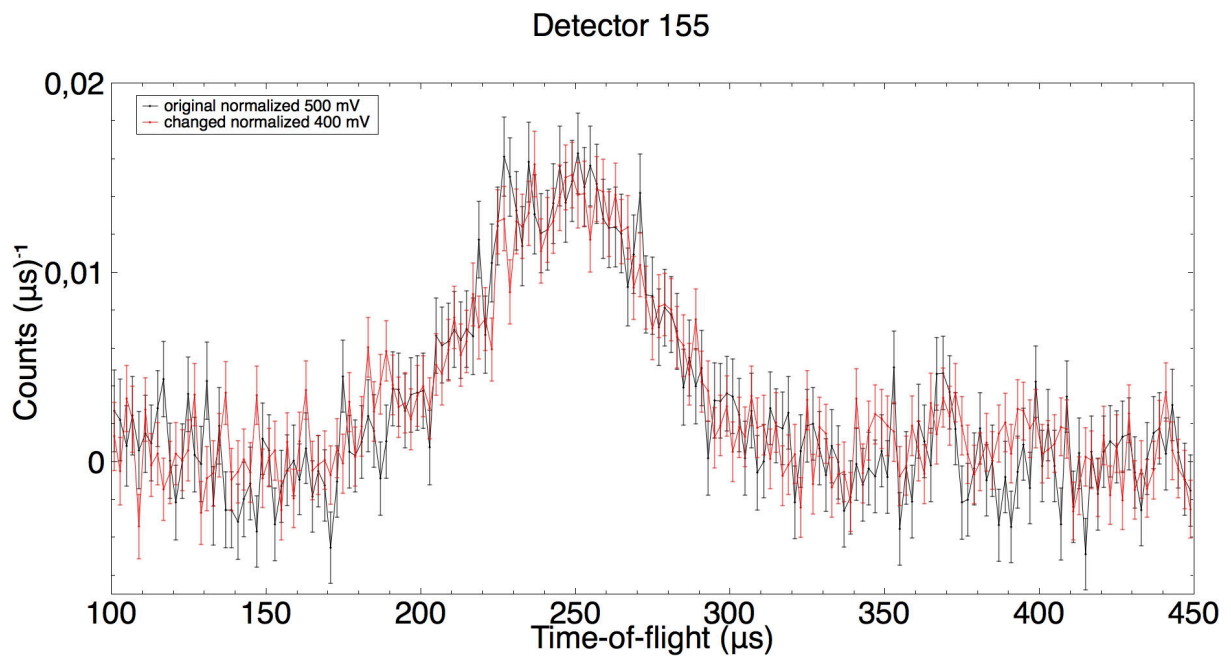


FIGURE B.8: Comparison of polyethylene spectra, with error bars, between original and changed threshold from detector 155 using a binning of  $2 \mu\text{s}$  normalized to the proton charge and to the peak area

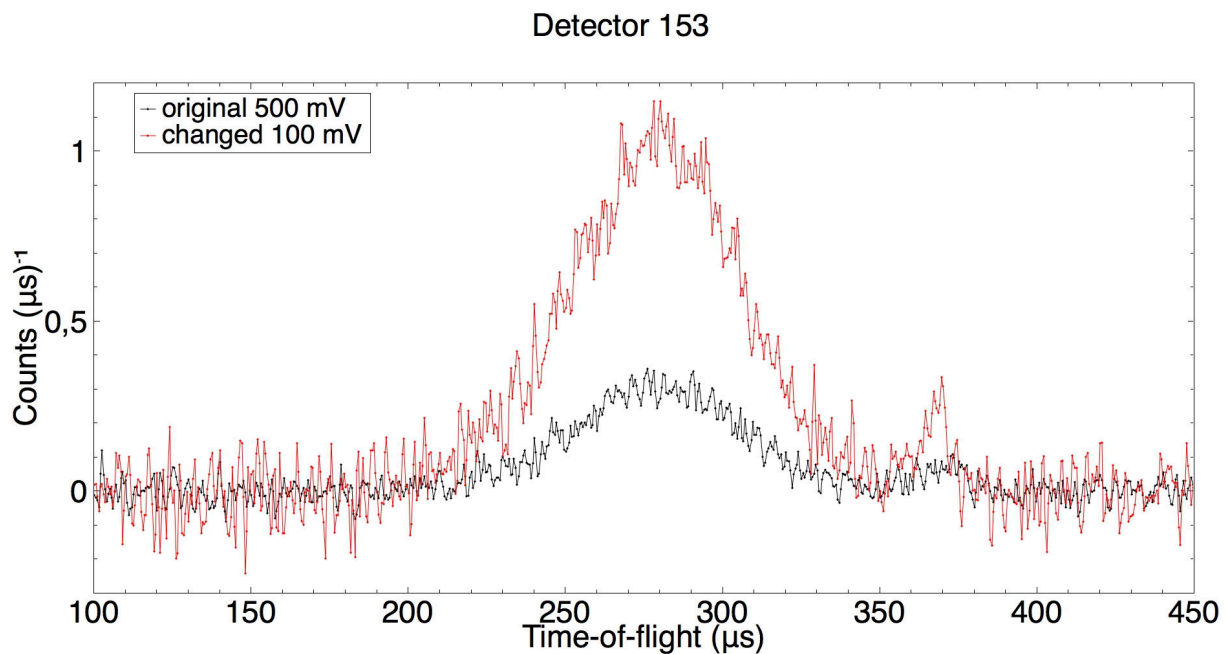


FIGURE B.9: Comparison of polyethylene spectra, without error bars, between original and changed threshold from detector 153 using a binning of  $0.5 \mu\text{s}$  normalized only to the proton charge

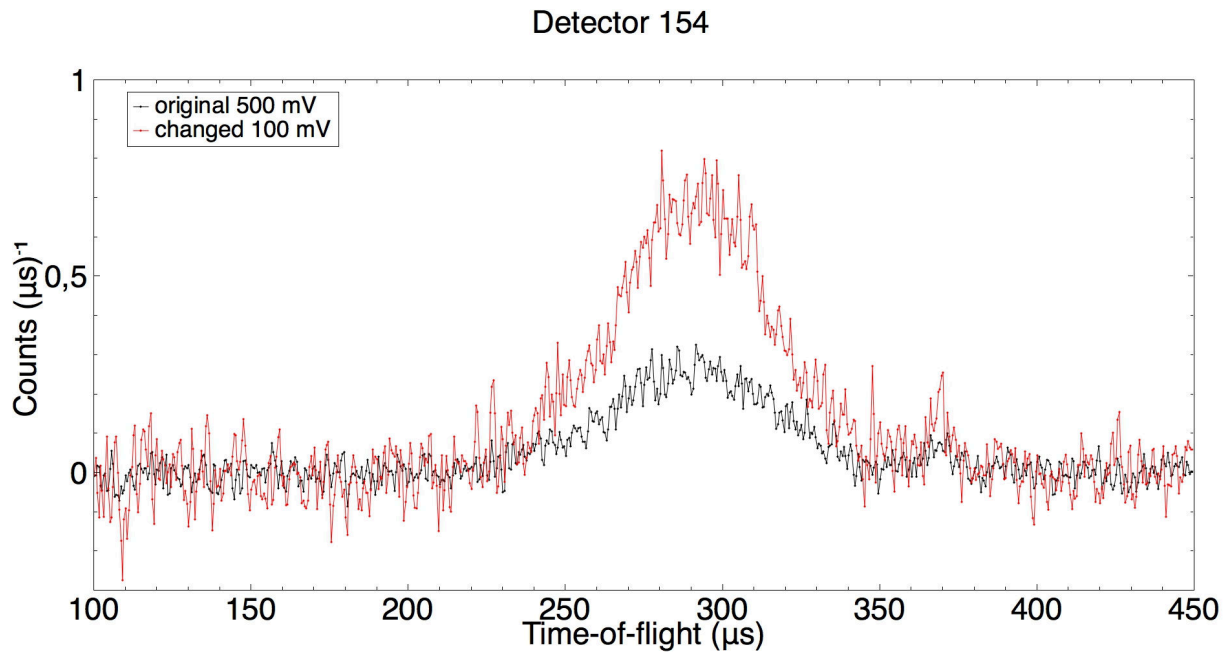


FIGURE B.10: Comparison of polyethylene spectra, without error bars, between original and changed threshold from detector 154 using a binning of  $0.5 \mu\text{s}$  normalized only to the proton charge

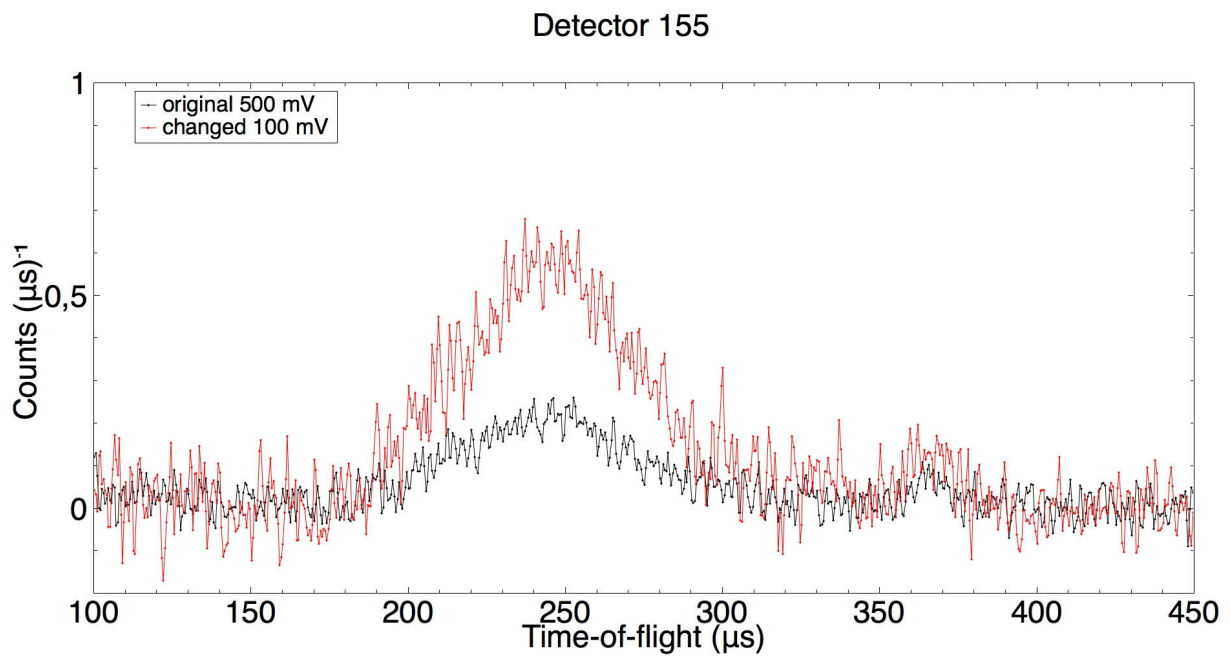


FIGURE B.11: Comparison of polyethylene spectra, without error bars, between original and changed threshold from detector 155 using a binning of  $0.5 \mu\text{s}$  normalized only to the proton charge

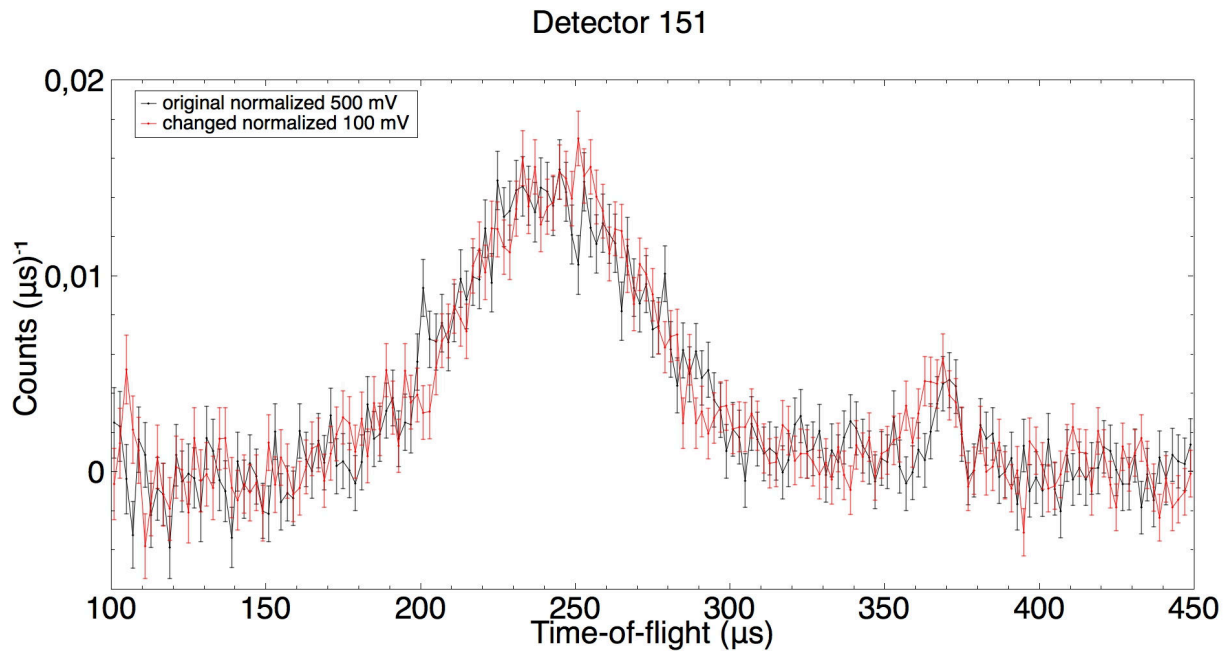


FIGURE B.12: Comparison of polyethylene spectra, with error bars, between original and changed threshold from detector 151 using a binning of  $2 \mu\text{s}$  normalized to the proton charge and to the peak area

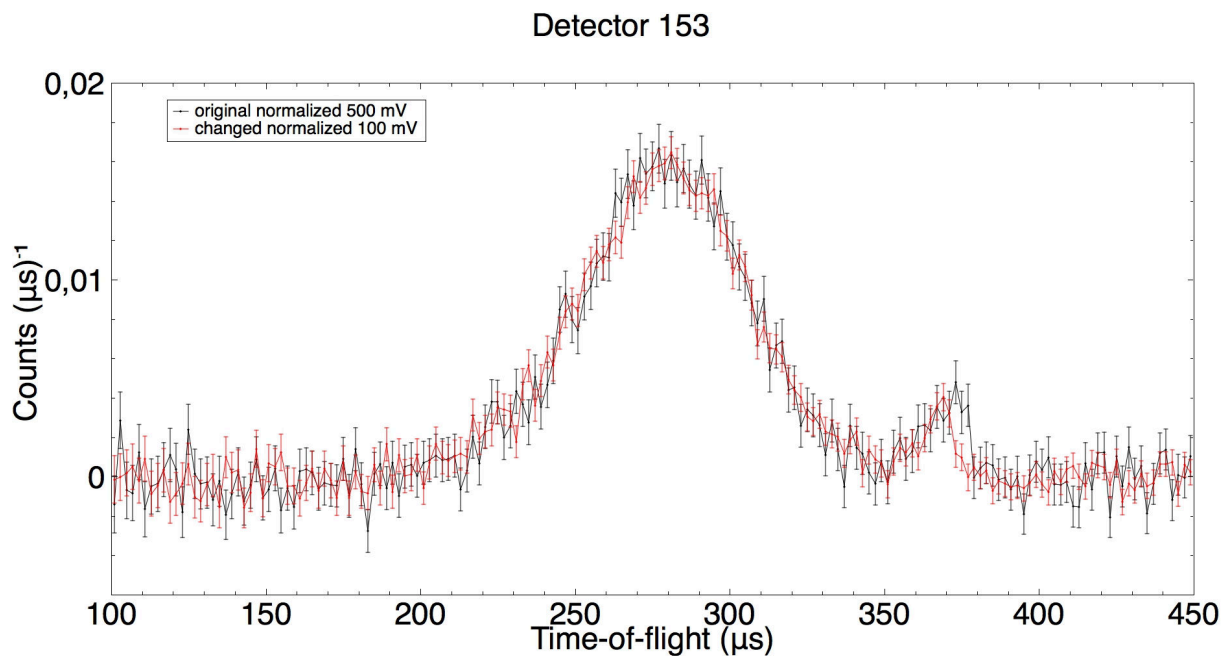


FIGURE B.13: Comparison of polyethylene spectra, with error bars, between original and changed threshold from detector 153 using a binning of  $2 \mu\text{s}$  normalized to the proton charge and to the peak area

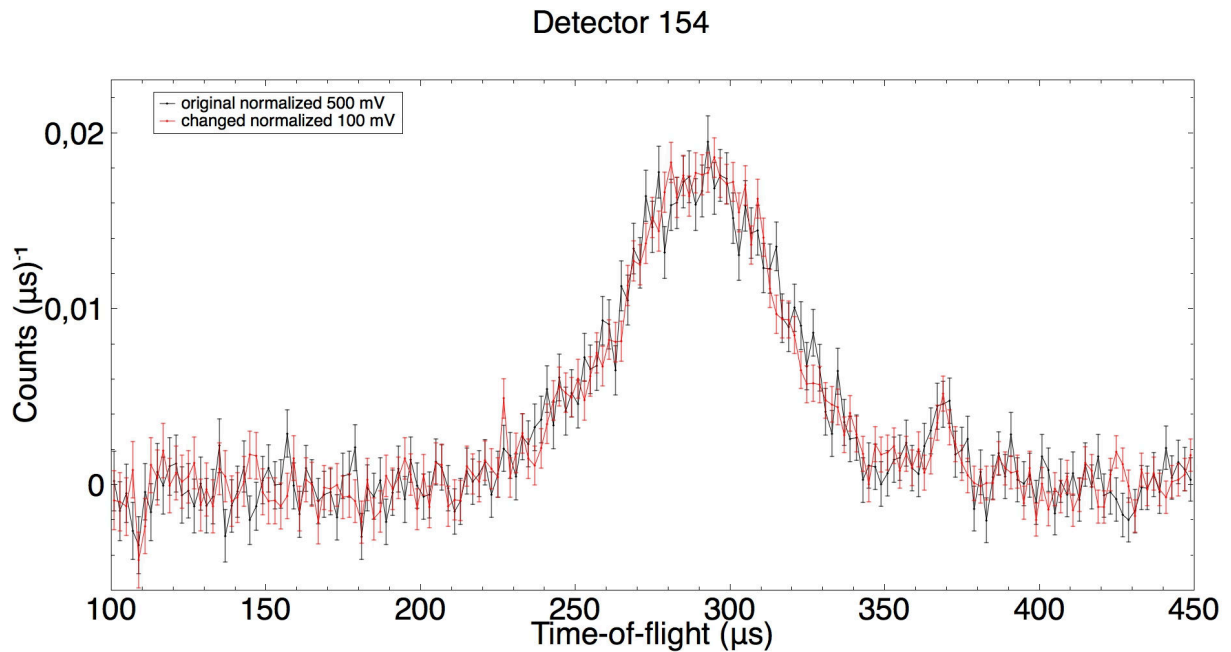


FIGURE B.14: Comparison of polyethylene spectra, with error bars, between original and changed threshold from detector 154 using a binning of  $2 \mu\text{s}$  normalized to the proton charge and to the peak area

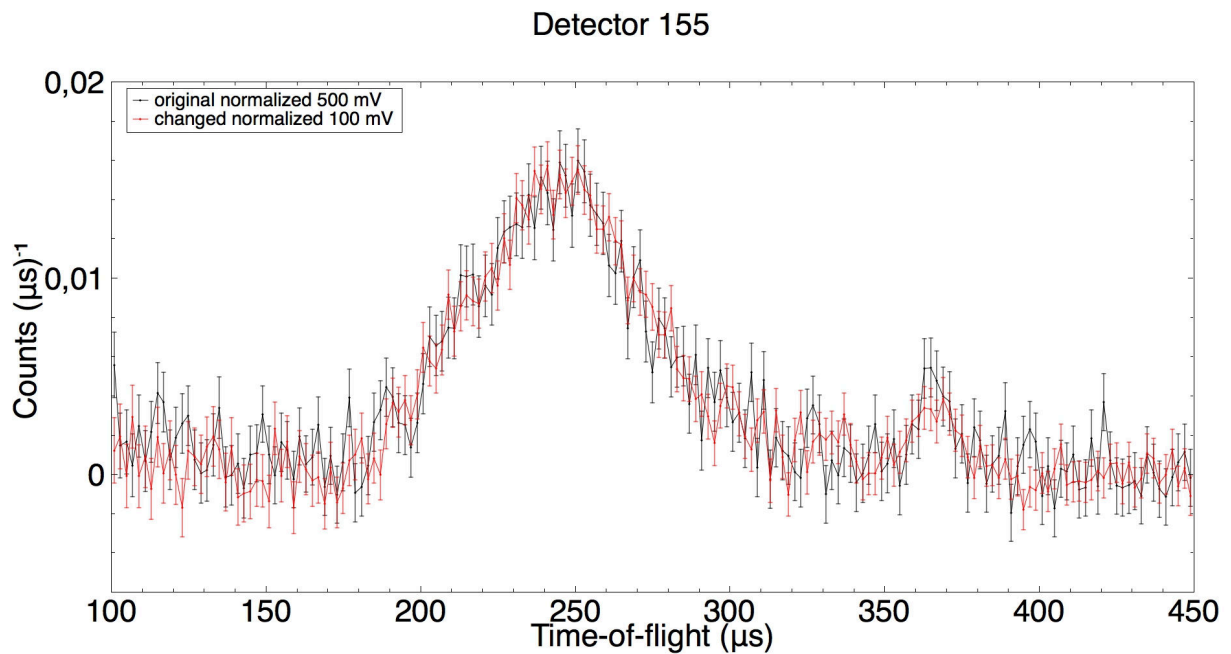


FIGURE B.15: Comparison of polyethylene spectra, with error bars, between original and changed threshold from detector 155 using a binning of  $2 \mu\text{s}$  normalized to the proton charge and to the peak area

## Appendix C

# Script used to fit $J(y, q)$ spectra

```

import mantid
from mantid.simpleapi import *

ipfile='/Users/pierfrancescoulpiani/Desktop/TESI MAGISTRALE/analisi/
Indium_post_moderator_calib_1Mar_3Bragg_L0_iter_2_IP.dat'

LoadVesuvio(Filename='27714-27738', SpectrumList='151-155', Mode=
'SingleDifference', InstrumentParFile=ipfile, OutputWorkspace='PE')

PE_reb=Rebin(InputWorkspace='PE', Params='110,1,510')
nspectra=PE_reb.getNumberHistograms()

for i in range(nspectra):
    profiles = "function=GramCharlier,width=[4, 5, 6],hermite_coeffs=[1, 0,
    0],k_free=0,sears_flag=1,function=Gaussian,width=12;"
    out_ws, fit_params, chi_sq = VesuvioTOFFit(InputWorkspace='PE_reb', Masses
    =[1.0079, 12.0], MassProfiles=profiles,IntensityConstraints='[1,-29.8]
    ', WorkspaceIndex=str(i))
    mass1, width1, intensity1 = fit_params.cell(0,1), fit_params.cell(1,1),
    fit_params.cell(3,1)*0.9

    mass_function = "name=GaussianComptonProfile,Mass="+str(mass1)+",Width="+
    str(width1)+",Intensity="+str(intensity1)
    background, corrected = VesuvioCalculateGammaBackground(InputWorkspace=
    'PE_reb', ComptonFunction=mass_function, WorkspaceIndexList=str(i))
    out_ws, fit_params, chi_sq = VesuvioTOFFit(InputWorkspace='corrected',
    Masses=[1.0079, 12.0], MassProfiles=profiles,IntensityConstraints='[1,
    -29.8]', WorkspaceIndex=0)
    RenameWorkspace(InputWorkspace='out_ws',OutputWorkspace='PE_fit_'+str(i))
    RenameWorkspace(InputWorkspace='fit_params',OutputWorkspace='PE_params_'+
    str(i))
    if (i==0):
        RenameWorkspace(InputWorkspace='corrected',OutputWorkspace=
        'PE_corrected')
        RenameWorkspace(InputWorkspace='background',OutputWorkspace=
        'PE_background')
    if (i>0):
        AppendSpectra(InputWorkspace1='PE_corrected',InputWorkspace2=
        'corrected',OutputWorkspace='PE_corrected')
        AppendSpectra(InputWorkspace1='PE_background',InputWorkspace2=
        'background',OutputWorkspace='PE_background')
    DeleteWorkspace('background')
    DeleteWorkspace('corrected')

ExtractSingleSpectrum(InputWorkspace='PE_fit_0',WorkspaceIndex=4,
OutputWorkspace='PE_carbon')
for i in range(nspectra-1):
    ExtractSingleSpectrum(InputWorkspace='PE_fit_'+str(i+1),WorkspaceIndex=4,
OutputWorkspace='tmp')
    AppendSpectra(InputWorkspace1='PE_carbon',InputWorkspace2='tmp',

```

```

        OutputWorkspace='PE_carbon')
Minus(LHSWorkspace='PE_corrected',RHSWorkspace='PE_carbon',OutputWorkspace=
'PE_corrected')

ConvertToYSpace(InputWorkspace='PE_corrected',Mass=1.0079,OutputWorkspace=
'PE_corrected',QWorkspace='PE_corrected_Q')
PE_corrected_1oQ=CloneWorkspace(InputWorkspace='PE_corrected_Q')
for j in range(PE_corrected_1oQ.getNumberHistograms()):
    for k in range(PE_corrected_1oQ.blocksize()):
        if (PE_corrected_1oQ.dataY(j)[k]!=0):
            PE_corrected_1oQ.dataY(j)[k]=1./PE_corrected_1oQ.dataY(j)[k]
Rebin(InputWorkspace='PE_corrected',Params='-30,1,30',OutputWorkspace=
'PE_corrected')
Rebin(InputWorkspace='PE_corrected_1oQ',Params='-30,1,30',OutputWorkspace=
'PE_corrected_1oQ')
tmp=Integration(InputWorkspace='PE_corrected',RangeLower='-30',RangeUpper='30
')
Divide(LHSWorkspace='PE_corrected',RHSWorkspace='tmp',OutputWorkspace=
'PE_corrected')

PE_corrected_readyforfit=CloneWorkspace(InputWorkspace='PE_corrected')
for j in range(PE_corrected_readyforfit.getNumberHistograms()):
    for k in range(PE_corrected_readyforfit.blocksize()):
        if (PE_corrected_readyforfit.dataE(j)[k]==0):
            PE_corrected_readyforfit.dataE(j)[k]=0.03

VesuvioResolution(Workspace='PE_background', Mass=1.0079,
    OutputWorkspaceYSpace='resolution')
Rebin(InputWorkspace='resolution',Params='-15,0.125,15',OutputWorkspace=
'resolution')
for i in range(nspectra-1):
    VesuvioResolution(Workspace='PE_background',WorkspaceIndex=str(i+1), Mass=
1.0079, OutputWorkspaceYSpace='tmp')
    Rebin(InputWorkspace='tmp',Params='-15,0.125,15',OutputWorkspace='tmp')
    AppendSpectra(InputWorkspace1='resolution',InputWorkspace2='tmp',
        OutputWorkspace='resolution')
tmp=Integration(InputWorkspace='resolution',RangeLower='-15',RangeUpper='15')
Divide(LHSWorkspace='resolution',RHSWorkspace='tmp',OutputWorkspace=
'resolution')
DeleteWorkspace('tmp')

sample_ws = mtd['PE_corrected_readyforfit']
resolution_ws = mtd['resolution']

convolution_template = """
(composite=Convolution,$domains={0});
name=Resolution,Workspace={1},WorkspaceIndex={0};
(
    name=UserFunction,Formula=A*exp( -(x-x0)^2/2/Sigma^2)/(2*3.1415*Sigma^2)
        ^0.5*(1+c4/32*(16*((x-x0)/sqrt(2.))/Sigma)^4-48*((x-x0)/sqrt(2.))/
        Sigma^2+12)),A=1.,x0=0.,Sigma=5.,c4=0
    ,ties=(c4=0);
(
    composite=ProductFunction,NumDeriv=false;name=TabulatedFunction,
        Workspace=PE_corrected_1oQ,WorkspaceIndex={0},ties=(Scaling=1,

```

```

        Shift=0,XScaling=1);
        name=UserFunction,Formula=Sigma*1.4142/12.*exp( -(x-x0)^2/2/Sigma^
        2)/(2*3.1415*Sigma^2)^0.5*( (8*((x-x0)/sqrt(2.)/Sigma)^3-12*((x
        -x0)/sqrt(2.)/Sigma))),x0=0,Sigma=5
    );ties=(f0.x0=f1.f1.x0
))""""

nspectra = sample_ws.getNumberHistograms()
convolved_funcs = []
ties = []
datasets = {}
counter = 0
for i in range(nspectra):
    spec_i = sample_ws.getSpectrum(i)
    det_i = sample_ws.getDetector(i)
    if det_i.isMasked():
        print "Skipping masked spectrum {}".format(spec_i.getSpectrumNo())
        continue
    f1 = convolution_template.format(counter, resolution_ws.getName())
    convolved_funcs.append(f1)
    if i > 0:
        ties.append('f{0}.f1.f0.Sigma= f{0}.f1.f1.f1.Sigma=f0.f1.f0.Sigma'.
            format(counter))
        attr = 'InputWorkspace_{0}'.format(counter) if i > 0 else
            'InputWorkspace'
    datasets[attr] = sample_ws.getName()
    attr = 'WorkspaceIndex_{0}'.format(counter) if i > 0 else 'WorkspaceIndex'
    datasets[attr] = i
    counter += 1

multifit_func = 'composite=MultiDomainFunction;' + ';'.join(convolved_funcs)
    + ';ties=({0},f0.f1.f1.f1.Sigma=f0.f1.f0.Sigma)'.format(','.join(ties))

Fit(multifit_func, Output='fit', **datasets)

```

# Bibliography

- [1] Carla Andreani et al. 'Electron-volt neutron spectroscopy: beyond fundamental systems'. In: *Advances in Physics* 66.1 (2017), pp. 1–73.
- [2] Carla Andreani et al. 'Atomic Quantum Dynamics in Materials Research'. In: *Experimental Methods in the Physical Sciences*. Vol. 49. Dec. 2017, pp. 403–457. ISBN: 9780128053249.
- [3] Lev Davidovich Landau and Evgenii Mikhailovich Lifshitz. 'Quantum mechanics: non-relativistic theory'. In: (1958).
- [4] C Andreani et al. 'Measurement of momentum distribution of lightatoms and molecules in condensed matter systems using inelastic neutron scattering'. In: *Advances in Physics* 54.5 (2005), pp. 377–469.
- [5] Lin Lin et al. 'Momentum distribution, vibrational dynamics, and the potential of mean force in ice'. In: *Physical Review B* 83.22 (2011), p. 220302.
- [6] R Senesi et al. 'From neutron Compton profiles to momentum distribution: Assessment of direct numerical determination'. In: *Nuclear Instruments and Methods in Physics Research Section A: Accelerators, Spectrometers, Detectors and Associated Equipment* 704 (2013), pp. 36–39.
- [7] D Flammini et al. 'Spherical momentum distribution of the protons in hexagonal ice from modeling of inelastic neutron scattering data'. In: *The Journal of chemical physics* 136.2 (2012), p. 024504.
- [8] Giovanni Romanelli et al. 'Direct measurement of competing quantum effects on the kinetic energy of heavy water upon melting'. In: *The Journal of Physical Chemistry Letters* 4.19 (2013), pp. 3251–3256.
- [9] D Kaplan et al. 'Hydrogenation of evaporated amorphous silicon films by plasma treatment'. In: *Applied Physics Letters* 33.5 (1978), pp. 440–442.
- [10] V Philipps et al. 'Erosion and redeposition of wall material in controlled fusion devices'. In: *Vacuum* 67.3 (2002), pp. 399–408.
- [11] Ian P Silverwood, Stewart F Parker, and C Richard A Catlow. 'Neutron scattering in catalysis and energy materials'. In: *Physical Chemistry Chemical Physics* 18.26 (2016), pp. 17140–17140.
- [12] A Pietropaolo et al. ' $\gamma$ -Ray background sources in the VESUVIO spectrometer at ISIS spallation neutron source'. In: *Nuclear Instruments and Methods in Physics Research Section A: Accelerators, Spectrometers, Detectors and Associated Equipment* 608.1 (2009), pp. 121–124.

- [13] G Festa et al. 'Characterization of  $\gamma$ -ray background at IMAT beamline of ISIS Spallation Neutron Source'. In: *Journal of Instrumentation* (2017).
- [14] Henry R Glyde. *Excitations in liquid and solid helium*. Clarendon Press Oxford, 1994.
- [15] *JANIS database*. URL: <http://www.oecd-nea.org/janisweb/>.
- [16] Masatoshi Arai and K Crawford. 'Neutron sources and facilities'. In: *Neutron imaging and applications*. Springer, 2009, pp. 13–30.
- [17] *ISIS facility website*. URL: [www.isis.stfc.ac.uk](http://www.isis.stfc.ac.uk).
- [18] G Romanelli et al. 'Characterisation of the incident beam and current diffraction capabilities on the VESUVIO spectrometer'. In: *Measurement Science and Technology* 28.9 (2017).
- [19] EM Schooneveld et al. 'Radiative neutron capture as a counting technique at pulsed spallation neutron sources: a review of current progress'. In: *Reports on Progress in Physics* 79.9 (2016), p. 094301.
- [20] Knoll Glen F. *Radiation Detection and Measurement*. 2010.
- [21] Antonino Pietropaolo. 'Research and development of  $\gamma$  detectors for neutron scattering at electron Volt energies on VESUVIO spectrometer'. PhD thesis. University of Rome Tor Vergata, 2004.
- [22] C Andreani et al. 'Double difference method in deep inelastic neutron scattering on the VESUVIO spectrometer'. In: *Nuclear Instruments and Methods in Physics Research Section A: Accelerators, Spectrometers, Detectors and Associated Equipment* 497.2 (2003), pp. 535–549.
- [23] M Tardocchi et al. 'YAP scintillators for resonant detection of epithermal neutrons at pulsed neutron sources'. In: *Review of scientific instruments* 75.11 (2004), pp. 4880–4890.
- [24] Dalila Onorati. MA thesis. University of Rome Tor Vergata. URL: <http://purl.org/net/epubs/work/33481015>.
- [25] G. Molnar. *Handbook of Prompt Gamma Activation Analysis*.
- [26] Fabio Sauli. 'The gas electron multiplier (GEM): Operating principles and applications'. In: *Nuclear Instruments and Methods in Physics Research Section A: Accelerators, Spectrometers, Detectors and Associated Equipment* 805 (2016), pp. 2–24.
- [27] K Kaneko and T Kohmura. 'Soft X-ray response of Au-GEM'. In: *Journal of Instrumentation* 7.07 (2012), p. C07001.
- [28] H Postma et al. 'Neutron-resonance capture analysis of materials'. In: *Journal of radioanalytical and nuclear chemistry* 248.1 (2001), pp. 115–120.
- [29] RL Paul and RM Lindstrom. 'Prompt gamma-ray activation analysis: fundamentals and applications'. In: *Journal of Radioanalytical and Nuclear Chemistry* 243.1 (2000), pp. 181–189.
- [30] G Festa et al. 'Isotope identification capabilities using time resolved prompt gamma emission from epithermal neutrons'. In: *Journal of Instrumentation* 11.03 (2016), p. C03060.
- [31] Michael P Failey et al. 'Neutron-capture prompt. gamma.-ray activation analysis for multielement determination in complex samples'. In: *Analytical Chemistry* 51.13 (1979), pp. 2209–2221.

- [32] Koo Ley et al. 'Neutron activation analysis'. In: *Journal of the Korean Nuclear Society* 5.4 (1973).
- [33] M Blaauw, H Postma, and P Mutti. 'Quantitative neutron capture resonance analysis verified with instrumental neutron activation analysis'. In: *Nuclear Instruments and Methods in Physics Research Section A: Accelerators, Spectrometers, Detectors and Associated Equipment* 505.1 (2003), pp. 508–511.
- [34] Antonino Pietropaolo et al. 'A neutron resonance capture analysis experimental station at the ISIS spallation source'. In: *Applied spectroscopy* 64.9 (2010), pp. 1068–1071.
- [35] Peter Schillebeeckx et al. 'Neutron resonance spectroscopy for the characterization of materials and objects'. In: *Journal of Instrumentation* 7.03 (2012), p. C03009.
- [36] Roberto Senesi, Alexander I Kolesnikov, and Carla Andreani. 'Measurement of proton momentum distributions using a direct geometry instrument'. In: *Journal of Physics: Conference Series*. Vol. 571. 1. IOP Publishing. 2014, p. 012007.
- [37] C Andreani, C Pantalei, and R Senesi. 'Mean kinetic energy of helium atoms in fluid  $3\text{He}$  and  $3\text{He}$ – $4\text{He}$  mixtures'. In: *Journal of Physics: Condensed Matter* 18.24 (2006), p. 5587.
- [38] A Miceli et al. 'Measurements of gamma-ray background spectra at spallation neutron source beamlines'. In: *Journal of Analytical Atomic Spectrometry* 29.10 (2014), pp. 1897–1903.
- [39] J Mayers et al. 'VESUVIO—the double difference inverse geometry spectrometer at ISIS'. In: *Physica B: Condensed Matter* 350.1 (2004), E659–E662.
- [40] A Pietropaolo et al. ' $\gamma$  detectors for deep inelastic neutron scattering in the 1–100 eV energy region'. In: *Applied Physics A* 74.1 (2002), s189–s190.
- [41] G Gorini et al. 'The resonant detector and its application to epithermal neutron spectroscopy'. In: *Nuclear Instruments and Methods in Physics Research Section A: Accelerators, Spectrometers, Detectors and Associated Equipment* 529.1 (2004), pp. 293–300.
- [42] A Pietropaolo et al. 'Resolution function in deep inelastic neutron scattering using the Foil Cycling Technique'. In: *Nuclear Instruments and Methods in Physics Research Section A: Accelerators, Spectrometers, Detectors and Associated Equipment* 570.3 (2007), pp. 498–510.
- [43] S Imberti et al. 'Resolution of the VESUVIO spectrometer for High-energy Inelastic Neutron Scattering experiments'. In: *Nuclear Instruments and Methods in Physics Research Section A: Accelerators, Spectrometers, Detectors and Associated Equipment* 552.3 (2005), pp. 463–476.
- [44] Antonino Pietropaolo and Roberto Senesi. 'Electron Volt neutron spectrometers'. In: *Physics Reports* 508.3 (2011), pp. 45–90.
- [45] Antonino Pietropaolo et al. 'DINS measurements on VESUVIO in the Resonance Detector configuration: proton mean kinetic energy in water'. In: *Journal of Instrumentation* 1.04 (2006), P04001.
- [46] C Andreani et al. 'A resonant detector for high-energy inelastic neutron scattering experiments'. In: *Applied physics letters* 85.22 (2004), pp. 5454–5456.
- [47] R Senesi et al. 'Deep-Inelastic Neutron Scattering Determination of the Single-Particle Kinetic Energy in Solid and Liquid  $\text{H}_3\text{e}$ '. In: *Physical review letters* 86.20 (2001), p. 4584.

- [48] J Mayers, AL Fielding, and R Senesi. 'Multiple scattering in deep inelastic neutron scattering: Monte Carlo simulations and experiments at the ISIS eVS inverse geometry spectrometer'. In: *Nuclear Instruments and Methods in Physics Research Section A: Accelerators, Spectrometers, Detectors and Associated Equipment* 481.1 (2002), pp. 454–463.
- [49] R Senesi et al. 'VESUVIO: a novel instrument for performing spectroscopic studies in condensed matter with eV neutrons at the ISIS facility'. In: *Physica B: Condensed Matter* 276 (2000), pp. 200–201.
- [50] Laura Arcidiacono. 'Gamma Spectroscopy and Time resolved Prompt Gamma Activation Analysis at ISIS Spallation Neutron Source'. MA thesis. University of Rome Tor Vergata, 2015/2016.
- [51] M Tardocchi et al. 'Cadmium–Zinc–Telluride photon detector for epithermal neutron spectroscopy—pulse height response characterisation'. In: *Nuclear Instruments and Methods in Physics Research Section A: Accelerators, Spectrometers, Detectors and Associated Equipment* 526.3 (2004), pp. 477–492.
- [52] Veljko Radeka. 'Low-noise techniques in detectors'. In: *Annual Review of Nuclear and Particle Science* 38.1 (1988), pp. 217–277.
- [53] Price David L. and Fernandez-Alonso F. *An introduction to Neutron Scattering*. 2013.
- [54] EM Schooneveld et al. 'Foil cycling technique for the VESUVIO spectrometer operating in the resonance detector configuration'. In: *Review of scientific instruments* 77.9 (2006), p. 095103.
- [55] C Andreani et al. 'Electron-volt spectroscopy at a pulsed neutron source using a resonance detector technique'. In: *Nuclear Instruments and Methods in Physics Research Section A: Accelerators, Spectrometers, Detectors and Associated Equipment* 481.1 (2002), pp. 509–520.
- [56] A Pietropaolo et al. 'Characterization of the  $\gamma$  background in epithermal neutron scattering measurements at pulsed neutron sources'. In: *Nuclear Instruments and Methods in Physics Research Section A: Accelerators, Spectrometers, Detectors and Associated Equipment* 568.2 (2006), pp. 826–838.
- [57] Windsor C. G. *Pulsed neutron scattering*. 1981.
- [58] Foderaro Anthony. *The elements of neutron interaction theory*. 1971.
- [59] Squires G. L. *Thermal neutron scattering*. 1978.
- [60] Lovesey Stephen W. *Theory of neutron scattering from condensed matter*. 1984.
- [61] Takahisa Koike et al. 'A new gamma-ray detector with gold-plated gas electron multiplier'. In: *Nuclear Instruments and Methods in Physics Research Section A: Accelerators, Spectrometers, Detectors and Associated Equipment* 648.1 (2011), pp. 180–185.
- [62] AG Seel, M Krzystyniak, and F Fernandez-Alonso. 'The VESUVIO Spectrometer Now and When?' In: *Journal of Physics: Conference Series*. Vol. 571. 1. IOP Publishing. 2014, p. 012006.